UNIVERSITY OF BERGEN
DEPARTMENT OF MATHEMATICS

Boussinesq modeling of the influence of wave energy converters on nearshore circulation

Author: Andreas Bondehagen Jacobsen
Supervisors: Henrik Kalisch & Volker Roeber

UNIVERSITETET I BERGEN
Det matematisk-naturvitenskapelige fakultet

May, 2023

Abstract

[Currents in the surf zone have an impact upon the creation and patterns of vortexes, which causes transportation of mass and momentum over a broad range of temporal time-scales. These currents are responsible for a number of phenomena such as sediment transport, spread of bacteria and marine micro-organisms, and transportation of pollutions. Additionally there have recently been found that the effects of transport of inertial particles, sand flux, and the location of the river is dominated by currents oscillating at infra-gravity periods.

In this thesis, previously documented theory necessary to it is presented. Firstly, the first and second order wave elevation and velocity is redeveloped, together with the second order Stokes drift. Further, theory regarding surface wave processes and Lagrangian particles are re-counted. Before lastly, methods of recreating 2D wave spectra from 1D buoy data and particle paths from stereo camera and GPS coordinates are described.

Throughout the thesis a phase-resolving nearshore wave model (BOSZ) is routinely used to test theoretical results and recreate experimental data. An overview of the numerical methods used by BOSZ to solve an alteration to Nwogu's equations is given. Further the theory of Turbulent Kinetic Energy (TKE) is summarized. To verify whether BOSZ is capable of modelling the near shore wave processes, multiple tests are conducted. Here the data of three laboratory tests are compared to outputs of BOSZ.

It is investigated how small amplitude infra-gravity (IG) waves are critical for the transportation of fluid particles in the surf zone. These low amplitude and frequency waves are responsible for large particle movements in the nearshore and surf zone regions. This is shown by looking at linear theory, creating a linear numerical model, and through simulations with BOSZ [1]. Further, data from a recent field study where orange tracers were tracked with a stereo-camera system is processed to extract their movements. The initial data is extracted and entered into BOSZ which simulate inertial particles. The numerical paths from the model is then compared with the paths of the oranges [2].

The verified ability to replicate nearshore velocity fields is used to bring to light the properties of surf zone circulation patterns. The influence of tidal elevation, mean direction and directional spread of the incoming wavefield on the quantity, extend, and circulatory magnitude of the surf zone circulation is studied. The nature of wave-induced circulation patterns such as horizontal eddies is investigated, and comparisons are made to Rankine vortexes [2].

Lastly, the theoretical results of the efficiency of an oscillating wave surge converter (OWSC) is briefly explained. A numerical scheme to calculate this efficiency is then developed and a method to use it in BOSZ is implemented. From this we compare how including an idealised OWSC farm in our computations changes the surf zone circulations [1].]

[1]This study is currently in the work of being made into a paper.

[2]The results of this study have been submitted for publication [Bondehagen et al., 2023].

Acknowledgements

I want to thank my supervisors Henrik Kalisch and Volker Roeber for the multiple talks we have had about the thesis. To Henrik I would say thank you for pointing me in the the direction of resarch and connecting me to the right people, and to Volker thank you for spending multiple hours teaching me your model and pre-processing data for our research.

Further I would like to thank Marc Buckley, Michael Streßer and Maria Bjørnestad for the meetings about the experiment at Sylt and how to use the data from there. A special thanks to Marc for the scripts provided.

Also thanks to Lutz Christiansen and the LKN.SH (Landesbetrieb für Küstenschutz, Nationalpark und Meeresschutz Schleswig-Holstein) for providing bathymetric data for the bathymetry around Sylt.

Without all these people, this thesis would not exist.

Andreas Bondehagen Jacobsen
26 May, 2023

Contents

Introduction

The nearshore zone is a dynamic environment where waves interact with the sea bed and coastal structures, creating complex and diverse hydrodynamic features [Holthuijsen, 2010]. Understanding the physical processes that govern nearshore circulation is important for a variety of applications, such as coastal engineering, environmental management, and wave energy extraction. The nearshore circulation is primarily driven by the wave-induced longshore currents and rip currents, which transport sediment and nutrients along the coast and affect the local ecology and coastal morphology [Bertin et al., 2018, Bertin et al., 2019, Russell, 1993, van Thiel de Vries et al., 2008].

How infra-gravity (IG) waves influence these processes have in recent years been of increasing interest. IG waves are waves of periods 30s up to 5 minutes, compared to the the ordinary gravity waves of periods 1s to $30s$ [Munk, 1951]. These waves also have very small amplitudes, often on the order of millimeters to a couple of centimeters making them hard to notice [Longuet-Higgins and Stewart, 1962, Longuet-Higgins and Stewart, 1964, Symonds et al., 1982]. It is now known that IG waves influence the hydrodynamics and effect the rip currents and storm surges, but they are also important for coastal processes such as beach and dune erosion [Bertin et al., 2018, Bertin et al., 2019, Russell, 1993, van Thiel de Vries et al., 2008]. Further, multiple effects in the surf zone have been found to oscillate with periods found in the IG-domain. For example the location of the river plume [Flores et al., 2022], net movement of inertial particles [Bjørnestad et al., 2021], and sand flux [Mendes et al., 2020]. This thesis takes upon itself to continue investigating how IG waves influences particle transport in the surf zone.

In recent years, numerical models have become an essential tool for studying nearshore circulation patterns. Among them, the phase-resolving wave models have been shown to accurately reproduce the complex wave transformation and nearshore hydrodynamics. In this thesis, we use the phase-resolving nearshore wave model Boussinesq Ocean and surf zone model (BOSZ) introduced in [Roeber et al., 2010], and under continuous development during the last ten years, to investigate the properties of surf zone circulation patterns. We focus on the influence of tidal elevation, mean direction, and directional spread of the incoming wavefield on the quantity, extent, and circulatory magnitude of the nearshore circulation.

To validate our numerical simulations, we compare the model results to data from a recent measurement campaign conducted at a beach on the island of Sylt, located off the German North Sea Coast near the border with Denmark [Bjørnestad et al., 2021]. Wave poles with graduation were mounted at low tide, together with pressure sensors and an Acoustic Doppler Velocimeter (ADV). In addition, oranges were used as surface tracers in connection with a two-camera stereo

imaging system which was able to track the surface tracers. By replicating the tracer movement using the model, we can assess the accuracy of the model in capturing the essential features of the nearshore velocity fields. While somewhat limited by the size of the field of view (FOV), the stereo images allow us to calibrate the numerical modeling of the orange tracers, and as shown in Ch. (6), the comparison is favorable.

In the thesis, we study the influence of three parameters on the nature of surf zone circulation patterns. In fact, we consider the joint influence of the peak direction D_P of the incoming wave field, the directional spread σ_θ of the applied spectrum and the tidal level. While many field studies are limited to one or two of these parameters [Baker et al., 2021][O'Dea et al., 2021][Choi et al., 2015][Scott et al., 2014], and may not paint a complete picture, in the present work, we can investigate the combined influence of these three parameter.

The numerical simulations are then used to study the influence of the three basic parameters peak direction D_P of the incoming wave field, the directional spread σ_θ of the applied spectrum and the tidal 1evel on the nature of the surf zone circulation. In particular, we quantify the quantity, strength, and size of vortexes, and their statistical dependence on the parameters. Further, we study the nature of each single vortex, and compares the circulation to a combination of solid-body rotation and irrotational vortexes known as a rankine vortex.

Also of current interest is the conversion of wave energy to electrical energy. Wave energy converters are newly developing technology which generally have high captor factors (C_f) of the targeting energy. Among these the Oscillating wave surge converters (OWSC) have the largest C_f value [Babarit, 2015]. Additionally, ocean waves have energy densities of $2 - 3$kW/m^2 compared to $0.1 - 0.3$ for solar and produce energy 90% of the time compared to $20 - 30\%$ for wind and solar [Drew et al., 2009].

Earlier it has been common to use a power matrix on a frequency-direction spectrum to calculate the average capture factor of the device over longer periods of time [Babarit, 2015]. This approach is unfeasible in a phase-resolving model, as the underlying distribution of the waves are unknown. [Renzi and Dias, 2013] derived an expression for the capture factor of an OWSC inspired by the Oyster 2 placed in the open sea. The only necessary input for their calculations were the parameters of the device itself, and the amplitude and period of the incoming wave field. This information is possible to estimate from a wave-to-wave basis as the phase-resolving model return the ocean elevation at every time step. Hence in this thesis we will continue the work of modelling these OWSC in a phase resolving model, and compare their impact on the surf zone circulation with the earlier results gathered from Sylt.

Structure of thesis

The thesis is divided into 8 chapters. The first three is previous knowledge reproduced for this thesis. Chapter 4 through 7 is four different parts written by me, each with their own discussion. Before lastly chapter 8 is a summary of the paper. Below is a short description of their content:

Chapter 1: All necessary theory to understand the paper. This includes wave theory, Nwogus equations, particle transport, how to transform coordinates from cameras to world coordinates, and how to recreaste 2D wave spectra from 1D spectra.

Chapter 2: Main ideas behind the numerics of BOSZ.

Chapter 3: Contains three tests to verify that BOSZ can recreate the surf zone processes described in Chapter 1.

Chapter 4: The influence of infra-gravity waves on particle transport is looked into. This is shown by linear wave theory, a linear model, and BOSZ.

Chapter 5: Verification of BOSZ by tracking oranges outside the island of Sylt with cameras. LiDAR data, buoys, and camera data are used in conjunction with numerical drifters to recreate particle paths.

Chapter 6: The bathymetry of Sylt is used to see how the creating of vortexes in the surf zone is influenced by the tide, directional spreading and main direction of the incoming waves.

Chapter 7: A numerical scheme to calculate the power of Oscillating wave surge converters is developed, and a rudimentary approach to include them in BOSZ is found. Then by repeating the simulation in Chapter (6) with a farm of these converters we show how these influence the surf zone circulations.

Chapter 8: The plain language summary of the new results of the thesis.

1 Theory

1.1 First order linear theory

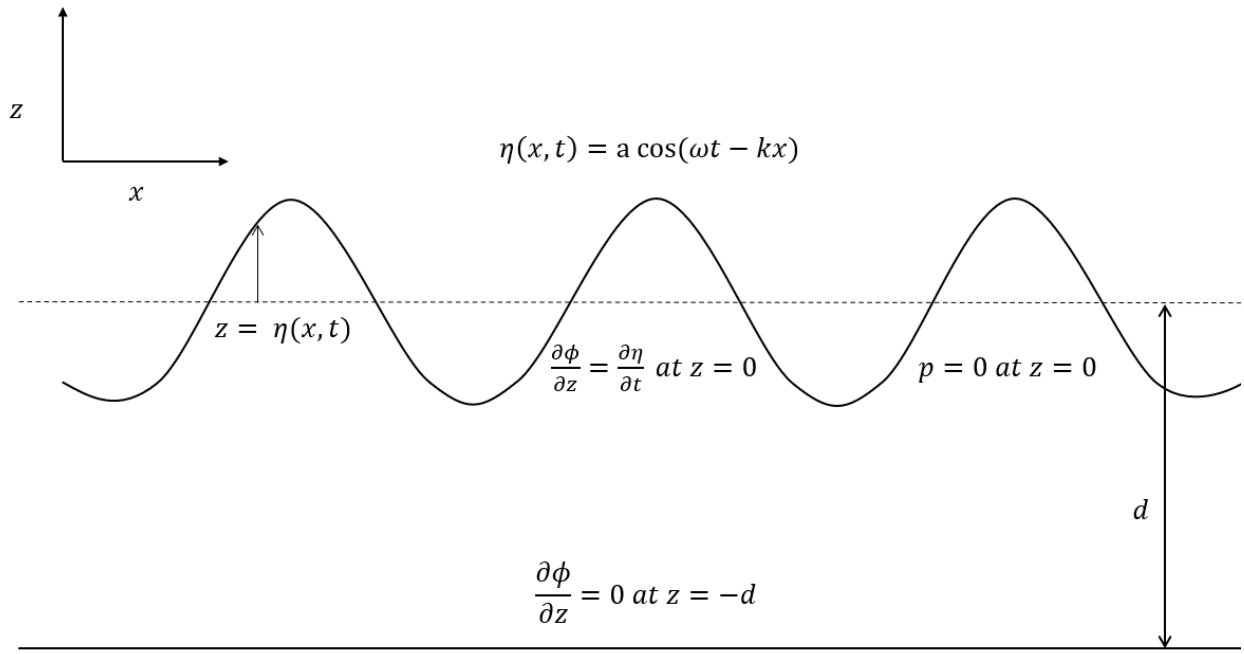

Figure 1: First order linear wave theory problem

In this section we follow [Kundu et al., 2015]

1.1.1 Fluid equations and boundary conditions

For all Newtonian fluids the Navier-Stokes equations describe the motion, which are written in Cartesian coordinates as:

$$\frac{\partial\rho}{\partial t} + \nabla\cdot(\rho\mathbf{u}) = 0 \tag{1}$$

$$\rho\frac{D\mathbf{u}}{Dt} = -\nabla p - \rho g\mathbf{e}_z + \mu\nabla^2\mathbf{u} \tag{2}$$

Assume we have an incompressible, irrotational, and inviscid fluid with constant density. Additionally, assume that the earths gravitation is the only body force. We also exclude wind generation and surface tension. Further we make the limitations that the water should not leave the surface of the waves, that it cannot penetrate the bottom, and that the pressure is continuous over the interface.

Applying these restrictions to the full Navier-Stokes equations we get the following problem:

$$\nabla \cdot \mathbf{u} = 0 \tag{3}$$

$$\frac{\partial \mathbf{u}}{\partial t} + \mathbf{u} \cdot \nabla \mathbf{u} = -\frac{\nabla p}{\rho} - g\mathbf{e}_z \tag{4}$$

$$w = \frac{\partial \eta}{\partial t} \quad \text{at } z = -d \tag{5}$$

$$(-u_x \frac{\partial \eta}{\partial x} + u_z) = \frac{\partial \eta}{\partial t} \qquad \text{at } z = \eta \tag{6}$$

$$p = 0 \qquad \text{at } z = \eta \tag{7}$$

Where $\eta(x, y, t)$ is the wave height with reference to the mean ocean surface. Since the fluid is assumed irrotational we can define a velocity potential $\phi(x, y, z, t)$. By the definition of the velocity potential, we can substitute ϕ in the above equations (3-7), rewrite (4) into a Bernoulli equation while inserting condition (7), to transform the problem to:

$$\nabla^2 \cdot \phi = 0 \tag{8}$$

$$\frac{\partial \phi}{\partial t} + \frac{1}{2}|\nabla \phi|^2 + g\eta = 0 \quad \text{at } z = \eta \tag{9}$$

$$\frac{\partial \phi}{\partial z} = 0 \quad \text{at } z = -d \tag{10}$$

$$-\frac{\partial \phi}{\partial x}\frac{\partial \eta}{\partial x} + \frac{\partial \phi}{\partial z} = \frac{\partial \eta}{\partial t} \quad \text{at } z = \eta \tag{11}$$

To solve this problem we want to move the boundary conditions using the Taylor expansions for ϕ. We want to linearize the problem to simplify it, and we thus assume that u, w, η, and ϕ are all of the same order and neglect all higher order term. This means that for example:

$$(\frac{\partial \phi}{\partial z})_{z=\eta} = (\frac{\partial \phi}{\partial z})_{z=0} + \eta(\frac{\partial \phi}{\partial z})^2_{z=0} + ... \approx \frac{\partial \phi}{\partial z}_{z=0} \tag{12}$$

Then (8)-(11) simplifies to the linearized problem:

$$\nabla^2 \cdot \phi = 0 \tag{13}$$

$$\frac{\partial \phi}{\partial t} + g\eta = 0 \qquad \text{at } z = 0 \tag{14}$$

$$\frac{\partial \phi}{\partial z} = 0 \qquad \text{at } z = -H \tag{15}$$

$$\frac{\partial \phi}{\partial z} = \frac{\partial \eta}{\partial t} \quad \text{at } z = 0 \tag{16}$$

1.1.2 The velocity potential and dispersion relation

Now assume that the waves profile propagates in the x-direction without loss of generalisation as $\eta(x,t) = asin(kx - \omega t)$ and that $\phi(x,y,t) = A(z)\eta(x,t)$. Further we assume that the ratio $a\lambda$ is small, such that we can make the solutions linear. Substituting our assumption on η into the Laplace equation (13) and using our linearity assumption in kinematic boundary conditions (15,16), then we get the following solution:

$$\phi(x,z,t) = \frac{\omega a}{k} \frac{cosh[k(d+z)]}{sinh(kd)} sin(kx - \omega t) \tag{17}$$

The phase speed of the waves follows from noting where the phase of the waves remains constant.

$$\frac{\partial(kx - \omega t)}{\partial t} = 0 \rightarrow c = \frac{\partial x}{\partial t} = \frac{\omega}{k} \tag{18}$$

Further, applying our solution of ϕ into the rewritten dynamic boundary condition (14) yields the dispersion relation:

$$\omega^2 = gk\, tanh(kd) \quad \text{or} \quad c = \sqrt{\frac{g}{k} tanh(kd)} \tag{19}$$

This shows that waves move slower with decreasing depth. In addition, for deep waves, $kd >> 1$, $c \approx \sqrt{g/k}$ such that waves with longer wavelength move with faster velocity. Meanwhile for shallow waves, $kd << 1$, $c \approx \sqrt{gd}$. Which means that in shallow water waves are non-dispersive.

When having a superposition of multiple waves, we have that the group velocity of those is:

$$c_g = \frac{\partial \omega}{\partial t} = \frac{1}{2}\left(1 + \frac{2kd}{sinh(2kd)}\right) c = \frac{1}{2}\left(1 + \frac{2kd}{sinh(2kd)}\right) \sqrt{\frac{g}{k} tanh(kd)} \tag{20}$$

Which means that the group velocity is always between 0.5c and 1c, for respectively deep and shallow water.

1.1.3 Particle velocity

A third way to describe the velocity of waves is that of the particles composing it. Taking the spatial derivatives of ϕ readily gives us the particle velocity. $\frac{\partial \phi}{\partial x} = u_x$ and $\frac{\partial \phi}{\partial z} = u_z$ so that:

$$u_x = \frac{\omega a \, cosh[k(d+z)]}{sinh(kd)} cos(kx - \omega t) \tag{21}$$

$$u_z = \frac{\omega a \, sinh[k(d+z)]}{sinh(kd)} sin(kx - \omega t) \tag{22}$$

When solving the equations $\frac{dx}{dt} = u_x$ and $\frac{dz}{dt} = u_z$ it results in two interesting orbits for deep and shallow water respectively:

$$x = \omega a e^{kz} cos(kx - \omega t) \quad \text{and} \quad z = \omega a e^{kz} sin(kx - \omega t) \tag{23}$$

$$x = \frac{\omega a}{kd} cos(kx - \omega t) \quad \text{and} \quad z = \omega a (1 + \frac{z}{h}) sin(kx - \omega t) \tag{24}$$

For deep water these velocities represent perfect circles with exponentially decaying radii, but perhaps more interesting in shallow waters they represent ellipses with decaying semi-axis in the z-direction. This results in straight lines at the bottom at the ocean. For water depths in between these cases there exists ellipses of which both semi-axis decay.

1.2 Second order linear theory

1.2.1 Wave elevation and particle velocity

Through a series of papers in the 1960s [Longuet-Higgins and Stewart, 1960, Longuet-Higgins and Stewart, 1961, Longuet-Higgins and Stewart, 1962, Longuet-Higgins and Stewart, 1964] Longuet-Higgins and Stewart released a series of papers extending linear wave theory to second order in terms of the wave elevation. Here they showed among other that groups of wave components induce longer waves which is known as bound infra-gravity waves. Through the following method they found the velocity induced by these additional wave components. In short, their work consisted of solving equations (3) through (6) with the Stokes approximation:

$$\mathbf{u} = \mathbf{u}^{(1)} + \mathbf{u}^{(2)} + ... \tag{25}$$

$$\phi = \phi^{(1)} + \phi^{(2)} + ... \tag{26}$$

$$\eta = \eta^{(1)} + \eta^{(2)} + ... \tag{27}$$

$$p + \rho g z = p^{(1)} + p^{(2)} + ... \tag{28}$$

Where the $^{(1)}$ terms satisfy the linearised equations and boundary conditions as in the previous section, and the $^{(1)}+^{(2)}$ terms satisfy the terms equations as to the quadratic terms. Using the solutions of the previous chapter and extending eq. (13-16) to also contain quadratic terms they found the following system of equations:

$$\nabla^2 \cdot \phi^{(2)} = 0 \tag{29}$$

$$g\eta^{(2)} = -(\frac{\partial \phi^{(2)}}{\partial t} + \frac{1}{2}(u^{(1)})^2 + \eta^{(1)}\frac{\partial^2 \phi^{(1)}}{\partial z \partial t}) \quad at\ z = 0 \tag{30}$$

$$(\frac{\partial^2 \phi^{(2)}}{\partial t^2} + \frac{\partial \phi^{(2)}}{\partial z}) = -\left[\frac{\partial}{\partial t}((u^{(1)})^2) + \eta^{(1)}\frac{\partial}{\partial z}(\frac{\partial^2 \phi^{(1)}}{\partial t^2} + \frac{\partial \phi^{(1)}}{\partial z})\right] \quad \text{at } z = 0 \tag{31}$$

$$\frac{\partial \phi^{(2)}}{\partial z} = 0 \qquad \text{at } z = -H \tag{32}$$

$$u^{(2)} = \nabla \phi^{(2)} \tag{33}$$

Solving these equations, details of which is left to the source, yield to the second order velocity $u^{(2)}$ and wave elevation $\eta^{(2)}$:

$$\phi^{(2)} = -K \sum_{m,n} \frac{a_m a_n c_g}{gH\theta - c_g^2} \frac{cosh\Delta k(z+H)}{cosh\Delta kH} \frac{sin(\Delta kx - \Delta\omega t)}{\Delta k} \tag{34}$$

$$u^{(2)} = -K \sum_{m,n} \frac{a_m a_n c_g}{gH\theta - c_g^2} \frac{cosh\Delta k(z+H)}{cosh\Delta kH} cos(\Delta k - \Delta\omega t) \tag{35}$$

$$\eta^{(2)} = \frac{-K}{g} \sum_{m,n} \frac{a_m a_n c_g^2}{gH\theta - c_g^2} cos(\Delta k - \Delta\omega t) - \frac{1}{g} \sum_{m,n} \frac{a_m a_n c_g^2}{sinh^2 kH} cos(\Delta kx - \Delta\omega t) \tag{36}$$

$$K = \frac{\omega^2 cosh(2kH)}{2sinh^2 kH} + \frac{1}{4} \frac{d}{d\omega} \left(\frac{\omega^3}{sinh^2 kH} \right) = \frac{\sigma^2}{4sinh^2(kh)} \frac{sinh(4kH) + 3sinh(2kH) + 2kH}{sinh(2kH) + 2kH} \tag{37}$$

$$\theta = \frac{tanh(\Delta kH)}{\Delta kH} \tag{38}$$

Summing these then yield the total velocity and wave elevation up to the second order of wave ampltitude. $\phi = \phi^{(1)} + \phi^{(2)}$ and $\mathbf{u} = \mathbf{u}^{(1)} + \mathbf{u}^{(2)}$. Interestingly this expressions means waves interact with themselves and induces a constant in time second order velocity in the direction of propagation. On the other hand, when there are multiple wave components they interact with each other in such a way that the velocity oscillate with the wave number and frequency of the wave envelope. This is in contrast to the first order effect where only the local wave amplitude determine the local particle velocity. Either way this second order effect is caused by what Longuet-Higgins and Stewart labeled radiation stress, and its effect is an infra-gravity wave which is bound with to the wave envelope and propagades at its speed.

1.2.2 Stokes drift

While the first order approximation of particle movement in the long wave model tells us that particle moves in closed orbits around a center point, this is never the case in real applications as the particle drifts along the direction of the waves. To see this effect it is necessary to Taylor expand $\frac{d\xi}{dt} = u_x$ again, but this time keep another term in the expansion of u_x. The following are due to [Ursell, 1953]:

$$\frac{d\xi}{dt} = u_x(x,z,t) \approx u_x(x_0,z_0,t) + (x-x_0)(\frac{\partial u_x}{\partial x})_{x_0,z_0} + (z-z_0)(\frac{\partial u_z}{\partial z})_{x_0,z_0} \tag{39}$$

Where (x_0, z_0) is the location of the particle when there is no waves present. This equation will be expressed with $u^{(1)}$ and $u^{(2)}$ separately. The distances in eq. (39) for the first order effects can be expressed as:

$$x - x_0 = \int_0^t u^{(1)}(x_0, z_0, t')dt' = -a\frac{cosh[k(z_0 + H)]}{sinh(kH)}sin(kx_0 - \omega t) \tag{40}$$

And similarly for $z - z_0$. Solving eq. 39 and averaging it over 1 period of the wave component yields the average Stokes drift due to the first order velocity in the horizontal direction per time as:

$$\bar{u_S}^{(1)} = \sum_n a_n^2 \omega_n k_n \frac{cosh(2k_n(z_0 + h))}{2sinh^2(k_1 h)} \tag{41}$$

Similarly for the second order effect:

$$\begin{aligned} x - x_0 = \int_0^t u^{(2)}(x_0, z_0, t')dt' &= \int_0^t -K \sum_{m,n} \frac{a_m a_n c_g}{gH\theta - c_g^2} \frac{cosh\Delta k(z_0 + H)}{cosh\Delta kH} cos(\Delta k x_0 - \Delta\omega t)dt \\ &= -Kc_g \left[\sum_{m=n} \frac{a_m a_n}{gh - c_g^2} t + \sum_{m!=n} \frac{a_m a_n c_g}{gH\theta - c_g^2} \frac{cosh\Delta k(z_0 + H)}{cosh\Delta kH} \frac{sin(\Delta k x_0 - \Delta\omega t)}{\Delta\omega} \right] \end{aligned}$$

Now the Taylor expansion (39) will create fourth order terms. This will be neglected as we are only interested in effects up to second order. Thus while only keeping the second order terms, time averaging this effect it is noticed that only terms where $m = n$ is not cancelled and the Stokes drift from the second order effects are:

$$\bar{u_S}^{(2)} = \frac{-Kc_g}{gh - c_g^2} \sum_n a_n^2 \tag{42}$$

And the total Stokes drift to second order are:

$$\bar{u_S} = \sum_n \left[a_n^2 \omega_n k_n \frac{cosh(2k_n(z_0 + h))}{2sinh^2(k_1 h)} - a_n^2 \frac{Kc_g}{gh - c_g^2} \right] \tag{43}$$

Where the first term corresponds to the second order effect from the first order estimation of the wave velocity, and the second term corresponds to the second order estimation.

1.3 Processes of changing properties

Before waves hit the shelf seas, their amplitude, direction, wave number are primarily generated by wind, quadruplet wave-wave interaction, and white-capping. As they reach shallower waters the limited water depth affects these processes and influence the evolution of the waves in new ways. The limited water depth makes the waves move slower, resulting in energy bunching and

Table 1: Relative importance of of various processes affecting the evolution of waves in coastal waters.

Process	Oceanic waters	Shelf seas	Nearshore
Wind generation	XXX	XXX	X
Quadruplet wave-wave interactions	XXX	XXX	X
White-capping	XXX	XXX	X
Bottom friction	-/X	XX	XX
Bottom refraction / Shoaling	-	XX	XXX
Breaking (depth-induced)	-	XX	XXX
Triad wave-wave interactions	-	X	XX
Reflections	-	-	X/XX
Diffraction	-	-	X

XXX = dominant, XX = significant, X = of minor importance, - = negligible
[Battjes, 1994] [Holthuijsen, 2010]

thus higher and potentially breaking waves, as well as the potential for new triad wave-wave interactions. The waves can now also "feel" the bottom, where they begin to reflect and experience bottom friction. This results in a model needing to take many more processes into account than in the ocean.

1.3.1 Shoaling

Consider a wave approaching a beach with a gentle slope. This wave will have its frequency retained, but due to the dispersion relation (19) its wavelength and phase speed will decrease since the depth decreases. These changing wave properties results in horizontal energy bunching that causes the amplitude of waves to increase while the wavelength decrease, an effect which is called shoaling. By looking at waves approaching the beach normally and creating a control surface where energy only enters and exits through the sides parallel to the beach, one can use conservation of energy to derive this change of amplitude:

$$\frac{1}{2}\rho g a_2^2 c_{g,2} = \frac{1}{2}\rho g a_2^1 c_{g,1} \tag{44}$$

So that,

$$a_2 = \sqrt{\frac{c_{g,1}}{c_{g,2}}} a_1 \tag{45}$$

Where a_2 is the amplitude towards the beach and a_1 the ocean, and c_g the group velocity as defined in (20). Thus, shoaling has the effect of theoretically increasing the amplitude to infinity as the depth decreases to zero. The theory breaks down before this can happen, and as the amplitude

grows other effects that decrease the amplitude also increase in importance.

1.3.2 Refraction

If the wave approaches the beach at an angle the wave will change direction towards the beach. Since the depth is decreasing towards the beach, the phase speed will be different along the wave crest. This induces a turning since the waves closer to the beach now move slower. To explain refraction it is necessary to define three-dimensional waves. Suppose the waves can be described as:

$$\eta = Hcos(\Omega) = Hcos(\mathbf{k}\cdot\mathbf{x} - \omega t) \quad \text{where} \quad \mathbf{k} = \begin{bmatrix} k_1 \\ k_2 \end{bmatrix} \text{ and } \mathbf{x} = \begin{bmatrix} x \\ y \end{bmatrix} \tag{46}$$

To see the role of k note that when we look along the crest of a wave, we have that $\Omega = 2n\pi$, and that the normal vector of a scalar function is $\mathbf{N} = \nabla\Omega = \mathbf{k}$. So $\mathbf{k}$ is the vector normal to the wave crest and is named the wave number vector. Further $\mathbf{k} = \frac{\mathbf{N}}{|\mathbf{N}|} = \mathbf{n}|\mathbf{k}| = \mathbf{n}k$, so $\mathbf{k}$ is nothing more than the wave number oriented in the wave direction. [Dean and Dalrymple, 1991]

By noting that $\nabla \times \mathbf{k} = \nabla \times (\nabla\Omega) = 0$, since the curl of a gradient is 0, we get that:

$$\begin{aligned} &\frac{\partial[k\,sin(\theta)]}{\partial x} + \frac{\partial[k\,cos(\theta)]}{\partial y} = 0 \rightarrow \\ &k\,cos(\theta)\frac{\partial\theta}{\partial x} + k\,sin(\theta)\frac{\partial\theta}{\partial y} = cos\theta\,\frac{\partial k}{\partial y} - sin\theta\,\frac{\partial k}{\partial x} \end{aligned} \tag{47}$$

By changing the coordinate system to one of (s,n), where s points along the wave direction and n normal to it:

$$\begin{aligned} x &= s\,cos\theta - n\,sin\theta \\ y &= s\,sin\theta + n\,cos\theta \end{aligned} \tag{48}$$

We can rewrite the above as:

$$(\frac{d\theta}{ds})_{ref} = -\frac{1}{c}\frac{\partial c}{\partial k} \tag{49}$$

Where m and n are coordinates along and normal to the wave crest. One can change this to Eulerian coordinates by the following substitutions: $\Delta\theta = \frac{d\theta}{ds}$ and $\Delta\theta = \frac{\Delta s}{c_g}$:

$$\frac{d\theta}{dt} = c_{\theta,ref} = -\frac{c_g}{c}\frac{\partial c}{\partial n} \tag{50}$$

Where the reference system is along the ray of wave energy.

So, a faster changing phase velocity will create a faster turning wave towards the location of shallower ocean. Since the phase velocity changes faster as the depth decreases, this effect also grows the closer to the beach the wave comes.

1.3.3 Wave interactions

Another way in which waves can be created is through non-liner wave-wave interactions, a process where wave components transfer energy between them through resonance. Note that no energy is added or removed from the system, it is only redistributed among them. There are two processes where this can occur, named triad- and quadruplet wave-wave interaction. In the first a pair of waves can form a diamond pattern with its own speed, length and direction with which a third wave can interact, and in the last two pair of waves can interact with each other.

For quadruplet wave-wave interaction to occur the waves need to fulfil the matching criteria:

$$\begin{aligned} f_1 + f_2 &= f_3 + f_4 \\ \mathbf{k}_1 + \mathbf{k}_2 &= \mathbf{k}_3 + \mathbf{k}_4 \end{aligned} \tag{51}$$

If these are fulfilled the waves will redistribute energy among themselves. Similarly for triad wave-wave interaction the condition reduces to:

$$\begin{aligned} f_1 + f_2 &= f_3 \\ \mathbf{k}_1 + \mathbf{k}_2 &= \mathbf{k}_3 \end{aligned} \tag{52}$$

This condition is impossible to fulfil in deep water because of the dispersion relation (13), but as the depth decreases it becomes close to being fulfilled and energy can begin to transfer. This often results in a second peak at double the frequency in spectrum, and sometimes also at higher multiples of two. A special case occurs when a unidirectional harmonic wave enters shallow water. Then it is possible for the wave to self-interact to create a harmonic with double the frequency. These so-called superharmonics are bound to the primary harmonic because of the shallow water and make the waves profile have sharper crests and flatter throughs. But as we will see in the bar-test Ch. (3.1) below, it is possible for these waves to become “free” and propagate independent of the primary wave if the depth increases again.

1.3.4 Dissipation

There exist three primary phenomena of energy dissipation: white-capping, depth-induced breaking, and bottom friction. Among these breaking is the least understood, but some efforts have been

made to explain it. Bottom friction is also a complicated phenomenon, which is dealt by various methods in numerical schemes.

White capping is the breaking of waves because of their steepness. By looking at the fact that the particle velocity u_x (24) cannot be higher than the forward speed of the waves c (19) [Miche, 1944] showed that the maximum height of a wave is:

$$H_{max} \approx 0.14L\, tanh(\frac{2\pi}{L}) \tag{53}$$

Waves can still white-cap below this limit, but H_{max} seems to be the upper limit. [Holthuijsen and Herbers, 1986]

[Hasselmann, 1974] theorizes that when waves white-cap they remove energy from the waves by acting as pressure pulses. Just downwind of the crest the weight of the white-cap acts against the rising sea surface and remove energy from the wave, which in turn is transferred to turbulence and currents. The result is that of reducing the amplitude of the waves.

Depth-induced breaking is the most non-linear and poorly understood process, and most of our information regarding them are based on empirical information [Holthuijsen, 2010]. Breaking limits the maximum height of waves because when they reach a certain height they must break. This maximum limit is in the range of $0.5 < \frac{H_{max}}{d} < 1.5$ depending upon the local bottom slope and surface conditions.

When waves break into spilling, plunging, collapsing, or surging the energy are again as in white-caps transferred to turbulence and currents. To estimate this this energy loss one can model the energy loss as the dissipation in a hydraulic jump. Further one says that every breaking wave have a height H_{max}. Then the energy loss is:

$$D_{surf,wave} = -\frac{1}{4}\alpha_{BJ}\rho g f_0 H_{max}^2 \tag{54}$$

Where f_0 is the zero-crossing frequency, and $\alpha_{BJ} \approx 1$ is a tuneable coefficient.

Bottom friction is a term that covers all transfer of energy from the waves to the boundary layer at the bottom of the ocean. Through motion of the particles in the ocean there is created a thin turbulent boundary layer at the bottom, and the energy for this layer is provided by the waves above it. The exchange of energy is determined by the rather complicated geometry of the bottom and the wave field itself. In addition, these might again affect each other.

One way to model this exchange of energy is to make use of eddy-viscosity models. Here one models the turbulent layer with parameters about the bottom. For sandy bottoms the only parameters that seem to determine the friction is the normalized bottom roughness $\tilde{k} = \frac{k_N}{a_{rms,bottom}}$,

where k_N is the bottom roughness length and $a_{rms,bottom}$ is the root-mean-square amplitude of near-bottom orbital excursion, and a parameter describing how much the waves can set the sandy bottom in motion :

$$\psi = C_{bfr,skin} \frac{u^2_{rmns,bottom}}{(\frac{\rho_{sand}}{\rho_{water}} - 1) g D_{grain}} \tag{55}$$

Where $C_{bfr,skin}$ is the coefficient for skin friction. [Tolman, 1995]

1.3.5 Generation of IG waves by breaking

Another process which generate infra-gravity waves in addition to the radiation stress shown in Ch.(1.2.1) is that of a varying surf zone. [Longuet-Higgins and Stewart, 1962] showed that their infra-gravity waves are bound to the wave envelope as they travel, as their wave component are therefor called a bound infra-gravity wave. But they also found while comparing their results to measurements that the bound wave is released at the breakpoint of the wave, and become a free wave. They do not however provide an explanation for this effect.

To answer this question [Symonds et al., 1982] develops a model by assuming that the point where waves begin breaking can vary, which they do when the amplitude of the incoming waves break. They found that the time variation of the breakpoint position can generate waves at the group period of the incoming waves. This new wave component is free to propagate at its own celerity, and would be reflected off the shore and propagate seawards.

[Symonds et al., 1982] compared their result to that of [Longuet-Higgins and Stewart, 1964] to find the relative importance of the two. Looking at the factor ζ_F/ζ_0 where ζ_F is the bound infra-gravity components of Longuet-Higgins and Stewart, and ζ_0 is the amplitude of the set-up about to the mean set-up found by Symonds et al. At the shore $\zeta_F/\zeta_0 \approx 0.25$ for a wave period of 10s, beach angle of 0.02 rad, and mean of the breakpoint at $X = 100$m. Assuming that the propagating wave is not losing energy, the amplitude of the free wave will decrease like $(h_b/h)^{1/4}$. This causes the same ratio to be $\zeta_F/\zeta_0 \approx 0.41$ at $x = 10X$.

Hence in the surf zone and near shore the effects of the free infra-gravity wave created by the moving break point seems to be more important than the bound infra-gravity wave moving with the wave groups.

1.4 Nwogus equations

In this chapter we begin with the work of [Nwogu, 1993] where he created a set of governing equations describing the ocean surface. I will follow the work of [Roeber et al., 2010] to express transported variables as conserved variables.

These equations are derived from a Taylor expansion of the Euler equations of motion, and thenceforth depth-integrated to remove the vertical dependence of the variables. The vertical velocity is then assumed to vary linearly over the depth.

With a stationary bathymetry, and the assumption of small amplitude long period waves, the equations of Nwogu in vector notation is expressed as:

$$\begin{aligned} \eta_t + \nabla[(h+\eta)\mathbf{U}] + \nabla \cdot \{(\frac{z_\alpha^2}{2} - \frac{h^2}{6})h\nabla(\nabla \cdot \mathbf{U}) + (z_\alpha + \frac{h}{2})h\nabla[\nabla \cdot (h\mathbf{U})]\} = 0 \\ \mathbf{U}_t + \mathbf{U}(\nabla \cdot \mathbf{U}) + g\nabla\eta + \{\frac{z_\alpha^2}{2}\nabla[\nabla \cdot (h\mathbf{U})]\}_t = 0 \end{aligned} \tag{56}$$

Where η is the free surface elevation, (u, v) is horizontal flow velocities, h is the bathymetry depth from the reference still water level, and z_α is the vertical reference position at which the velocities are determined. z_α is defined as a percentage of the reference depth s.t. $z_\alpha = 0$ is the reference at the surface, and $z_\alpha = -h$ is the reference at the bottom. Since z_α approximates the fully dispersive problem, one can choose the velocity variable u_α to minimize the error for the depths used in the current model. (See Ch. 1.4.4)

The advantage of these equations compared to the earlier Boussinesq equations by [Peregrine, 1967] is the extra dispersion term in the continuity equation which makes the model have lower error in intermediate to deep water.

1.4.1 Conserved variable formulation

The equations of Nwogu are not stated in conserved form which becomes a problem when discussing wave breaking/discontinuities. These depth integrated Boussinesq equations cannot handle wave overturning, so it is necessary to reformulate the equations in conservative form such that these situations can be resolved. (See Ch. 2)

Volker et al. showed that Nwogus equations could be reformulated in terms of the conserved qualities H, Hu, Hv instead of η, u, v, where $H = h+\eta$. In conserved form the continuity equation is expressed by rewriting the equation as:

$$\boxed{H_t + (Hu)_x + (Hv)_y + \psi_c = 0}$$

Where,

$$\begin{aligned}\psi_c = [(\frac{z_\alpha^2}{2} - \frac{h^2}{6})h(u_{xx} + v_{xy}) + (z_\alpha + \frac{h}{2})h((hu)_{xx} + (hv)_{xy})]_x \\ +[(\frac{z_\alpha^2}{2} - \frac{h^2}{6})h(u_{xy} + v_{yy}) + (z_\alpha + \frac{h}{2})h((hu)_{xy} + (hv)_{yy})]_y\end{aligned} \tag{57}$$

is a term describing dispersion in the continuity term.

For the momentum equation it is necessary to multiply Nwogus momentum equation by H as well as his continuity equation by u and v respectively. Doing some algebraic and calculus exercises yields the following systems for the momentum equation in the horizontal plane:

$$\boxed{\begin{aligned}x - dir : P_t + (Hu^2)_x + (Huv)_y + Hg\eta_x + \psi_{P2} - H_t\psi_P + u\psi_c = 0 \\ y - dir : Q_t + (Hv^2)_y + (Huv)_x + Hg\eta_y + \psi_{Q2} - H_t\psi_Q + v\psi_c = 0\end{aligned}}$$

Here P and Q involves all terms of that variable with time derivates, and are equal to:

$$P = (Hu + \frac{z_\alpha^2}{2}[Hu_{xx}] + z_\alpha[H(hu)_{xx}]) \tag{58}$$

$$Q = (Hv + \frac{z_\alpha^2}{2}[Hv_{yy}] + z_\alpha[H(hv)_{yy}]) \tag{59}$$

ψ_P and ψ_Q contains all terms parabolic terms not dependent on time:

$$\psi_P = \frac{z_\alpha^2}{2}u_{xx} + z_\alpha(hu)_{xx} \tag{60}$$

$$\psi_Q = \frac{z_\alpha^2}{2}v_{yy} + z_\alpha(hv)_{yy} \tag{61}$$

Simiarly ψ_{P2} and ψ_{Q2} contains the time dependent xy-terms:

$$\psi_{P2} = \frac{z_\alpha^2}{2}Hv_{xyt} + z_\alpha(Hhv)_{xyt} \tag{62}$$

$$\psi_{Q2} = \frac{z_\alpha^2}{2}Hu_{xyt} + z_\alpha(Hhu)_{xyt} \tag{63}$$

Finally, ψ_c is the term from the continuity equation (57).

Now the continuity equation together with the momentum equations can be written in a con-

servative vector form as:

$$\mathbf{U}_t + \mathbf{F}(\mathbf{U})_x + \mathbf{G}(\mathbf{U})_y + \mathbf{S}(\mathbf{U}) = 0 \tag{64}$$

Where,

$$\mathbf{U} = \begin{bmatrix} H \\ P \\ Q \end{bmatrix} \; \mathbf{F}(\mathbf{U}) = \begin{bmatrix} Hu \\ Hu^2 + \frac{1}{2}g\eta^2 + g\eta h \\ Huv \end{bmatrix} \; \mathbf{G}(\mathbf{U}) = \begin{bmatrix} Hv \\ Huv \\ Hv^2 + \frac{1}{2}g\eta^2 + g\eta h \end{bmatrix}$$

$$\mathbf{S}(\mathbf{U}) = \begin{bmatrix} \psi_c \\ -g\eta h_x + u\psi_c - H_t\psi_P + \psi_{P2} \\ -g\eta h_y + v\psi_c - H_t\psi_Q + \psi_{Q2} \end{bmatrix} \tag{65}$$

The variables U now contain the evolution variables, $\mathbf{F}(\mathbf{U})$ and $\mathbf{G}(\mathbf{U})$ the homogenous parts of the nonlinear shallow water equations and $\mathbf{S}(\mathbf{U})$ contains the local acceleration and source terms.

1.4.2 Additional source terms

Additional terms can be added to equations to add or remove mass given that the units are consistent with the other terms. While BOSZ include four additional source terms, I will describe just the two which is necessary for this paper.

[Wei et al., 1999] proposes that the wavemaker can be introduced to Boussinesq models through a source function in the continuity term. This source function is analogous to adding or subtracting mass, which it does over a bell curved area to ensure a smooth transition between the wavemaker and the rest of the model.

The produced wavefield are generated through a superposition of individual waves of single frequencies, amplitudes, and direction through the equation:

$$\psi_{wm} = \sum_{i=1}^{M_\omega} \sum_{j=1}^{M_\theta} D \, \cos(ky \, \sin\theta - \omega t + \phi) \tag{65}$$

Where D, k, ω, ϕ are the amplitude, wave number, angular velocity, and a phase shift of the waves respectively. See Ch. (2.1.6) for how to include it numerically.

Another useful term to model is the bottom friction based on the manning friction n. τ_1 and τ_2

describe this friction in x- and y- direction, and is given by:

$$\begin{aligned}\tau_1 &= gn^2 H^{-\frac{4}{3}} u\sqrt{u^2+v^2} \\ \tau_2 &= gn^2 H^{-\frac{4}{3}} v\sqrt{u^2+v^2}\end{aligned} \tag{66}$$

These equations describe the friction associated with surfaces and roughness's much smaller than the depth. To include these into the model it is necessary to add them in the source term **S**(**U**) described in Ch. (1.4.1) multiplied by the variable H. To describe friction across large objects or flow through porous mediums other models must be used as described in Ch. (1.4.3).

1.4.3 Flow through porous layers

The governing equations of the fluids can be modified to incorporate the effects of partial transmission and reflection about a porous layer. The BOSZ model incorporates the idea from [Nwogu and Demirbilek, 2001], where the equations are written in terms of the discharge velocities to ease the matching of velocities across the structure interface. This is done by replacing u with u/n, where n is the porosity of the structure. Further they add energy dissipation terms to the momentum equation to account for friction inside the structure:

$$\begin{aligned}\eta_t + \nabla\cdot(\frac{\mathbf{u}_f}{n}) &= 0 \\ \eta_{\alpha,t} + ng\nabla\eta + \mathbf{u}_\alpha\cdot\nabla(\frac{\mathbf{u}_\alpha}{n}) + z_\alpha[\nabla(u_{\alpha,t}\cdot\nabla h) + (\nabla\cdot\mathbf{u}_{\alpha,t})\nabla h] & \\ +\frac{1}{2}[(z_\alpha+h)^2 - h^2]\nabla(\nabla\cdot\mathbf{u}_{\alpha,t}) + nf_l\mathbf{u}_\alpha + nf_t\mathbf{u}_\alpha|\mathbf{u}_\alpha| &= 0\end{aligned} \tag{67}$$

Where f_l and f_t are respectively laminar and turbulent friction factors. [Engelund, 1953] recommended that the factors should follow the following empirical relationships:

$$f_l = \alpha_0\frac{(1-n)^3}{n^2}\frac{\nu}{d^2} \quad f_t = \beta_0\frac{1-n}{n^3}\frac{1}{d} \tag{68}$$

Where ν is the kinematic viscosity of water, d is the characteristic stone size, α_0 and β_0 are empirical constants that range from 780 to 1500 and 1.8 to 3.6 respectively.

In the BOSZ model this is incorporated by an array of values for the above four variables, which can be updated for each time step. The new system is then solved for every location deemed to consist of a porous layer, typically a breakwater.

In this thesis I will also use this method to simulate an OWSC, since its mechanics also consist of partial transmission and reflection (see Ch. 7).

1.4.4 Dispersion properties

Linearizing the equations found in Ch. (1.4.1) and considering the depth as constant and in one dimension as in [Nwogu, 1993] yields the following linear system:

$$\begin{aligned} \eta_t + hu_{\alpha x} + (\alpha + \frac{1}{3})h^3 u_{\alpha xxx} = 0 \\ u_{\alpha t} + g\eta_x + \alpha h^2 u_{\alpha txx} = 0 \end{aligned} \tag{69}$$

Where $\alpha = \frac{1}{2}(\frac{z_\alpha}{h})^2 + \frac{z_\alpha}{h}$ and $z_\alpha = -0.531h$.

Now we look specifically at the single steady period waves:

$$\begin{aligned} \eta(x,t) = a\, sin(kx - \omega t) \\ u(x,t) = b\, sin(kx - \omega t) \end{aligned} \tag{70}$$

Inserting these into the above equations yield:

$$\begin{aligned} -a\omega + hbk - (\alpha + \frac{1}{3})h^3 bk^3 = 0 \\ -b\omega + gak + \alpha h^2 b\omega k^2 = 0 \end{aligned} \tag{71}$$

Which if we solve for the velocity magnitude b is:

$$b = \frac{a\omega}{kh(1 - (\alpha + \frac{1}{3})h^2 k^2)} \tag{72}$$

And thence the celerity of Nwogus equations:

$$C_{Nwogu} = \left[gh \frac{1 - (\alpha + \frac{1}{3})h^2 k^2}{1 - \alpha h^2 k^2} \right]^{1/2} \tag{73}$$

This is now compared to the celerity of linear wave theory discussed seen in eq. (19) such that $Relative\, error = C_{Nwogu}/C_{Linear}$. The relative error of Nwogus celerity is plotted below. As one can see in Fig. (2), the celerity of Nwogus equations is overestimated for short waves. This error is negligible, below 1% error, while the waves are in shallow waters where $kh < \pi$. It grows steadily in intermediate waters $\pi < kh < 2\pi$ up till around 12% error, at this point a 100m wavelength wave would be modelled to have a 112m wavelength.

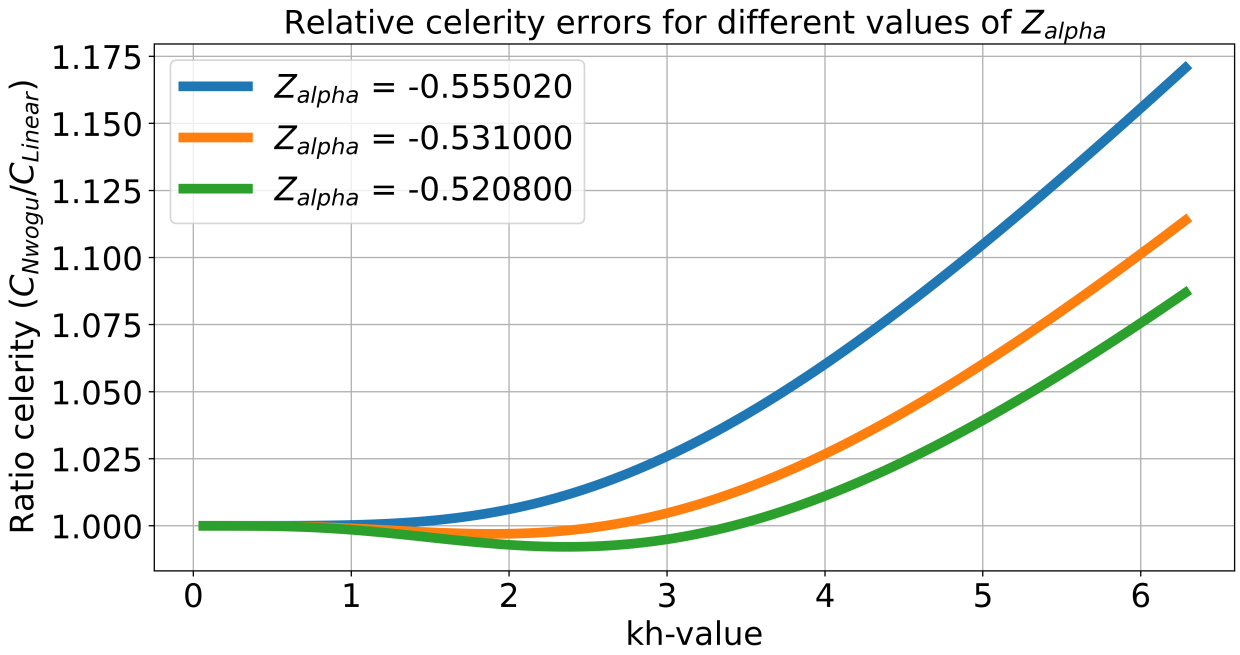

Figure 2: Relative celerity error for $z_\alpha = -0.55502h, -0.531h, -0.5208h$

Now the celerity has a high sensitivity on z_α. Changing this value changes the shape of the error curve, and generally a higher value of z_α makes the error less for higher kh-values. For example, looking at $z_\alpha = -0.5208h$ instead makes error between ± 8% for intermediate depth, while sacrificing accuracy for long waves.

It is therefore a matter of discussion what value of z_α is best to use, as for a given situation there will be a range of different khs in the domain and hence a range of z_αs. Different average optimal values have thus been proposed, for example [Nwogu, 1993] originally proposed $z_\alpha = -0.531h$ while [Roeber and Cheung, 2012] proposed $z_\alpha = -0.5208h$ to emphasize intermediate waves and [Simarro et al., 2013] recommended a value of $z_\alpha = -0.55502h$ to improve shoaling of high frequencies. In this paper I chose to use Nwogus original proposal, as this seem to be in the middle of the other two approaches and it prioritises long waves in shallow depths.

1.5 Lagrangian particle

While studying the effects of gravity waves on the motion of inertial particles [Santamaria et al., 2013] found a system of differential equations which describe their paths evolution.

By starting at the linear theory of ocean waves with the assumption of small amplitude long period waves, and specifically a monochromatic wave, they found that the motion of the inertial

particle is given by:

$$\begin{aligned} \frac{d\mathbf{x}}{dt} &= \mathbf{V} \\ \frac{d\mathbf{V}}{dt} &= \frac{\mathbf{u}-\mathbf{V}}{\tau} + \beta\frac{d\mathbf{u}}{dt} \end{aligned} \tag{74}$$

Where **x** are the particles location, **V** and **u** are respectively the particles and wave velocity. In the latter equation $\tau = a^2/3\beta\nu$ is the Stokes response time, where again a is the particles radius and ν is the kinematic viscosity of the fluid. $\beta = 3\rho_f/(\rho_f + 2\rho_p)$ in both the differential equation and the response time is a correction factor to the fact that the local density is changed by the particle.

Note that (Boffetta et al., 2013) dealt with the full 3D-case, but I have reduced the system to account for the fact that the model used in this thesis does not solve for the z-position.

In the following code (Ch. 2) I incorporated these equations into BOSZ by solving them for each timestep with a simple Euler forward scheme. Note that since these equations are ODE's for V and can be expressed as $\frac{d\mathbf{V}}{dt} = -a\mathbf{V} + \mathbf{F}, 1 > a > 0$, where **F** is treated as a constant forcing term, these equations are stable for all timesteps with Euler forward [Gustafsson et al., 1995].

1.6 Recreation of drifters path in ocean

A central problem for the verification of the model (2) is the comparison of movement of actual drifters recording through a stereo camera setup to the simulated Langrangian drifters described above Ch. (5). To perform this comparison, it is necessary to transform the pixel coordinates of the two cameras to 3d world coordinates. This is done with the same method described by [Bjørnestad et al., 2021].

To transfer a real-world coordinate to the pixel coordinate it is necessary to linearly transform them by two means: an extrinsic matrix to transform the world coordinates to camera coordinates, and an intrinsic matrix to compensate for distortions on the cameras vision. This transformation looks like:

$$\begin{bmatrix} u \\ v \\ 1 \end{bmatrix} = \begin{bmatrix} f_x & s & c_x \\ 0 & f_y & c_y \\ 0 & 0 & 1 \end{bmatrix} \begin{bmatrix} r_{11} & r_{12} & r_{13} & t_1 \\ r_{21} & r_{22} & r_{23} & t_2 \\ r_{31} & r_{32} & r_{33} & t_3 \end{bmatrix} \begin{bmatrix} X \\ Y \\ Z \\ 1 \end{bmatrix} \tag{75}$$

Where (u, v) are our pixel coordinates and (X, Y, Z) the world coordinates. The right matrix is the extrinsic coordinates and consists of rotation and translation elements r_{ij} and t_i respectively

which rotates and translate the world coordinates to match the cameras field of view. The left matrix is the intrinsic matrix which consists of compensation for the focus f_x, f_y of the camera which changes how large objects appear. The c_x,c_y elements translates the location of the pinhole if it is not in the middle of the camera. Lastly s compensates for the skewness of camera axes.

These parameters might be different for different locations in the cameras view as well, due to imperfections in the camera's construction. It might therefore be necessary to create multiple such transformations for different locations in the field of view.

Now to go the other way it is necessary to use a stereo camera to determine the third world coordinate. This is done by using geometry and the fact that the two cameras are defined to have the same Y and Z coordinates. Then the Z value of the world point of one pixel is:

$$Z = \frac{f_x b}{d} \tag{76}$$

Where Z is the coordinate in the cameras world coordinate system, f_x is the focal length of this camera, b is the distance between the cameras and d is the disparity of x-coordinates between the two cameras.

In this paper this model is on the other hand left to MATLAB to solve with its inbuilt Camera Calibration library. Here they provide both functions to calibrate, that is to find the intrinsic and extrinsic matrices of the stereo cameras, and to triangulate, which is to change from pixel coordinates to world coordinates. But when working backwards from pixel coordinates to world coordinates the model described above does not know which world coordinates to solve for. Hence MATLAB describes the world points in the following coordinate system:

x: towards camera 2 from camera 1
y: downwards of camera 1
z: outwards of camera 1

Hence it is necessary to perform a change of basis. If multiple ground control points inside the pictures have known coordinates in both the cameras coordinates and for example in WGS84, then it is possible to change the coordinates through:

$$P_{C \to WGS84}[\mathbf{x}]_C = [\mathbf{x}]_{WGS84} \tag{77}$$

Where the change of basis matrix the same described in [Lay et al., 2016].

Thus, if the cameras are calibrated and the pixel locations of drifters are known it is possible to calculate the corresponding location in world coordinates.

1.7 Recreating 2D spectra from 1D spectra

A common problem in is the fact that buoys often record a local wavefield with a 1D spectrum instead of a full 2D spectrum. Hence it is necessary to somehow recreate the full 2D spectrum. Consider the two-dimensional simple harmonic wave propagating in x, y-space:

$$\eta = a\,cos(\omega t - kx + \alpha) \tag{78}$$

Now since every wave carries energy, an entire wavefield can be described using the two parameters θ and f from k and ω respectively. The two-dimensional variance density is the function:

$$E = E(f, \theta) \quad [m^2/Hz/angle] \tag{79}$$

Describing the concentration of energy for one frequency and angle. Further the one-dimensional frequency spectrum can be defined as:

$$E = E(f) = \int_0^{2\pi} E(f, \theta) d\theta \tag{80}$$

[Holthuijsen, 2010]. Which implies that,

$$E(f, \theta) = E(f) \cdot D(\theta) \quad \text{where} \int_0^{2\pi} D(\theta) d\theta = 1 \tag{81}$$

Recreating the two-dimensional from a one-dimensional spectrum is then a matter of finding the function $D(\theta)$, which is generally unknown. [Pierson Jr et al., 1971] attempted to estimate the function as:

$$D(\theta) = \begin{cases} \frac{2}{\pi} cos^2\theta & \text{if } |\theta| \leq \frac{\pi}{2}, \\ 0 & \text{else} \end{cases}$$

Hence if one knows at least the 1-dimensional spectrum it is possible to estimate the two-dimensional spectrum with the assumption that the directional function is described by a $cos^2 x$ function.

2 BOSZ model

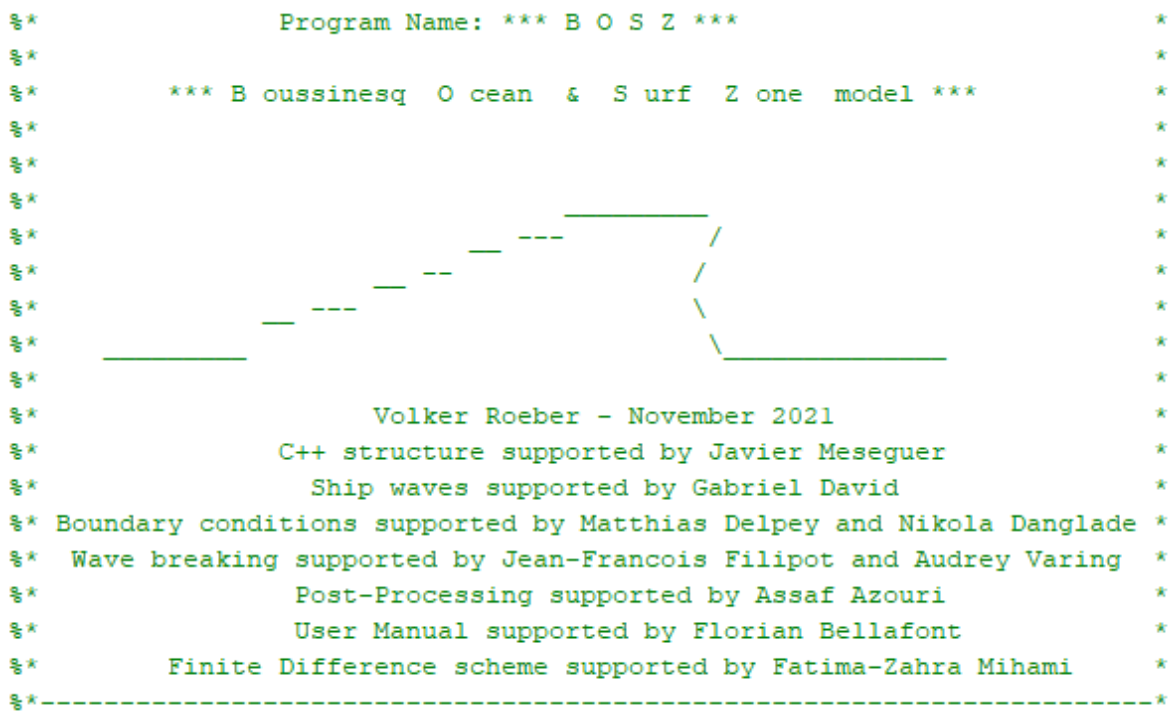

Figure 3: First lines of the BOSZ code.

2.1 Numerical method

The BOSZ method uses a variety of numeric methods to solve its governing equations. It uses finite volumes and finite differences for the different terms. The finite volume methods solve for the fluxes with a Riemann solver at all cell interfaces. Here it uses a reconstruction method to find the Riemann solutions. To solve for the time steps, it further uses a direct finite difference scheme.

Looking back at Ch.(1.4.1) the terms $\mathbf{F}(\mathbf{U})$ and $\mathbf{G}(\mathbf{U})$ are solved using the Riemann solver supported finite volume scheme, and the acceleration and source terms inside $\mathbf{S}(\mathbf{U})$ are solved with a finite difference, except ψ_{P2} and ψ_{Q2} which are dealt with separately.

2.1.1 Finite volume calculation

The governing equations have the nonlinear shallow water equations as a subset, which are flux driven non-linear hyperbolic systems. The additional parts of Nwogus equations introduce

parabolic dispersion terms, but these corrections are rather small in comparison. This means that our model is prone to develop discontinuities [LeVeque and Leveque, 1992], and our solver therefor need to be able to resolve these shocks which develop naturally in water because of the effects discussed in Ch. (1.3.4).

One such numeric scheme which can resolve hyperbolic shocks are the finite volume method. This caters to the problem since the method works on conservative systems, and it approximates breaking waves by moving them along the domain as discontinuities [LeVeque and Leveque, 1992]. It is also the reason they needed to rewrite Nwogu's equations in conservative form, since the finite volume methods demands it.

Here I derive the finite volume method used in the BOSZ model. Starting with the governing equation (64), integrate across the area of one cell, which is constant in size to every other cell:

$$\int_A \mathbf{U}_t dA + \int_A \mathbf{F}(\mathbf{U})_x dA + \int_A \mathbf{G}(\mathbf{U})_y dA \int_A \mathbf{S}(\mathbf{U}) dA = 0 \tag{82}$$

Now define $\bar{\mathbf{U}} = \frac{1}{n}\int_A \mathbf{U} dA$, $\bar{\mathbf{S}} = \frac{1}{n}\int_A \mathbf{S} dA$, and $\mathbf{H}(\mathbf{U}) = \begin{bmatrix} \mathbf{F}(\mathbf{U}) \\ \mathbf{G}(\mathbf{U}) \end{bmatrix}$, then the above equation is identical to:

$$A\bar{\mathbf{U}}_t + \int_A \nabla \cdot \mathbf{H} + A\bar{\mathbf{S}} = 0 \tag{83}$$

Using Gauss divergence theorem on the remaining integral yields:

$$\int_A \nabla \cdot \mathbf{H} = \oint_{\partial A} \mathbf{H} \cdot \mathbf{n} dl \tag{84}$$

Where $\mathbf{n}$ denote an outward facing normal. By further assuming that $\mathbf{H}$ is constant along each boundary they can rewrite the equations into:

$$\bar{\mathbf{U}}_t = -\frac{1}{A}\sum_l \mathbf{H} l - \bar{\mathbf{S}} \tag{85}$$

Here l is the length of each side and A the area of the cell. Writing out the summation sign and introduction location indexes they get:

$$\bar{\mathbf{U}_{i,j_t}} = -\frac{1}{\Delta x}(\mathbf{F}_{i+\frac{1}{2},j} - \mathbf{F}_{i-\frac{1}{2},j}) - \frac{1}{\Delta y}(\mathbf{G}_{i,j+\frac{1}{2}} - \mathbf{G}_{i,j-\frac{1}{2}}) - \bar{\mathbf{S}} \tag{86}$$

Where the index $i + 1/2$ and $j + 1/2$ mean the value of the variable at the interface in between the cells. The equations now state that the average value of our cell only changes by how much mass enters through the boundaries, an effect called flux, and how much our source creates or deletes.

The problem now consists of finding the values of this flux at the interfaces.

2.1.2 Flux calculation

The process of finding the flux is threefold: first a linear function is estimated over the cell to limit diffusion, then this function is slope-limited to limit oscillations, before these values are solved with a Riemann-problem solver.

The method used for reconstructing the fluxes are called MUSCL-TVD (Monotonic UpStream Centered Limited Total-Variation Diminishing). Instead of simply treating the value in each cell of constant or doing a simple interpolation, the idea of MUSCL-TVD is to find a second order linear approximation inside each cell. The forwards and backwards slopes are defined as:

$$\begin{aligned} f_{i,j} &= u_{i+1,j} - u_{i,j} \\ b_{i,j} &= u_{i,j} - u_{i-1,j} \end{aligned} \tag{87}$$

Here only the x-direction is shown, as this generalizes well to two dimensions. Further the ratio of slopes is:

$$r_{i,j} = \frac{b_{i,j}}{f_{i,j}} \tag{88}$$

Now the slope inside the domain is generally a linear combination of the backwards- and forwards difference given as:

$$\nabla i, j = \frac{(1-\Omega) f_{i,j} + (1+\Omega) n_{i,j}}{2} \tag{89}$$

Where Ω is a parameter which determines this linear combination. Inside BOSZ this parameter is $\Omega = 1$ which means only the backwards slope is used.

Now this approach has the problem that it is likely that the values at the interfaces are overshot and undershot from each side, which will introduce oscillations and instability to the scheme. To avoid this Total-Variation Diminishing slope limiters are used. Total variation is given as $TV(u) = \sum |u_{i+1} - u_i|$, and a scheme is total variation diminishing if $TV(u^{i+1}) \leq TV(u^i)$. Now this means that no further oscillations are added into the code [Gustafsson, 2007].

To ensure this a slope limiter $\phi(r_{i,j})$ is applied to our slope (89). The scheme to determine this slope limiter is called Superbee-SLIC which is defined as:

$$\phi(r) = \begin{cases} 2r & \text{if } r \leq 1/2, \\ 1 & \text{if } r \leq 1, \\ \min(0.5(1-\Omega+(1+\Omega)r, r, 2) & \text{else} \end{cases}$$

The final slope is then $\Delta_{i,j} = \phi(r_{i,j})\nabla_{i,j}$ such that the values at the interfaces is equal to:

$$\begin{aligned} u_{i+1/2,j} &= u_{i,j} + \frac{\Delta_{i,j}}{2} \\ u_{i-1/2,j} &= u_{i,j} - \frac{\Delta_{i,j}}{2} \end{aligned} \tag{90}$$

Now the last step is to solve the Riemann problem at each interface. This is done with two different Riemann solvers, the HLLC scheme of [Toro, 1997] for regions of breaking waves and second order upwind [Gustafsson, 2007] for the rest of the computational domain. Numerical details of the methods can be found in the respective sources.

The HLLC scheme of Toro is accurate at solving the discontinuities of the wave field and is robust for flows over irregular bathymetry. But it was specifically developed for solving shocks and is therefore not optimised to reduce numerical diffusion. The more oscillatory motion there is in the wave field, the more energy is lost with a pure HLLC approach. Therefor at locations not dealing with the issue of wave breaking the Riemann solution is instead solved with the second order upwind scheme. This means that the HLLC scheme is only used along the wavemaker, the sponge layer, and everywhere where the depth is lower than $2H_s$ in accordance with Ch. (1.3.4). In essence this makes the approach less diffusive by only keeping the high diffusive solver where it is necessary, and the computational cost lower as well.

2.1.3 Source term calculations

The source vector is the same as described in 1.4.1:

$$\mathbf{S}(\mathbf{U}) = \begin{bmatrix} \psi_c \\ -g\eta h_x - u\psi_c - H_t\psi_P + \psi_{P2} \\ -g\eta h_y - v\psi_c - H_t\psi_Q + \psi_{Q2} \end{bmatrix} \tag{65}$$

where,

$$\psi_c = [(\frac{z_\alpha^2}{2} - \frac{h^2}{6})h(u_{xx} + v_{xy}) + (z_\alpha + \frac{h}{2})h((hu)_{xx} + (hv)_{xy})]_x \\ +[(\frac{z_\alpha^2}{2} - \frac{h^2}{6})h(u_{xy} + v_{yy}) + (z_\alpha + \frac{h}{2})h((hu)_{xy} + (hv)_{yy})]_y \tag{57}$$

$$\psi_P = \frac{z_\alpha^2}{2}u_{xx} + z_\alpha(hu)_{xx} \quad \psi_Q = \frac{z_\alpha^2}{2}v_{yy} + z_\alpha(hv)_{yy} \tag{60 - 61}$$

$$\psi_{P2} = \frac{z_\alpha^2}{2}Hv_{xyt} + z_\alpha(Hhv)_{xyt} \quad \psi_{Q2} = \frac{z_\alpha^2}{2}Hu_{xyt} + z_\alpha(Hhu)_{xyt} \tag{62 - 63}$$

Here every term in $\mathbf{S}(\mathbf{U})$ can be estimated with finite central difference methods without the time dependent ψ_{P2} and ψ_{Q2}. By default second order central difference is used, but by input higher orders is possible to use.

For the cross terms and time dependence in ψ_{P2} and ψ_{Q2} a first order upwind scheme is used. These terms only contain terms containing cross spatial derivatives together with a time derivative. They are calculated at the end of one-time loop for the next loop.

The time derivative of these terms are the hard part, and they are calculated as follows for every cell to second order accuracy:

$$u_t = \frac{u^{n+1}(\Delta t^n)^2 + u^n[(\Delta t^{n+1})^2 - (\Delta t^n)^2].u^{n-1}(\Delta t^{n+1})^2}{\Delta t^{n+1} \cdot \Delta t^n \cdot (\Delta t^{n+1} - \Delta t^n)} \tag{91}$$

And similarly for $(hu)_t$,v_t and $(hv)_t$. Since these are calculated at the end of the time step, the $(n+1)$ terms are already calculated and can be used for the next loop. In essence this means that the backwards difference is used in time.

When this is calculated for every cell, it is then a repeat of the central differences above to calculate the remaining xy derivatives with the central difference.

2.1.4 Scheme in time

Now to progress the modelling in time a direct Runge-Kutta time integration is used. These schemes are particularly useful for the modelling of wavefields as can easily be implemented with a dynamic time step, which will be necessary given the constant changing of the maximum flow speed of the waves. While BOSZ includes TVD version of second, third, and forth-order time

integration methods, the second order is most common in the code and is calculated as:

$$\begin{aligned} w' &= w^n + \Delta t \cdot T(w^n) \\ w^{n+1} &= \frac{[(w' + w^n) + \Delta T(w')]}{2} \end{aligned} \tag{92}$$

Where w^n is any of the three variables of (86) in timestep n and $T(w^n)$ is the R.H.S. of the same equation. This means that all the above calculations must be done twice, once for the predictor w' and once for the final value of w^{n+1}.

To determine the time step Δt an adaptive time step based on the CFL condition [LeVeque and Leveque, 1992] is used. To calculate this condition the fastest moving information propagation must be known, and BOSZ uses the speed from the nonlinear shallow water equations for this basis, where:

$$U_{max} = \max(\sqrt{u_{i,j}^2 + v_{i,j}^2} + \sqrt{gH_{i,j}}) \tag{93}$$

Which is the velocity of the particles plus the shallow water celerity. Then the CFL conditions become:

$$\Delta t = c \cdot \min(\frac{dx}{U_{max}}, \frac{dy}{V_{max}}) \tag{94}$$

Where c is the Courant number, a number $0 < c \leq 1$ meant to ensure that information does not propagate longer than one grid cell. In BOSZ the Courant number is defaulted to 0.5.

2.1.5 Retrieving physical variables

The variables solved for through Ch. (2.1.1 - 2.1.4) are just the variables H,P, and Q, but we want to know η, u, and v. To find η is as trivial as to solve $\eta = H - h$ for every grid cell, but u and v is instead defined by the equations:

$$
\begin{aligned}
P_{i,j} =& Hu + \frac{z_\alpha^2}{2}[Hu_{xx}] + z_\alpha[H(hu)_{xx}] \approx \\
& (Hu_{i,j}) + \frac{z_{\alpha_{i,j}}^2}{2}[H_{i,j}\frac{u_{i+1,j} - 2u_{i,j} + ui - 1, j}{2}] + \\
& z_{\alpha_{i,j}}[H_{i,j}\frac{(hu)_{i+1,j} - 2(hu)_{i,j} + (hu)_{i-1,j}}{2}] \\
Q_{i,j} =& Hv + \frac{z_\alpha^2}{2}[Hv_{yy}] + z_\alpha[H(hv)_{yy}] \approx \\
& (Hv_{i,j}) + \frac{z_{\alpha_{i,j}}^2}{2}[H_{i,j}\frac{v_{i,j+1} - 2v_{i,j} + vi, j - 1}{2}] + \\
& z_{\alpha_{i,j}}[H_{i,j}\frac{(hv)_{i,j} - 2(hv)_{i+1,j} + (hv)_{i,j-1}}{2}]
\end{aligned}
\tag{95}
$$

Which when approximated with a central difference define the linear system $C_x u = P$ and $C_y u = Q$. Note that all the coefficients of the variables are constant for every time step and need not be calculated again for either any time step or for any of the two parts of the time integration. Also note that the two systems are independent, so they can be solved in any order or side by side.

For $i = 1, M$ and $j = 1, N$ the scheme must be altered and instead of the above:

$$
\begin{aligned}
P_{1,j} =& H_{1,j} z_{\alpha_{1,j}}[\frac{1}{z_{\alpha_{1,j}}} - \frac{z_{\alpha_{1,j}}}{\Delta x^2} - \frac{2h_{1,j}}{\Delta x^2}]u_{1,j} + \\
& H_{1,j} z_{\alpha_{1,j}}[\frac{z_{\alpha_{1,j}}}{2\Delta x^2} + \frac{h_{2,j}}{\Delta x^2}]u_{2,j} \\
P_{M,j} =& H_{M,j} z_{\alpha_{M,j}}[\frac{1}{z_{\alpha_{M,j}}} - \frac{z_{\alpha_{M,j}}}{\Delta x^2} - \frac{2h_{M,j}}{\Delta x^2}]u_{M,j} + \\
& H_{M,j} z_{\alpha_{M,j}}[\frac{z_{\alpha_{M,j}}}{2\Delta x^2} + \frac{h_{M-1,j}}{\Delta x^2}]u_{M-1,j}
\end{aligned}
\tag{96}
$$

And similarly for $Q_{i,1}$ and $Q_{i,N}$ The systems are solved by Thomas' algorithm and stored for each time step.

2.1.6 Internal wave generation

In Ch. (1.4.2) it was shown that the wavemaker term could be included in the model as:

$$
\psi_{wm} = \sum_{i=1}^{M_\omega} \sum_{j=1}^{M_\theta} D \, \cos(ky \, \sin\theta - \omega t + \phi) \tag{65}
$$

Though this add and removes mass, the sum of these effects is zero over one period. Hence if one places this wavemaker at the start or end of the computational domain it can be seen as modelling the incoming and outcoming mass from the deep ocean. To include this into the model it is necessary to discretize it, which is done as:

$$\psi_{wm_{i,j}} = \sum_{i=1}^{M_\omega} \sum_{j=1}^{M_\theta} D_{i,j} \cos(k_i y_j \sin\theta_j - \omega_i t + \phi_{i,j}) \tag{97}$$

M_ω and M_θ denotes here the number of frequencies and directions which the wave spectrum is composed out of. $\theta_(i,j)$ is a random phase angle which is necessary since the angle of individual waves are generally unknown. For example, wave spectral from buoys or SWAN do not contain information regarding phases. These are thus calculated at the beginning of the simulation and kept constant after this. To make the sure the model is repeatable, the random number seed is set to a fixed number such that two different runs will yield the same results, even though the phases are still randomly chosen.

To ensure the smooth transition from the wavemaker to the rest of the model, [Wei et al., 1999] wrote the source term as two terms: $G(x)$ a shape function which describes the distribution of the generating area and $s(y,t)$ explaining the strength of the generation:

$$\psi_{wm_{i,j}} = \sum_{i=1}^{M_\omega} \sum_{j=1}^{M_\theta} G(x)_{i,j} s(y,t)_{i,j} \tag{98}$$

$$G(x) = e^{-\beta_{i,j}(x_i - x_s)^2} \tag{99}$$

$$s(y,t) = D_{i,j}\, cos(k_i y_j\, cos\theta_j - \omega_i t + \theta_{i,j}) \tag{100}$$

Here $\beta_{i,j} \approx \frac{80}{\delta^2 L^2}$, where L is the wavelength of the individual wave, and δ is a factor for the width of the wavemaker set to 0.5. Lastly x_s is the centre of the wavemaker. Further Wei et al. found that:

$$D_{i,j} = \frac{2a_{i,j}\, cos(\theta_j)(\omega_i^2 - (\alpha + \frac{1}{3}) g k_i^4 h_j^3)}{\omega_i k_i B_i (1 - \alpha k_i^2 h_k^3)} \tag{101}$$

where $B_i = \sqrt{\frac{\pi}{\beta}} e^{-\frac{l_{i,j}^2}{4\beta}}$ and $l_{i,j} = k_i\, cos(\theta_j)$

A strength of this approach to wave generation is that since this source only adds and removes mass to represent the wave spectrum, it is nothing stopping other waves to travel through the wavemaker. For example, after simulating for a while some waves may be reflected from inside the domain and come back towards the wavemaker. This approach allows this wave to pass through

to the sponge layer behind the wavemaker to be absorbed, hence it simulates an open ocean.

But an issue to be aware with for discrete frequency bins is that the smallest bin determines when the incoming time series is repeated. Thus, a recycling of the time series occurs after $T = \frac{1}{min(\Delta f_i)}$ seconds. To avoid this, it is therefore necessary to ensure that there are enough bins to avoid this recycling for the planned computation time, which can be achieved by re-sample the spectrum through interpolation. Failure to do this might lead to artificial wave groups cluttering the output of the model.

2.1.7 Boundary conditions

The model allows for some different boundary conditions for each wall of the computational domain. These consists of reflective, radiating, or sponge layers at the end of the domain, as well as dry cells inside the domain. The easiest of which is the reflective boundary layers, of which the only necessary change is to change the sign of u and v on the boundary cells. Absorbing boundary conditions are Radiation- or sponge layers. Radiation boundary layers can also be directly imposed on the boundary as $\eta = -u\sqrt{H/g}$ and $\eta = u\sqrt{H/g}$ in the positive and negative x-direction respectively, and similarly in the y-direction. While this is very computationally efficient, the fact that these are based on hydrostatic flows means that they are more reflective than the alternative. Sponge layers are cosine functions imposed on the flux terms to transition the wave field to zero at the boundaries. These are almost not reflective at all and mimic the effect of having an open ocean around the computational domain.

Lastly there's the matter of dry cells in the domain. Since these there is no water to be simulated on these, BOSZ keep track of which cells contain water and only simulate those and the dry cells next to them. No more is necessary to simulate as the CFL makes sure the water can't travel further in one time step. To avoid dividing by zero, all cells are set to a negligible minimum water level of H_{min} and at the end of the computational step any cell with lower water level than $H < \frac{3}{2}H_{min}$ is treated as a dry cell. This ensures that numerical errors won't change the cells dryness.

2.2 Wave breaking

As discussed in Ch. (2.1.1) resolving wave breaking is hard in Boussinesq models since they can only be modelled as a discontinuity. Two problems come into action at once, first how to prevent a blow-up of the solution and secondly also how to further simulate it and lastly how to deal with the derivatives in the source terms which becomes large when the wave front becomes steeper and steeper. [Roeber, 2021]

There exist two potential solutions to these problems, deactivating the source term or adding diffusive eddy terms. Deactivate the source terms of the governing equations locally reduces the equations to the hyperbolic swallow water equations. A purely hyperbolic PDE allows discontinuities and, however the abrupt change of where and where not the source term is calculated can lead to instabilities in the model. Adding the eddy viscosity terms on the other hand keeps dispersion active in every cell. In addition, the dispersive nature of the eddies counter acts the formation of discontinuities and removes the instabilities of them [Roeber and Cheung, 2012].

2.2.1 Identification of breaking waves

The problem of identifying when the waves are beginning to break in depth-integrated models is notoriously difficult. Since overturning is impossible breaking is an approximation no matter what criteria and solution is used, but recent advances show that a kinematic or dynamic criteria works best [Varing et al., 2021] [Barthelemy et al., 2018]. The criteria included in the BOSZ model are either the Momentum gradient, Froude number, or the water depth to wave height ratio depending on the input to the model.

The momentum gradient criterion is that every cell is turned off if one of the following criteria is met:

$$\begin{aligned} |(Hu)_x| &> 0.5\sqrt{gH} \\ |(Hv)_y| &> 0.5\sqrt{gH} \end{aligned} \tag{102}$$

Where the factor 0.5 is chosen by the creator of the model by comparison with experimental data, and the derivatives are discretized with an upwind method as:

$$(Hu)_x = \frac{(Hu)_{i+\frac{1}{2},j} - (Hu)_{i-\frac{1}{2},j}}{\Delta x} \tag{103}$$

And similarly for $(Hv)_y$. This condition is then checked for every cell for every time step.

The Froude number can also be calculated at the surface by evaluating the velocities at the free surface. This can be done via the assumption of a quadratic velocity distribution in the z-direction as:

$$\begin{aligned} u^\eta &= u_{z_\alpha}\frac{1}{2}(z_\alpha^2 - z_\eta^2)[(u_{z_\alpha})_{xx} + (v_{z_\alpha})_{xy})] + (z_\alpha - z_\eta)[(hu_{z_\alpha})_{xx} + (hv_{z_\alpha})_{xy}] \\ v^\eta &= v_{z_\alpha}\frac{1}{2}(z_\alpha^2 - z_\eta^2)[(u_{z_\alpha})_{xy} + (v_{z_\alpha})_{yy})] + (z_\alpha - z_\eta)[(hu_{z_\alpha})_{xy} + (hv_{z_\alpha})_{yy}] \end{aligned} \tag{104}$$

Where u_{z_α} is the velocity at $z = z_\alpha$ and u_η is at $z = \eta$. The Froude number can then be calculated as:

$$Fr = \sqrt{\frac{u^{\eta^2} + v^{\eta^2}}{gh}} \tag{105}$$

Which measures how fast the particles in the waves moves in comparison to the waves celerity. If $Fr > 1$ the flow is supercritical and breaking occurs as the particles overtake the wave front, but [Varing et al., 2021] proved that at for $Fr > 0.85$ breaking will inevitable occur. A number in between these two values thus seem to represent the onset of breaking correctly. While the best value is not proven, BOSZ operates with $Fr = 1$ as the trigger value.

Lastly the third criterion is the ratio of the local wave height and water depth. But this is hard to calculate in a model as the crest and through corresponding to a single wave is unknown unless a tracking algorithm is implemented as well. Therefor the linear threshold of $a/h > 0.78$ is generally not the same as $2\eta/h > 0.78$ as the waves profile might not be symmetric about the mean water height. Nevertheless [Roeber, 2021]) proposes that a compensation of $\eta/h > 0.6$ might account for the disparity.

A comparison of these three different methods of identifying breaking is given in Ch. (3.2).

2.2.2 Turbulent kinetic energy

Now to answer the question regarding how to deal with the problem of discontinuous wavefronts, one potential solution is to add a diffusive term which prevents the creation of a sharp front. When this is prevented, the problem of the source term growing arbitrary large is also prevented. One such diffusive term is an eddy viscosity model coming from the work of [Zelt, 1991] and [Kennedy et al., 2000]. The term they proposed is added to the momentum equation and looks like:

$$\mathbf{R}_b = \begin{vmatrix} 0 \\ [\nu_t H u_x^\alpha]_x + [\frac{1}{2}\nu_t H(u_y^\alpha + v_x^\alpha)]_x \\ [\nu_t H v_y^\alpha]_y + [\frac{1}{2}\nu_t H(u_y^\alpha + v_x^\alpha)]_y \end{vmatrix} \tag{106}$$

This diffusion term involves the time-varying eddy-viscosity ν_t which determine the strength of the diffusion. This term is again connected to the Turbulent Kinetic Energy (TKE) k through the relation defined by [Pope and Pope, 2000] as:

$$\nu_t = \sqrt{k} H \tag{107}$$

Now the governing equation of TKE is given by Pope as:

$$k_t = -A - E + P + D \tag{108}$$

Where the right-hand side variables denote advection, elimination, production, and diffusion of TKE respectively.

All of these terms are active and calculated every time loop in every cell, except the production term. This means that as waves travel through the domain, do not get influenced by the TKE until they activate the production term. They then continue to lose energy to diffusion even after the production term is deactivated until enough energy is diffused that the TKE term is negligible.

The production term is assumed to be proportional to the vertical gradient of the horizontal water particle velocity at the crest and is activated whenever the local Froude number exceeds 1, as shown in the previous chapter [Nwogu, 1996]. The term which Nwogu developed looks like:

$$P = BH^2\sqrt{(u_z|_\eta)^2 + (v_z|_\eta)^2} \cdot [(u_x + v_y)(u_x + v_y) + (u_y + v_x)] \tag{109}$$

Where $B = 0, 1$ depending upon the trigger defined earlier. The vertical gradients of the horizontal velocities are found from the truncated Taylor series in combination with the irrotationally condition such that :

$$\begin{aligned} u_z|_\eta &= -\eta[u_{xx} + v_{xy}] - [(hu)_{xx} + (hv)_{xy}] \\ v_z|_\eta &= -\eta[u_{xy} + v_{yy}] - [(hu)_{xy} + (hv)_{yy}] \end{aligned} \tag{110}$$

Further [Nwogu, 1996] calculated the advection term, elimination term, and diffusion term as:

$$A = uk_x + vk_y \tag{111}$$

$$E = \frac{k^{3/2}}{H} \tag{112}$$

$$D = \nu(k_{xx} + k_{yy}) \tag{113}$$

Where $\nu = 0.001[m^2/s]$ is the kinematic viscosity of water, and constant terms have been changed to agree with information available in BOSZ [Roeber, 2021].

Now all derivatives in these terms are solved using finite differences in each time loop for all cells. These equations, and in particular the governing equation of TKE, state a fourth governing

equation for our model. The time dependency of k_t is solved for by the second order Runge-Kutta method just like the other governing equations, where the RHS are determined by the equations above.

This yields a systematic way of moving along diffusive terms and remove energy at locations moving along with the waves, which simulates white water. So this makes a method to deal with wave breaking which always acts across the domain by varying degrees.

3 Test cases

In this chapter I simulate three test cases to verify that the BOSZ model can simulate the earlier mentioned fluid processes in Ch. (1.3) to a satisfactory degree.

3.1 Bartest

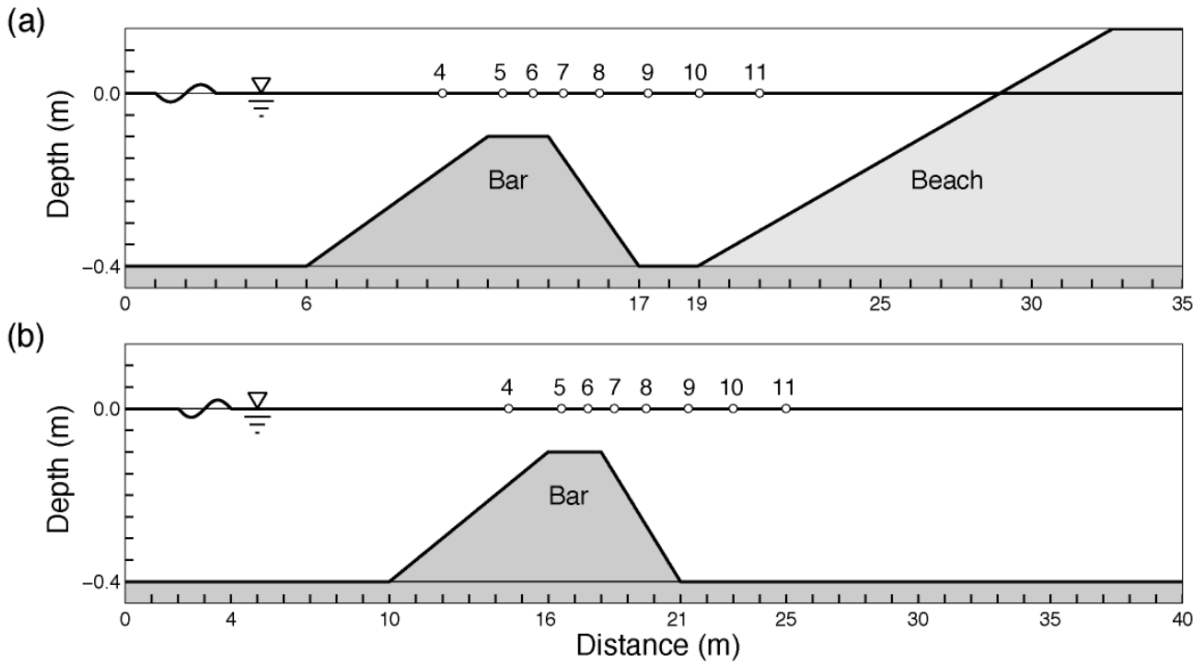

Figure 4: Sketch of the bartest. (a) The laboratory setup. (b) The numerical set up. Circles and numbers denote gauges.

[Beji and Battjes, 1993] created a laboratory experiment in which they investigated propagation of waves over a submerged bar. The above figure depicts a 37.7 meter long, 0.8 meter wide, and 0.75 meter high flume. Submerged in 0.4 meter of water is a 0.3-meter-high bar with a 1:20 sloped front side, 2 meter wide top, and 1:10 sloped backside. At the end of the flume is a gravel beach which acts as a wave absorber.

This setup is replicated in our model, except I add some additional 4 meters in which our numerical wavemaker replicates the wave setup. In addition, I neglect the beach at the right hand side of our setup in accordance with earlier research. [Stelling and Zijlema, 2003], [Roeber, 2021]. The lack of a beach on the right-hand side should not affect gauges 4-10, but it might influence gauge 11.

When waves travel up the bar they shoal and the low value of kh makes the wave non-linearly self-interact to create higher harmonics (see Ch. 1.3.1 and 1.3.3). These are originally bound together with the primary wave since their phase speed eq. (19) are equal. But when they reach the end of the bar kh rapidly increase and the phase speed differs between the harmonics, resulting in "freed" higher harmonics. Many Boussinesq-type or non-hydrostatic models do not fully resolve these higher harmonics due to low-order approximations of the non-linearity and dispersion of the governing equations. Sandbars are common in coastal waters and are therefore important to consider in near-shore experiments.

We are focusing on [Beji and Battjes, 1993] experiment with sinusoid waves with 2.05 cm amplitude and 2.02 s period.

3.1.1 Numerical set-up

I input the bathymetry as indicated in the above figure with a grid size of 1.25 cm. At the start of our numerical scheme, I have a 125 cell wide sponge layer to position the wavemaker as close to the laboratory experiment as possible. The data at each of the gauges are recorded every 0.02s. Further I have introduced a uniform manning friction of 0.01 to represent bottom friction Ch. (1.3.4). And lastly, I input the sinusoidal waves as described above.

3.1.2 Results

These simulations line up relatively well with the experiment. At Gauge 4 I can see that the model has made the wave shoal to the right proportions, with perhaps a small phase shift. Through 5-7 I can see the higher harmonics being created, but bound to the solution, until they in 8-11 become free to propagate. Gauge 8-10 seem to fit particularly well, but gauge 11 seem miss some details.

This might be because of the different topography in our model and the experiment, or it might be because of the errors in dispersion in the BOSZ model. Gauge 11 is in the original experiment placed above the beach. It is therefore not surprising that our model does not accurately predict the wave conditions at this location, since it does not take shoaling into account for this gauge. Further the error in dispersion for our governing equations might be starting to come into effect at this location, further exaggerating the errors as seen in Ch. (1.4.4).

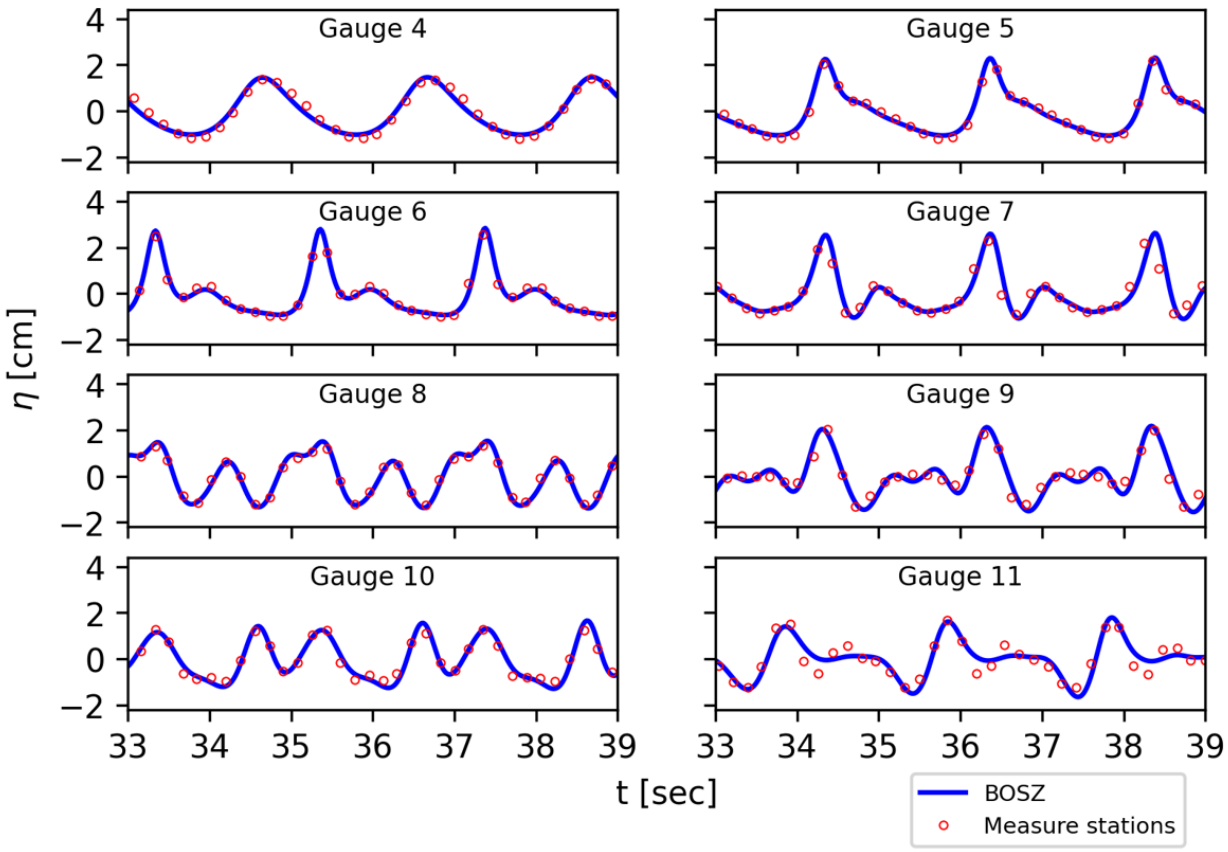

Figure 5: Comparison of BOSZ and experimental results of a wave propagating over a submerged bar. Red circles indicate recorded experimental data of Beiji and Battjes, and blue lines the numerical results from the BOSZ model.

3.2 Suzuki test

3.2.1 Experimental set-up

In 2017 Tomohiro Suzuki conducted a test and described it in [Suzuki et al., 2017]. The layout represents a 1D channel where the kh value is about 1.5 and is therefore not particularly dispersive. The structure consists of a 1:35 sloped smooth impermeable concrete dike, a sharp 1:2 sea wall, and a 1:100 promenade until the end domain. In his experiments Suzuki measured the overtopping discharge at the end of the channel.

The model is in total 70m long, 1.5m high, and 4m wide. It is further placed 12 gauges at the locations indicated in the figure. The wave paddle created a spectrum of waves which would be fully generated by the SWASH boundary, where he placed 3 gauges to that the spectrum where gully generated.

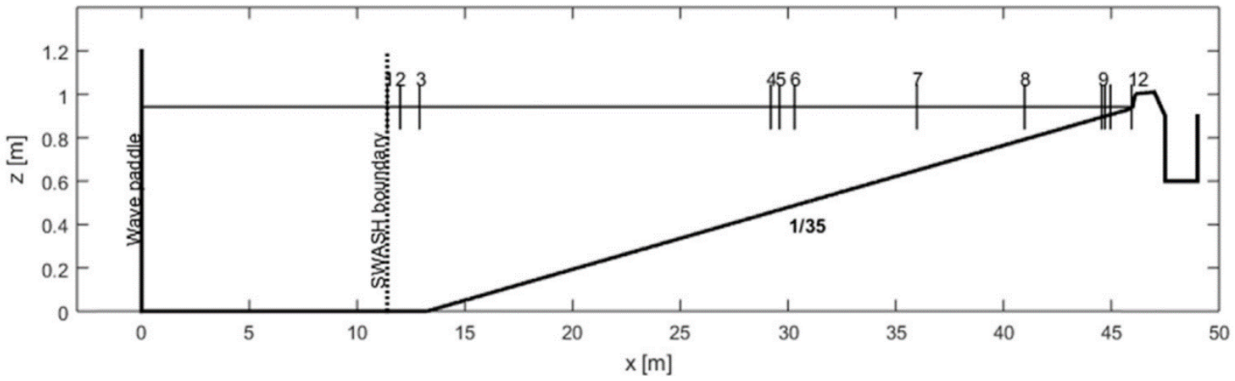

(a)

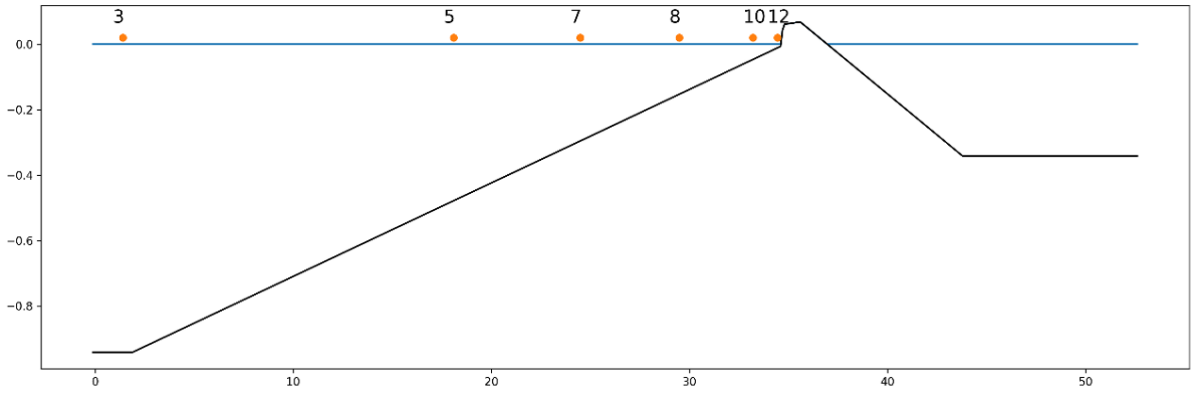

(b)

Figure 6: a) Experimental layout of Suzukis test. The BOSZ model's bathymetry starts at the SWASH boundary. Graphics is taken from (Suzuki, et al., 2017), b) Computational domain and gauge location used in the BOSZ model

3.2.2 Hydraulic processes and model input

This experimental setup is suited to test for shoaling, wave-wave interactions, and transfer and dissipation of energy through breaking. The waves are fed through the left boundary as a time series supplied by Suzuki, and travel freely through the domain until any wave overtopping are captured at the right by a sponge layer. The computation time is 400 seconds. As the waves travel right, they shoal, steepen, and eventually breaks. For this I need some criteria to detect wave breaking since the model can only model 1-dimensional flow. The model comes with three possible criteria: testing the Froude number, the momentum gradient, or the ratio of wave height and water depth. As seen below, all of these give satisfactory results but with minor differences depending upon the method of wave detection.

3.2.3 Results

The BOSZ model seem to handle the generation of infra-gravity waves and the diffusion of energy of the spectrum particularly well, regardless of the method of detection of breaking. There are minor differences of power density between the methods, but big picture they are all working out fine. Near the seawall the methods underestimate the diffusive properties of higher frequency waves, and as a result there appears higher peaks at around 0.3 Hz.

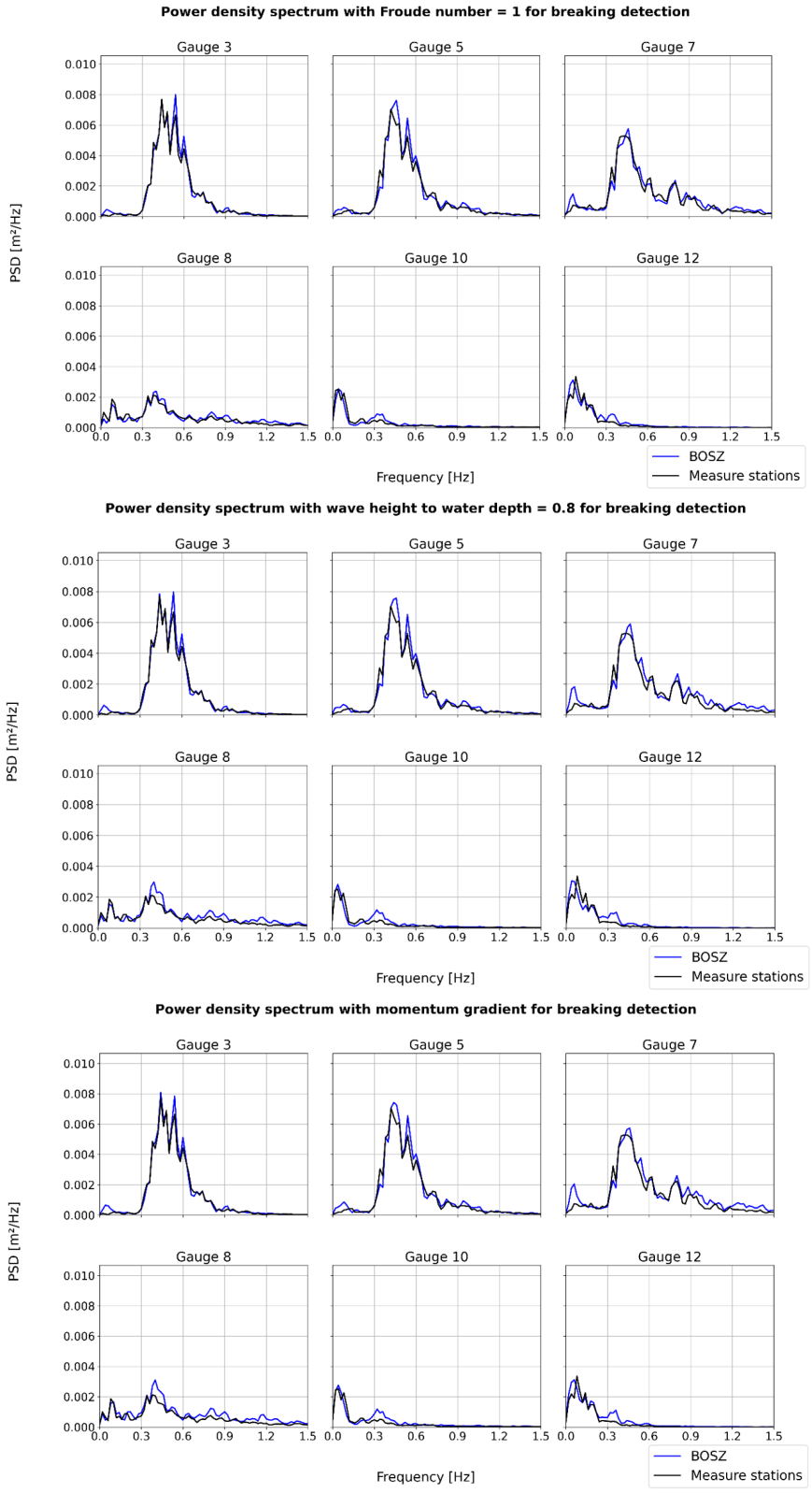

Figure 7: Power spectral density of BOSZ at the six indicated wave gauges. Case computed with Froude number, water height to depth ratio, and momentum gradient for detection of wave breaking on top, middle and bottom respectively.

3.3 NTHMP 2015 BM5

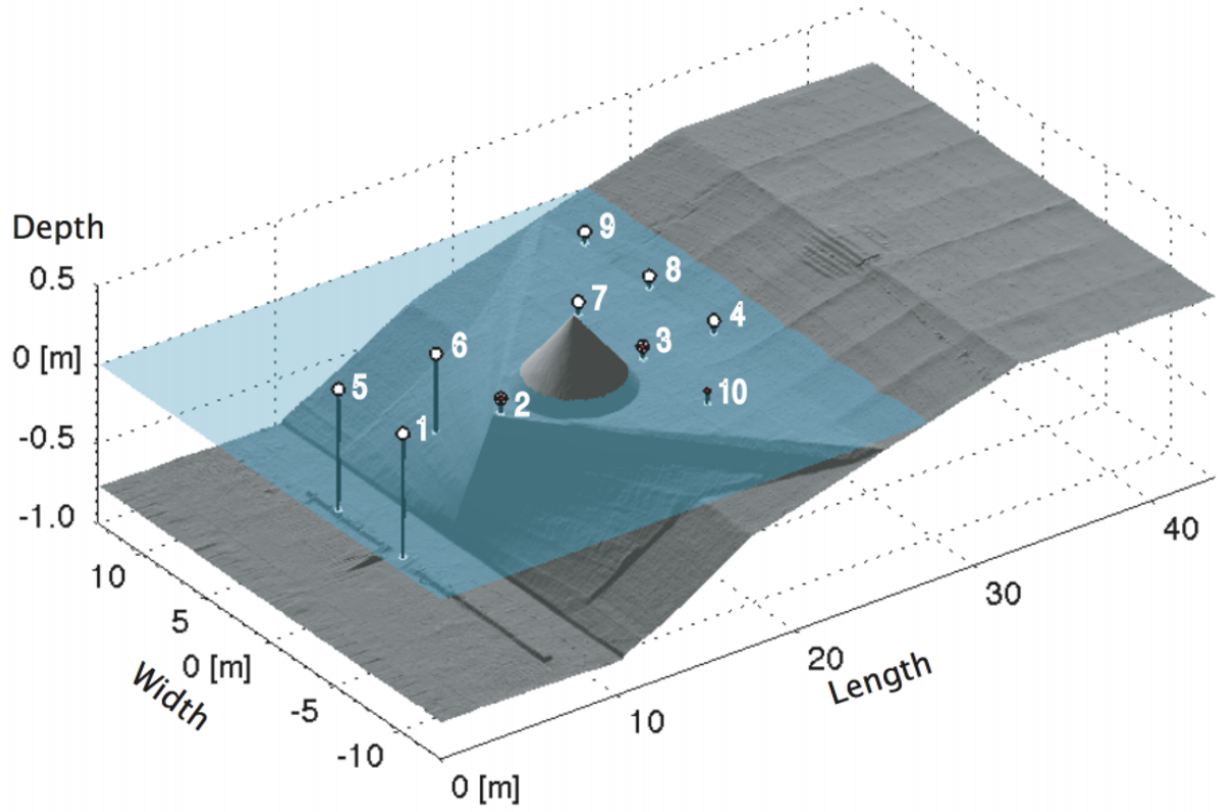

Figure 8: Bathymetry and gauge locations for Swinglers experiment and the numerical set up

3.3.1 Set-up

In 2015 the National Tsunami Hazard Mitigation Program (NTHMP) benchmarking competition chose the experiments of [Swigler, 2010] as a test for various models. This experiment was conducted in a basin at Oregon State University and was 48.8m long, 26.5m wide, and 2.1m deep. The water level was kept at a maximum depth of 0.78m.

At the start of the basin was a wavemaker located, before on the other side a complex shallow water bathymetry constructed of concrete was located. This was made up of a 1:16 plane beach, out of which a triangular shelf was built with a depth of 5cm. The apex of the triangle was located at X = 12.6m, Y = 0, and was connected down from the sides of the triangle. This connection was steepest at the apex with a slope of 1:3.5. Further, on top of the triangle is a cone, reaching up and out of the water. The top has a shallow slope of just 1:30 so ensure that the water falls back into

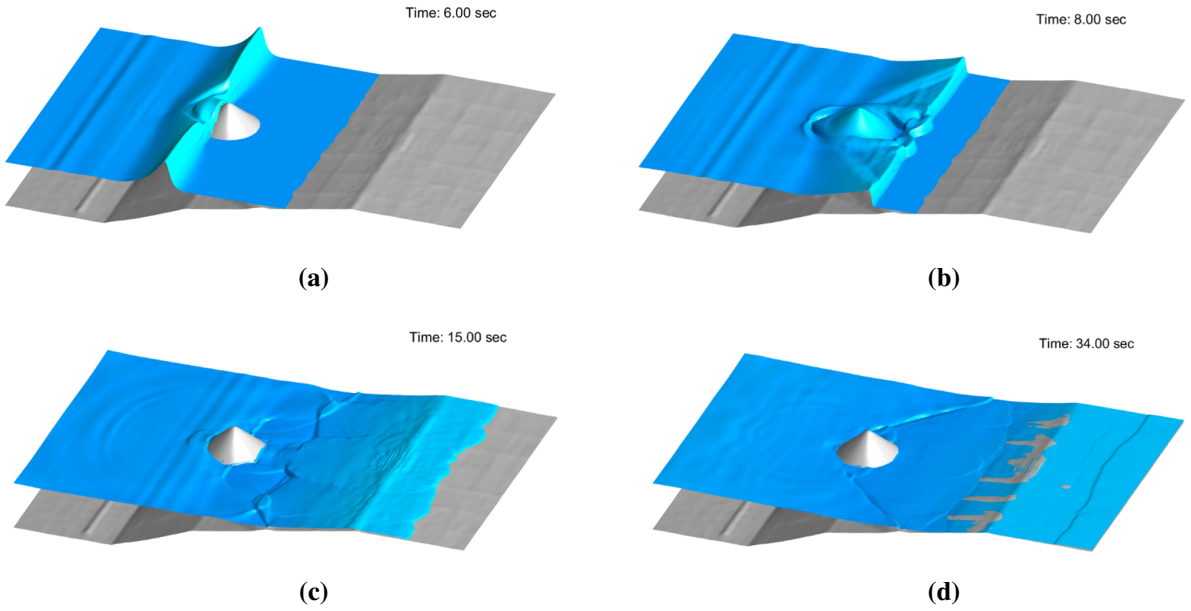

Figure 9: a) Wave field at 6s. The wave front has steepened and begun breaking over the cone. b) Wave field 8s into the simulation and there's vortex formation around the cone. The breaking wave front is simulated as a discontinuity. c) Wave field after 15s. There is run up onto the dry bed. Water have begun puring down again. d) Wave field after 34s. The wave fields continue to move back and forth, but with less amplitude. The plotting script is due to V. Roeber.

the tank after each experiment.

Into the basin it was generated a single solitary wave with height 0.39m to create a single strong breaker.

3.3.2 Model input and hydraulic processes

The BOSZ model was set up with $\Delta x, \Delta y = 0.1m$ and Courant-Friedrich-Lewy number of Cr=0.5, lastly a Manning coefficient of $n = 0.015m/s^2$ was chosen to best reflect the bottom friction of the concrete. The bathymetry was scanned by Lidar at 10cm increments and supplied to me by Volker Roeber. Lastly the wave input is a solitary wave generated out of bounds, which are moved into the domain before the domain is closed behind it.

This experiment is good to test our previous results with another dimension added, and to introduce new effects such as refraction and diffraction. Firstly, when the wave hits the slope, we get a quick shoaling which also steepen the wave front. This evolves into various forms of breaking, of which Swingler noted that at the reef edge the wave is plunging and at the crest its spilling. Further the triangular hill introduces a change of angle of steepening, and diffraction

begins to matter. In addition, behind the cone there's less a lower free surface, and refraction must also be modelled. Lastly, there's reflection to be accounted for at the slope, cone, and all walls of the domain.

In addition, there's also the numerical challenges of the steep slope of 1:3.5 at the apex of the triangular hill, the non-linear behaviour of the soliton wave, and the numerous breaking and moving waves.

3.3.3 Results at gauges

The comparison of the simulation and experiments are given below. The close resemblence of the two plots validate BOSZ ability to simulate multiple wave processes as described in Ch. (1.3) and (3.3.2). It also importantly shows that the model can sufficiently model various breaking in multiple directions at the same time.

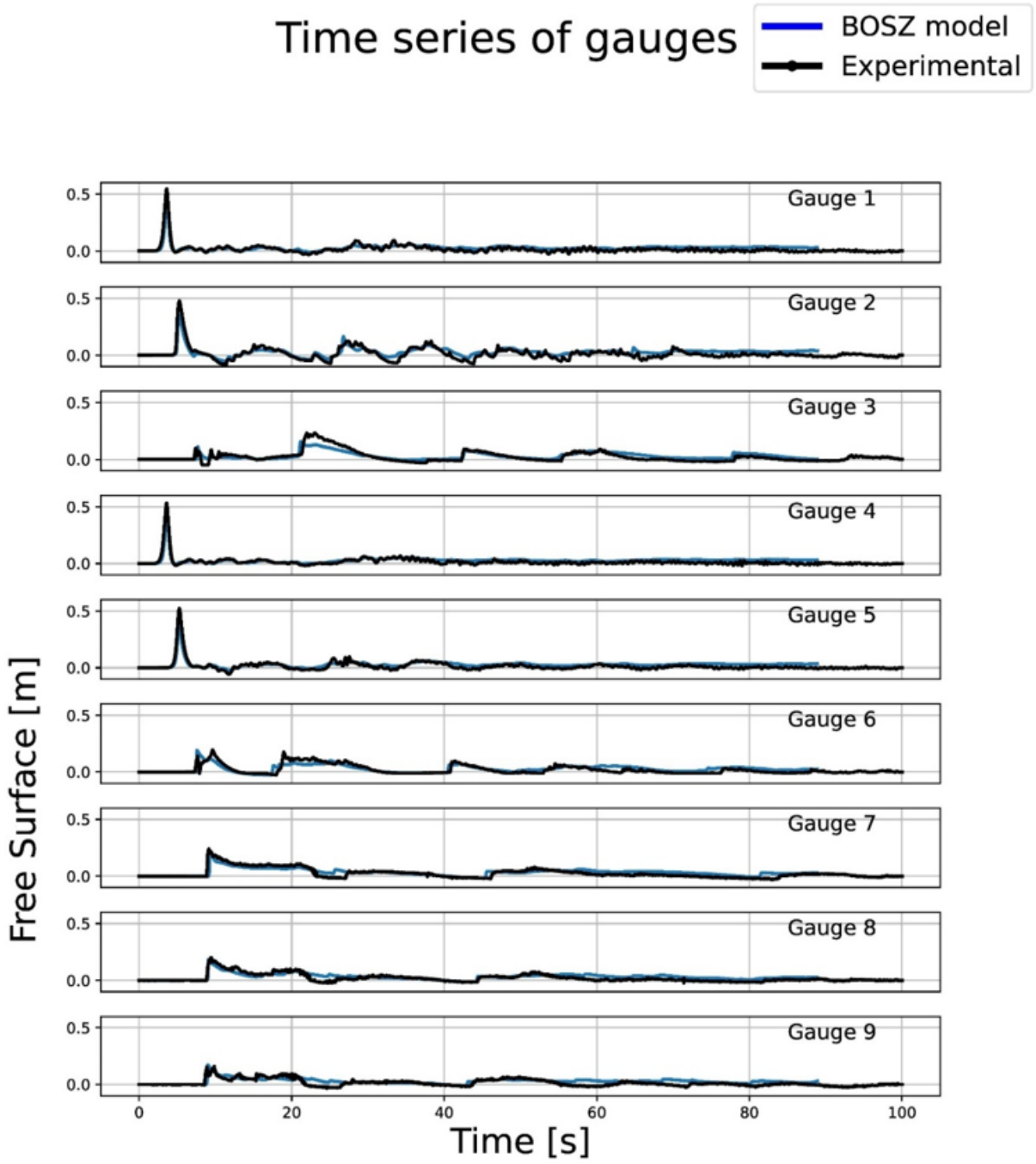

Figure 10: Free surface elevation at the gauges. The blue line denotes the computed results, and the black the experimental.

4 Infra-gravity particle transport

4.1 First order theory

In Ch. (1.1) it was found that the velocity of fluid particles under the influence of linear gravity waves was:

$$u_x = \frac{\omega a\, cosh[k(H+z)]}{sinh(Hd)} cos(kx - \omega t) \tag{114}$$

$$u_z = \frac{\omega a\, sinh[k(d+z)]}{sinh(kd)} sin(kx - \omega t) \tag{115}$$

The linear path lines of the fluid particles are then given as:

$$\frac{d\xi}{dt} = u_x(x,z,t) = \omega A \frac{cosh(k(H+z))}{sinh(kH)} cos(kx - \omega t) \tag{116}$$

Assuming that the particles position x stay close to the centre x_0 is small we can linerize the problem by saying that the path is $x = x_0 + \xi(t)$. The assumption of small movement is believed to be true with the small amplitude assumption of the waves, which cause the velocity above to be small as well. After linearising, the differential equation becomes:

$$\frac{d\xi}{dt} = \omega A \frac{cosh(k(H+z_0))}{sinh(kH)} cos(kx_0 - \omega t) \tag{117}$$

Which can be readily solved as:

$$\xi = x_0 - A \frac{cosh(k(H+z_0))}{sinh(kH)} sin(kx_0 - \omega t) \tag{118}$$

So the amplitude of the horizontal movement is $L(A,k,z) = A\frac{cosh(k(H+z_0))}{sinh(kH)}$. Now by choosing a value for the amplitude of the wave we can find the associated value for any particular wavenumber, and through the dispersion relation $\omega^2 = gktanh(kH)$ the corresponding wave frequency.

In Fig. (11) we can see the size of horizontal movement for two different combinations of these two variables. It is clear that infra-gravity waves has a much larger influence on the horizontal movement than ordinary gravity waves. Even when looking at a JONSWAP spectrum, and adding a small and arbitrary infra-gravity component the dominant force of movement is the infra-gravity waves. This is true for any value of the ocean depth, but the movement itself of the particles become smaller for larger depths.

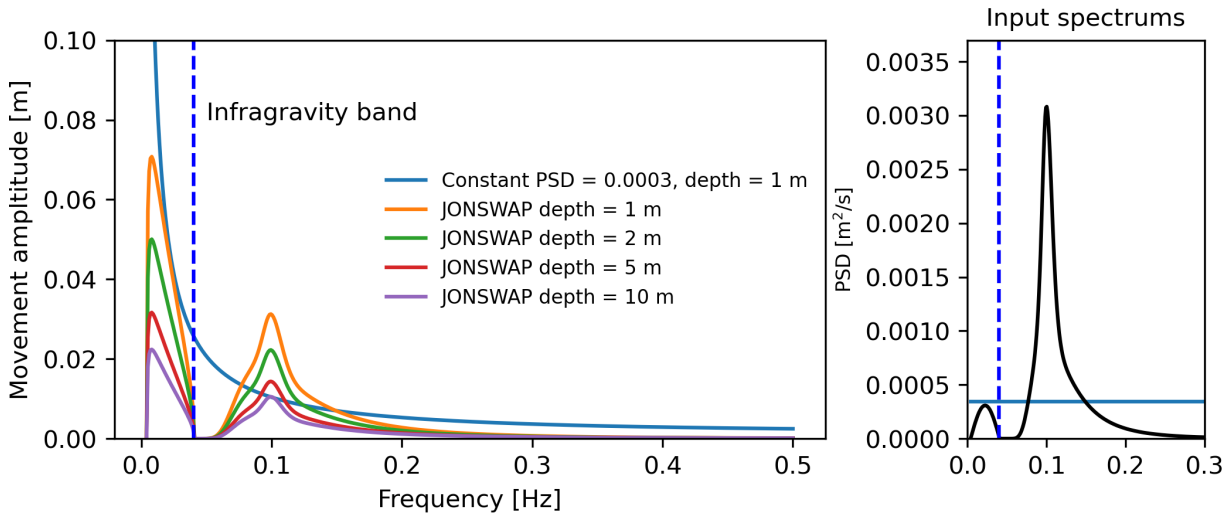

Figure 11: Analytical solutions of the movement of the particle in a surface wave of a single frequency. The blue line shows the movement associated with different wave components with equal amplitude. The remaining lines show the effect for varying depths when the amplitude comes from a Jonswap spectrum with $H_s = 0.10m$ and $T_m = 10s$, with an added infra-gravity component with 10% of the associated energy. On the right is a representation of the power spectrums of the amplitudes used.

4.2 Numerical solutions

4.2.1 Linear model

Now, assuming that the small amplitude assumption means that we can add every wave component in a superposition, such that:

$$\eta_i(x,t) = A_i cos(k_i x - \omega t) \tag{119}$$

$$u_x(x,z,t) = \sum_i u_{x_i} = \sum_i \omega_i A_i \frac{cosh(k_i(H+\eta_i))}{sinh(k_i H)} cos(k_i x - \omega_i t) \tag{120}$$

As seen in the previous chapter, this of course means that the movement of the fluid particle can be modelled as:

$$\frac{dx}{dt} = u_x(x,z,t) \quad \frac{dz}{dt} = u_z(x,z,t) \tag{121}$$

Now instead of assuming that the velocity of the particle is close to that near the original center, we look at a particle that can move freely around. This means that we now also will include the Stokes drift induced from the linear waves as described in Ch. (1.2.2). See Fig.(12) for explanation

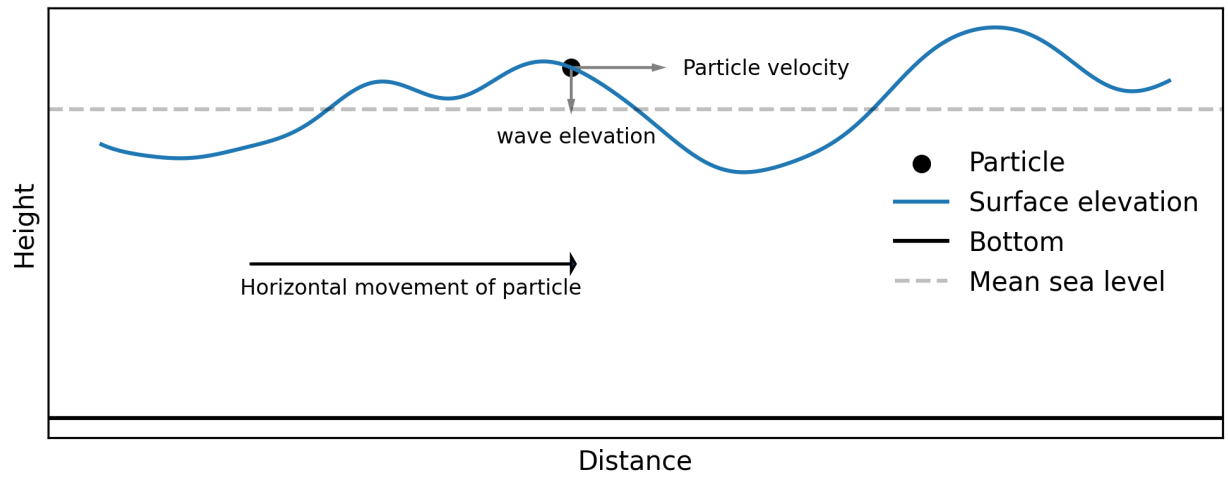

Figure 12: The ocean surface is simulated for some constant depth. A drifter located at the surface has an instantaneous velocity and elevation and are free to move in the horizontal direction. After some time it has had a horizontal movement away from its starting position.

of the variables and Fig.(13) for the case with 1 wave component.

I estimate the above equation with 500 wave components drawn linearly between frequencies of $0.004Hz$ and $0.5Hz$. The amplitudes and wavenumbers are chosen from the dispersion relation and modified JONSWAP spectrum seen in the last chapter.

Following the particle for 1800s with a time discretization of 0.25s, using RK4 to evolve time, and removing the linear stokes drift, we get the results from Fig. (14). Notice here that the position of the tracer is dominated by the components in the infra-gravity spectrum with an even more drastic difference than the analytical case, while the amplitudes and velocity is reminiscent of the input spectrum.

4.2.2 BOSZ movement

Now we instead want to utilize the phase-resolving nearshore surface model BOSZ to model a full sea state where our particles are tracked by solving eq.(116) for each time step. This will simulate that when the wave field evolves while approaching the shore, the influence on the movement on the particles are also changed.

For this test we will input a JONSWAP spectrum as in the earlier tests, but without the infra-gravity component (see Fig.(15) upper right panel). This spectrum will be created inside the domain by the model, and every infra-gravity components in the spectrum will be created through the nearshore wave evolution which BOSZ model.

To see that BOSZ can model this IG-generation a simulation of BOSZ is run for 3 hours with

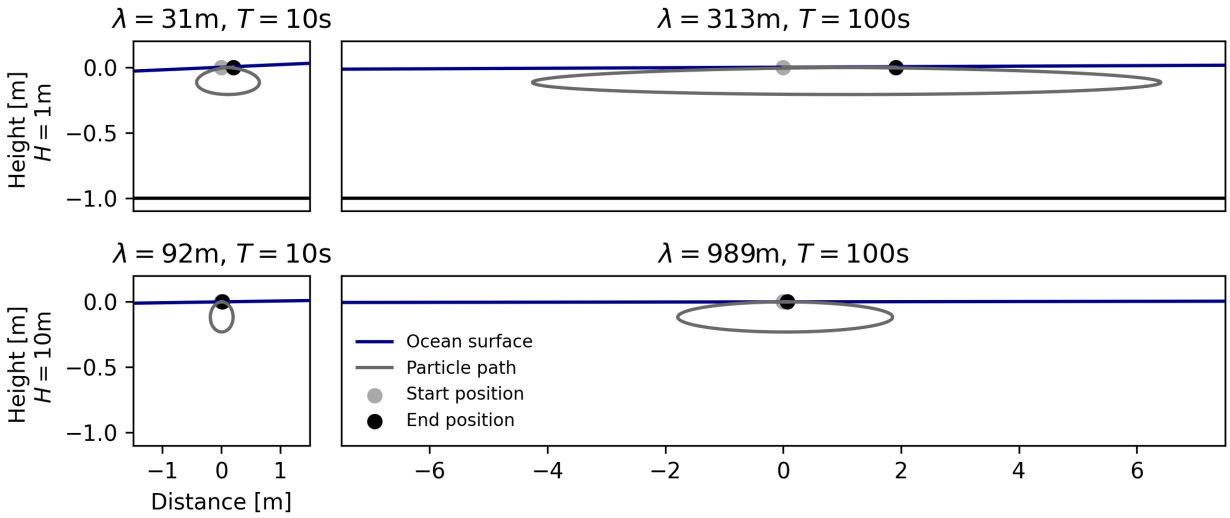

Figure 13: The pathline for one particle drawn through 1 period for a single wave component found by solving eq. (116) with RK4. Left: a 10 second wave with amplitude 10cm for depth $= 1$m and $10m$. Right: a 100s wave with the same amplitude and depths. As seen predicted for the first order approximation, the IG waves have a much larger impact on the particles horizontal movement.

a 1 hour setup time for 3 different bathymetries. Every second the wave elevation at a numerical gauge is recorded, before the power spectral density is calculated. In figure (15) one can see the bathymetries and corresponding power spectral densities (PSD). In the flat beach case both ends of the domain are padded with a sponge layer, such that no reflection takes place. Thus IG-wave components which are visible in the spectrum must thus be bound IG-waves as described in Ch. (1.2.1). For the other two bathymetries, a plane beach and a trilinear beach which becomes more gentle closer to the surface, the IG-band is more pronounced by a factor of 2-4. This must be due to free IG-waves generated when the waves break in the surf zone as described in Ch. (1.3.5).

To see the influence of these IG-waves on particle transport we simulate an applied case with a more complex barred beach. The bathymetry of which can be seen in the top panel of Figure (16), with the locations of three buoys and corresponding drifters are marked. It is a 1-dimensional domain with spatial resolution of $DX = 1$m, composed of multiple sine waves made to resemble a domain outside of Hawaii [Roeber and Cheung, 2012]. This is to have a simple bathymethry which is somewhat realistic which can showcase the effect of the IG-wave transport.

The model in run for 1800 seconds before the drifters are released and begin moving such that the wave field can become saturated before simulating. The model is then run for another $T = 1800$s, such that the fundamental frequency we can detect in our time series analysis is $f_0 = \frac{1}{T} \approx 0.0005$s, more than enough to detect the entire IG-spectrum. Further we sample the

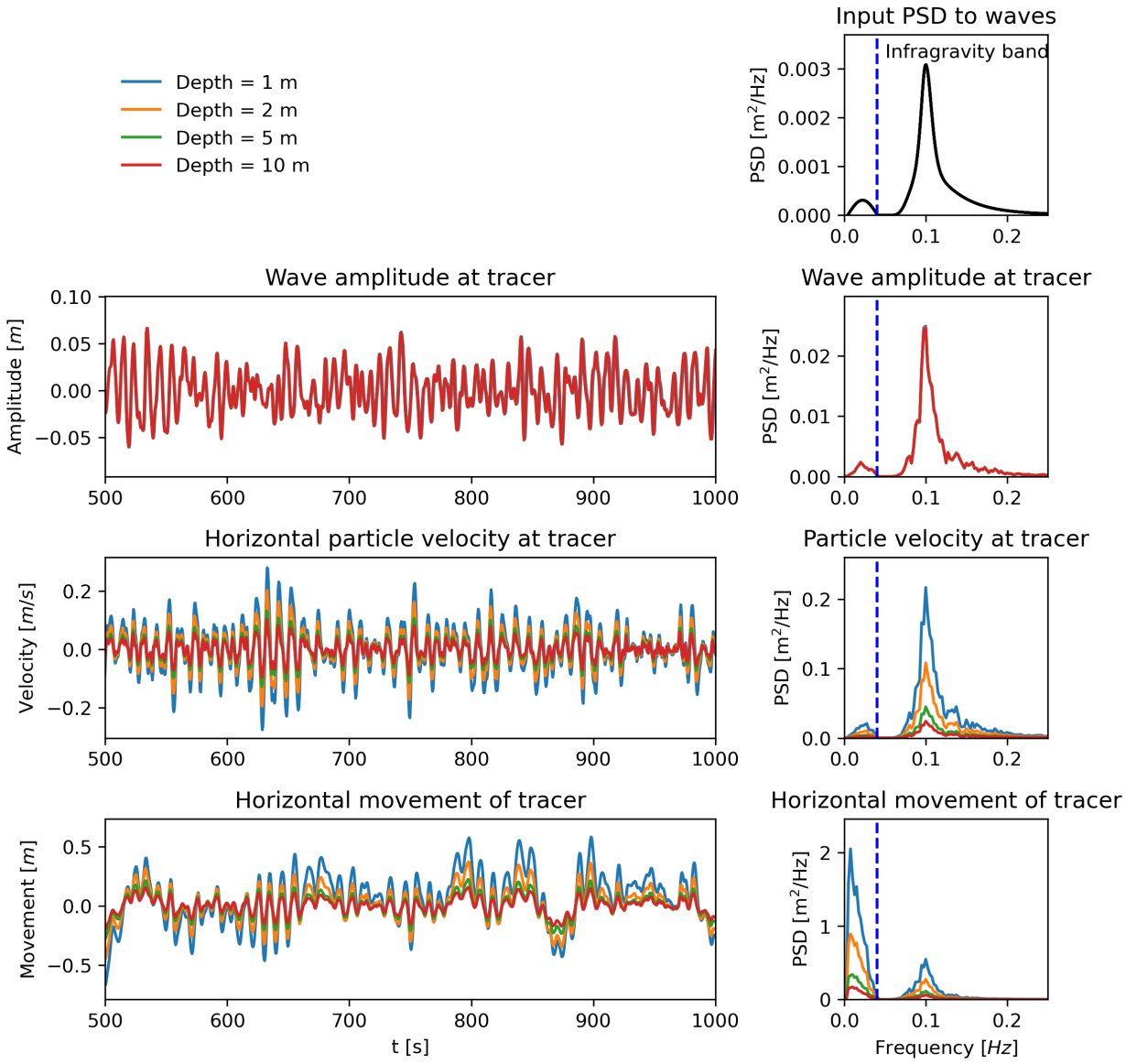

Figure 14: Experimental results from following a fluid particle moved by a superpostion of waves. Top: Amplitudes of waves encountered by the particle. Middle: Velocity experienced by the particle. Bot: Position of particle over time with the Stokes drift removed. Left: Time series of values. Right: Power spectral density of the time series. Color indicate simulation depth. Blue 1m, orange 2m, green 5m, red 10m.

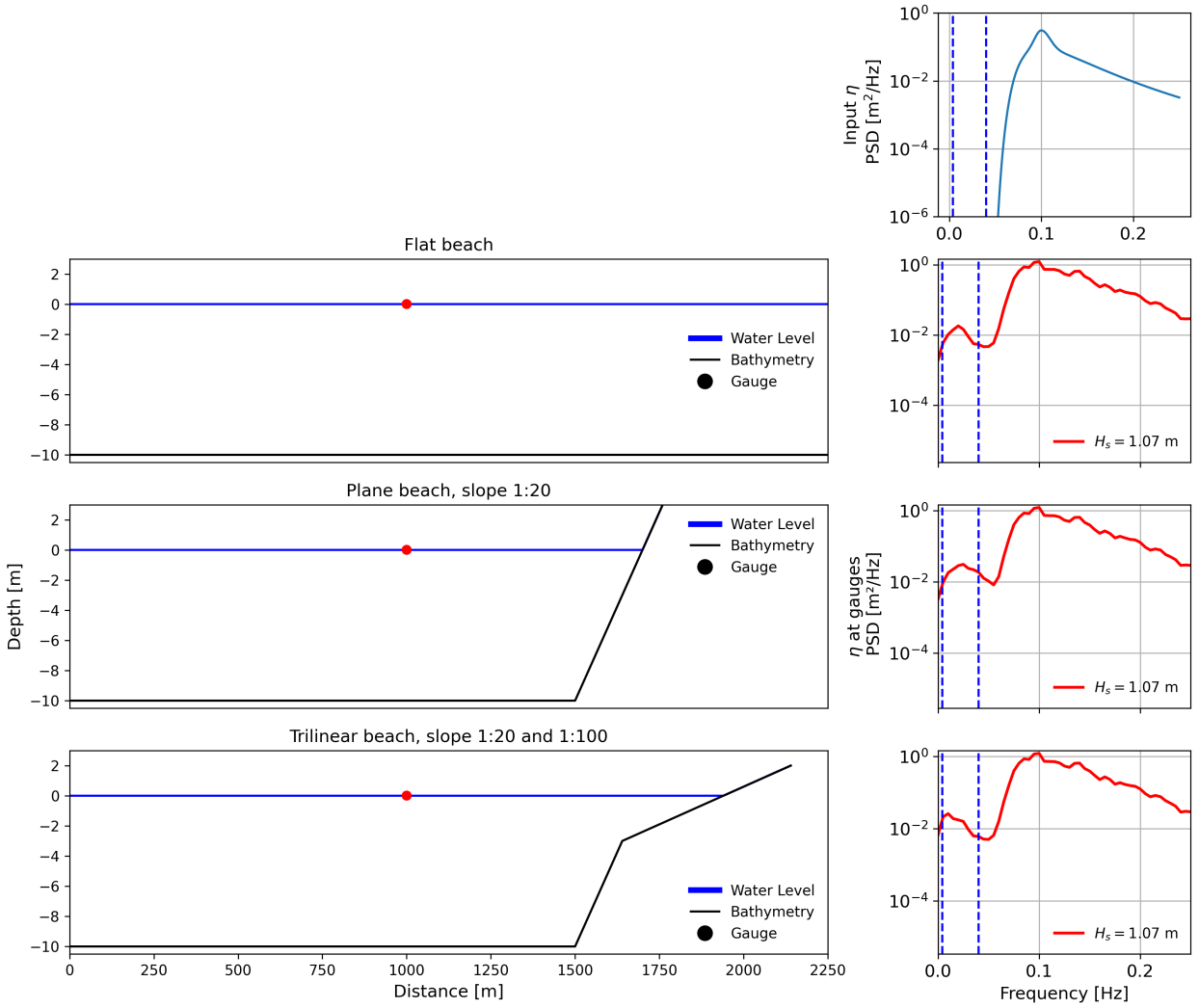

Figure 15: Comparison of infra-gravity wave generation inside BOSZ. Upper right: the input JONSWAP spectrum to the model with $H_s = 1$m and $T_p = 10$s. Notice the lack of IG wave components in the input. Second row: Here a flat beach is simulated, and bound IG waves are generated as anticipated by [Longuet-Higgins and Stewart, 1962]. Third and fourth row: with the inclusion of a beach where waves can break the IG-band is increased in importance. This is due to free IG waves being generated by the breakpoint [Symonds et al., 1982].

position every $\Delta t = 1$s so our Nyquist frequency is $f_{max} = 0.5$s, this is enough that our spectrum can have nonlinear wave-wave interaction and release superharmonics when they shoal.

Now for the particles we simulate them as fluid particles such that their movement are determined by:

$$\frac{d\xi}{dt} = u|_{z_\alpha} \tag{122}$$

Where z_α is the reference depth at which the velocity variable of the velocity fields are evaluated in the BOSZ model. This means that we now model fluid particles located at depth $z = z_\alpha = -0.531H$, examples of which are plotted in Fig. (16). The vertical distribution of horizontal velocity is in general non-constant in the ocean, as seen in eq. (114). Now by decreasing the value of z_0 in (118) when $H >> 0$ the amplitude of motion decrease as well. Since this effect is equal for all wave frequencies according to linear theory, this will not effect the results when comparing the Power Spectrum Densities.

Running the simulations and performing a time series analysis yields the spectrums seen in Fig. (16) in the middle and lower panels. In the middle panels are the PSD of the buoy wave elevation record plotted, and the lower panels show the Fourier transform of the detrended position of the fluid particles. The leftmost plot shows that JONSWAP spectrum has been generated by the wavemaker, but with some extra energy associated by frequency at $0.2Hz$. This seem to the authors to be reflected waves that through triad wave-wave interaction has created wave components of about twice the frequency of the original JONSWAP peak. Looking at the panel below, it is seen that offshore the movement of the particles are dominated by the peak of the JONSWAP spectrum.

Further looking at the middle panel, here the waves have travelled through a slope which change the water depth from 10m to 2.5m. Looking at the PSD of the wave elevation it is obvious that the peak has been greatly reduced by the bathymetry driven breaking which occurred while the depth decreased. Looking between the two blue stippled lines it is seen that this breaking has transferred some the energy to infra-gravity wave components. Interestingly this small wave component has caused the movement of the particle simulated at this depth to mainly be moving at IG-frequency.

Further, looking at rightmost plots seems to indicate that so close to shore at such small depths almost all non-IG wave components have dissipated. While the incoming waves travelled through a bar with minimum depth of 0.5m the energy of the waves transferred to the IG-band and now the predominating frequency for the wave elevation is infra-gravity. Also looking at the drifters, the increased energy associated with IG-waves now yield a much larger movement than earlier.

All in all this seem to indicate that near-shore the particles in the water are mainly determined by the IG components coming from breaking, rather than the higher frequencies wave components. Also interesting is the fact that even though the significant wave-height and total energy in the wave

field decrease towards shore, $H_s = 1.12, 0.65, 0.14$m at $x = 1000, 1800, 2400$m respectively, the movement of the particles increase.

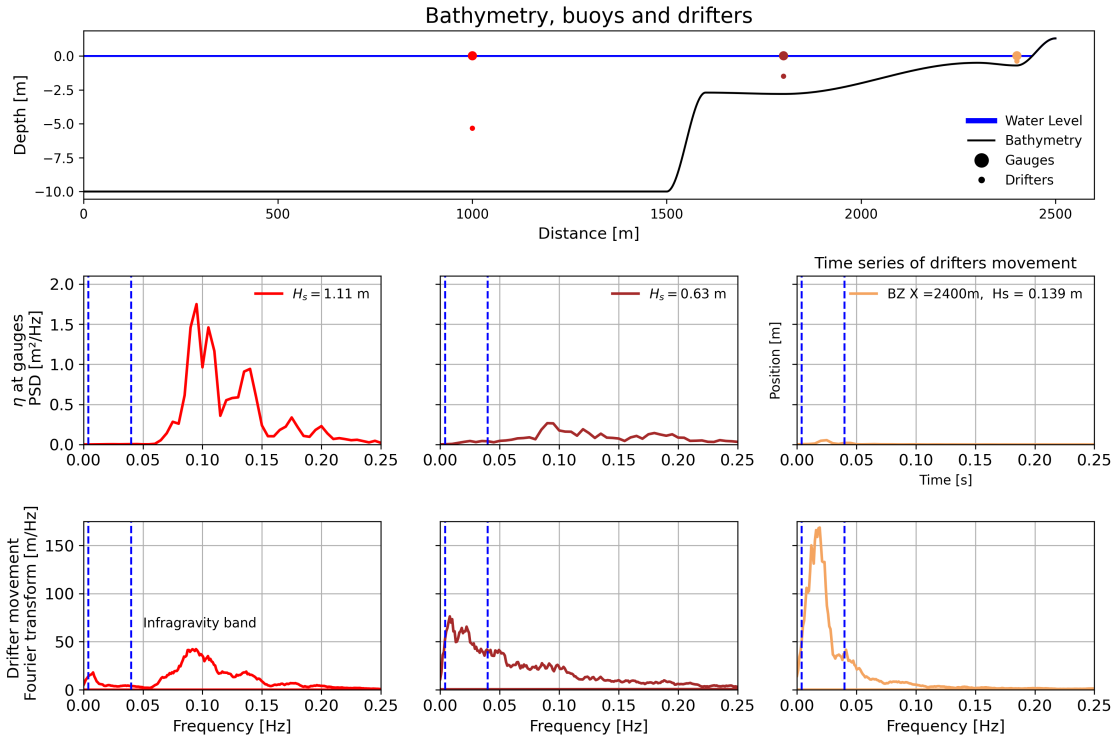

Figure 16: Experimental results from following fluid particles. Top: Bathymetry and locations. Middle: Power spectral densities of the wave elevation at the gauges. The colors correspond to the locations in the top plot. Bot: Power spectral densities of the movement of the particles after Stokes drift has been removed.

4.3 Discussion

Through this chapter it is seen that wave components from the infra-gravity spectrum have a much larger influence on the movements of particles nearshore. In Ch. (4.1) this is seen to be the results of lower frequency waves causing the particles to move in larger ellipses, a fact which we see remains true even when incorperating higher order effects such as Stokes drift in Ch. (4.2.1). We saw then that IG-components of just 10% of the energy of the peak causes the movements to be mainly caused by IG periods.

To represent a real case scenario we used the BOSZ model due to Volker Roeber which can generate the IG waves inside the domain without need to arbitrarily add them (Fig. 15). This experiment showed that IG-waves naturally arise nearshore, both due to the radiation stresses and depth-induced breaking. We thus saw in Ch. 4.2.2 that nearshore the particles are influenced by

IG.components, while in the surf zone they are mainly controlled by them.

It is therefor crucial to include IG-effects to any models or experiments looking at transport of particles in the ocean. In the next chapter we do this by simulating oranges in BOSZ, which we have shown generate these waves numerically.

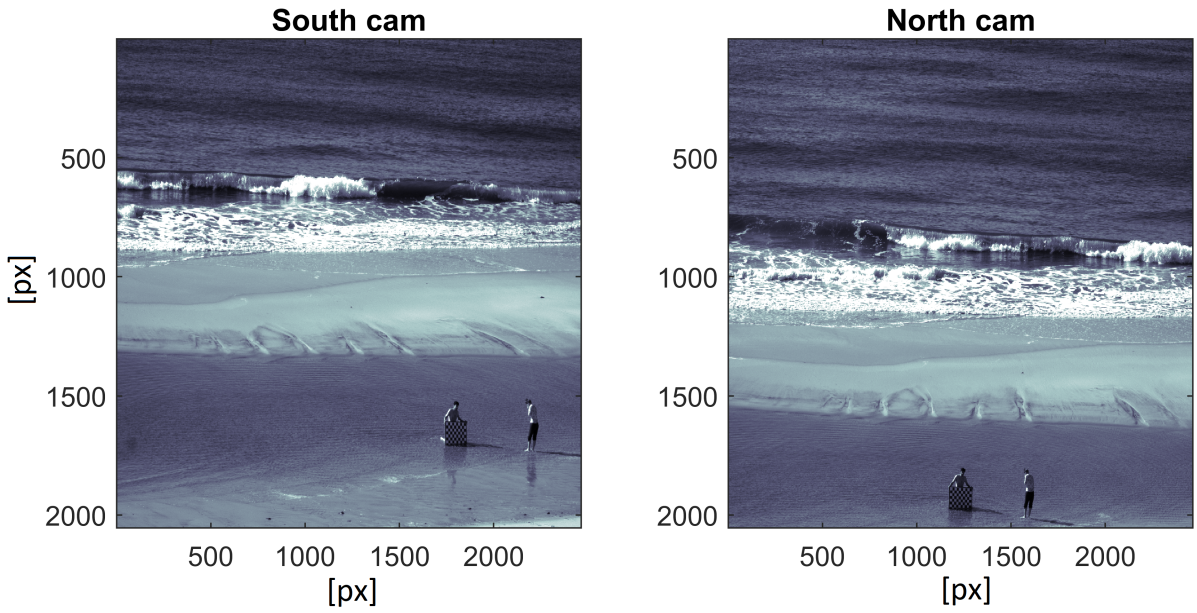

Figure 17: The checkerboard carried around the beach to calibrate the camera, seen here through the two cameras

5 Experiment at Sylt (2019)

In September 2019 [Bjørnestad, 2021] was doing a measurement campaign at a beach located at the German island of Sylt. Here they were tracking oranges as surface tracers together with a stereo imaging system to research particle trajectories. Important for us is that during their experiment they mounted poles at low tides which were located by a GPS tracker, installed a buoy outside the coast which tracked the incoming wavefield, and stored all the pictures taken by the cameras. These data could therefore later be used to validate our numerical estimates of the particle velocity field.

But the data obtained by Bjørnestad et al. is not enough to run a numerical model. It is also necessary to have the local bathymetry at least as far offshore as the buoy they used to record the wavefield. Therefor LiDAR data supplied by the Landesbetried für Küstenschutz Nationalpark und Meeresschutz Schleswig-Holstein (LKN.SH) over the island and surrounding ocean was connected together with the coarse grid of the North Sea from the European Marine Observation and Data Network (EMODnet).

The following chapter describes how we included the data from Bjørnestad et al. and the bathymetry.

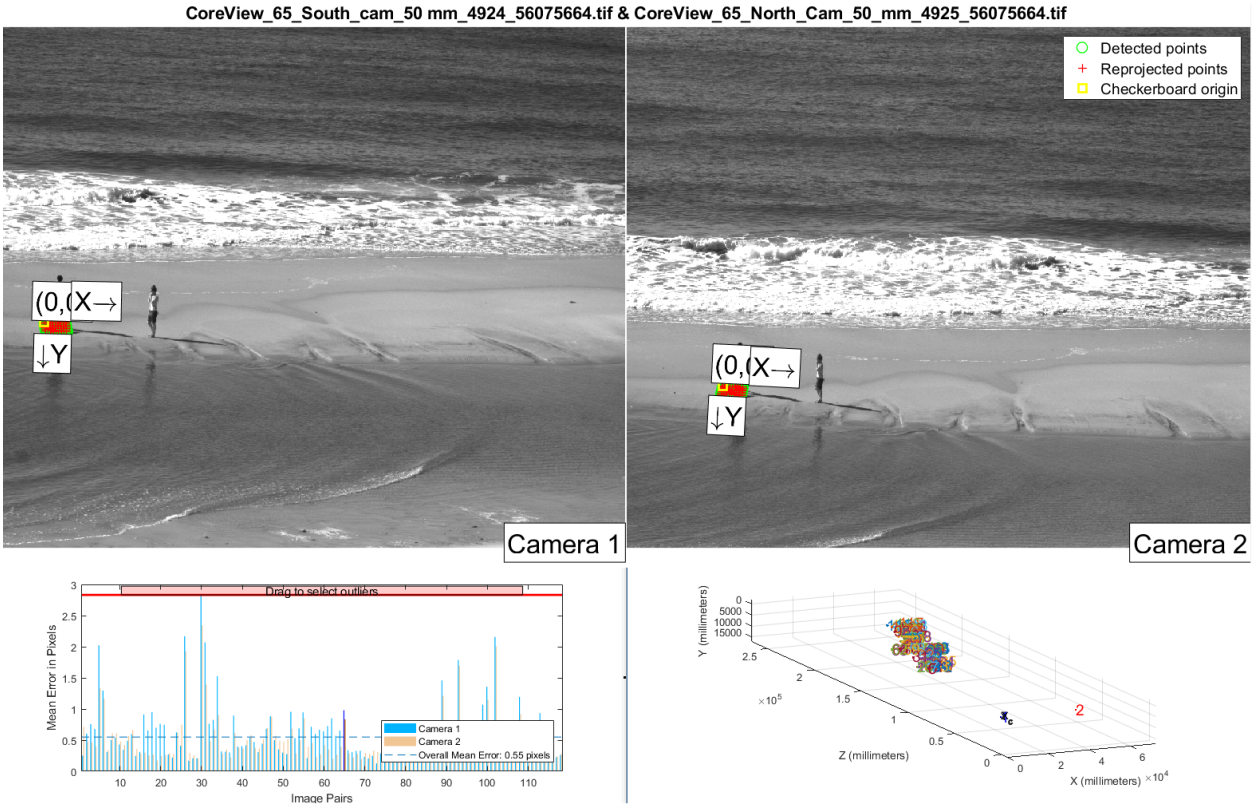

Figure 18: The calibration software supplied by MATLAB. In the top row is the reprojected checkerboard locations for one image pair. In the bottom left the error of these reprojections is shown for each pair of images and in the bottom right the locations of the checkerboard in the cameras coordinate system is shown.

5.1 Orange tracers

After arriving at Sylt and setting up the cameras, a checkerboard was carried around inside the field of views of the cameras (see image 17). This was done to collect multiple pictures of a known geometry from multiple angles and locations for MATLAB to later calibrate the cameras. By choosing a subset of these images MATLAB can create the matrices for the stereo cameras. About 120 pairs of images were chosen to create the above image, which created a geometry which matched with the known distances of the testing area (see Fig. 18).

Now by finding all the pixel values of the tracer's path, MATLAB can recreate the path in 3D world coordinates. The following days poles with known coordinates were set up, and during high tide oranges were thrown out onto the sea (Fig. 19). Here it was now possible to follow the tracer's position on the images by a script created by Marc Buckley. By supplying the initial position of the oranges, it follows the locations of the whitest pixel values in the surrounding areas. This means on the other hand that it is difficult to follow the orange through breaking waves, since the white-caps

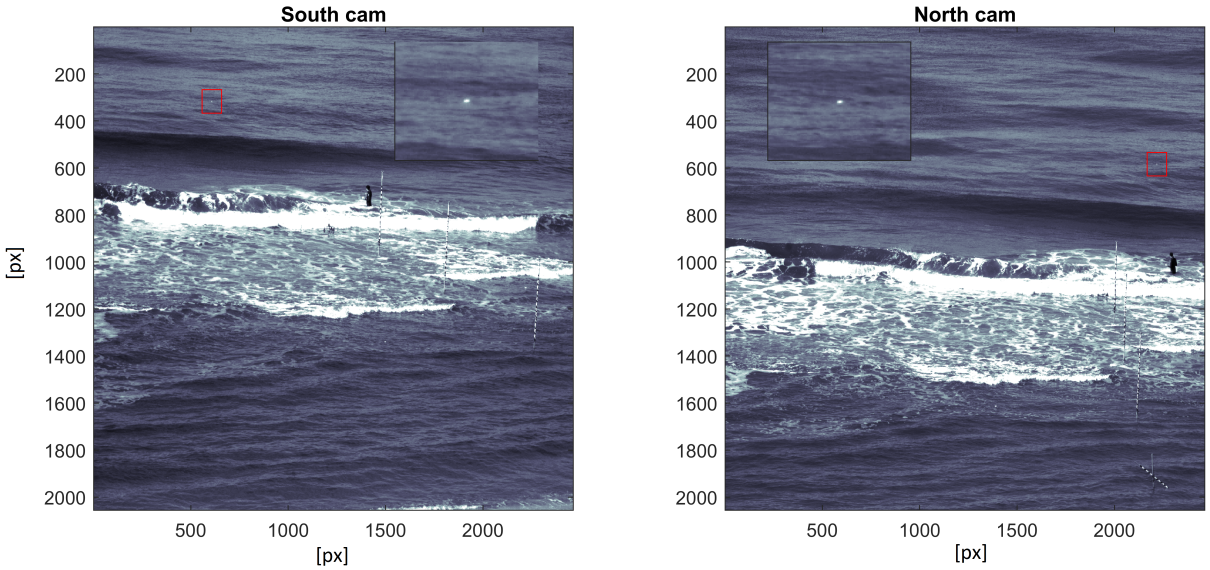

Figure 19: Full picture of an orange inside the cameras field of views. The red box is zoomed into in the upper pat of the images to show the orange. As the orange moves it is tracked through the water.

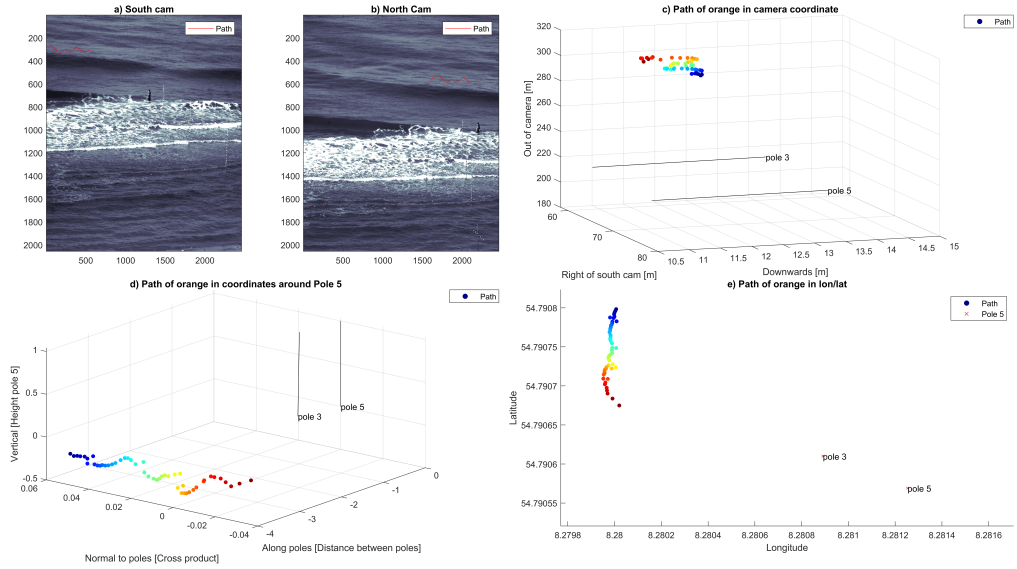

Figure 20: The steps from pixel values to WGS84. a) Pixel values of the oranges path. b) The world coordinates of MATLABs triangulation function. c) The path in Bjørnestad et al. coordinate system. d) The path in WGS84 where the height is truncated.

hides the orange. In this picture an orange which is outside the breaking waves is tracked instead (Fig. 20).

After tracking an orange, one can use MATLABs inbuilt triangulations function to find the world coordinates of all the pixel points the orange has occupied. But the original coordinate system which MATLAB supplies is not useful for us, hence it is necessary to change it. I followed Bjørnestad et al. proposal for a coordinate system, where a orthogonal right handed coordinate system which x- and y-basis vectors is parallel to the sea surface is found between the poles. After this it was necessary to rotate these basis vectors around the z-axis to line the x- and y-axis with the North and East basis vectors of WGS84 as described in Ch. (1.5) such that the locations can be plotted together with the bathymetry described in this datum.

5.2 Spectrum

5.2.1 Buoy data

The data gathered from the buoy outside Sylt contains various data regarding the wavefield for every half hour throughout the 7th to 8th of September 2019. An extract of this data is shown to the right and below.

It consists of 12 rows of data containing one of which is the reference PSD of which the PSDs below are relative to. Below are the main data from the buoys (table 2). They consist of columns describing the frequencies f, relative PSD $E(f)_{rel}$, main direction of propagation D_P, spread σ_θ, skew, and kurtosis.

5.2.2 Implementing 2D spectra from 1D spectra

The fact that we have more information about the wave field than [Pierson Jr et al., 1971] had in Ch. (1.6) means that we can implement a more sophisticated guess about $D(\theta)$. To incorporate the information about main direction and spread I propose the modified function:

Table 2: Example data from buoy.

Freq. [Hz]	$E(f)_{rel}$ **[-]**	D_P [°]	σ_θ [°]	**Skew [-]**	**Kurt [-]**
0.025	4.17E-05	275.6	56	-0.39	3.63
0.030	1.30E-04	267.2	53.5	-3.93	4.04
0.035	1.11E-03	278.4	49.4	-0.48	3.06

$$D(\theta) = \begin{cases} a\,cos^2(k(\theta - D_P)) & \text{if } D_P - \sigma_\theta \cdot \text{fac} \leq \theta \leq D_P + \sigma_\theta \cdot \text{fac}, \\ 0 & \text{else} \end{cases}$$

Where D_P and σ_θ denotes the main direction and spread of a given frequency, and fac is a factor larger than or equal to 0.

To determine the constants a and k I have solved the system of equations,

$$\begin{aligned} \int_{D_P-\sigma_\theta\cdot\text{fac}}^{D_P+\sigma_\theta\cdot\text{fac}} a\,cos^2(k(\theta - D_P))d\theta = 1 \\ a\,cos^2(k(\sigma_\theta \cdot \text{fac})) = 0 \end{aligned} \tag{123}$$

Which yields,

$$a = \frac{\pi}{4 \cdot \sigma_\theta \cdot \text{fac}} \quad \text{and} \quad k = \frac{\pi}{2 \cdot \sigma_\theta \cdot \text{fac}} \tag{124}$$

Now to use these results together with the input data it is necessary to discretize both the frequency and angle. This is done with the following discretization:

$$f_n = \{f_1, f_2, ..., f_n\} \tag{125}$$

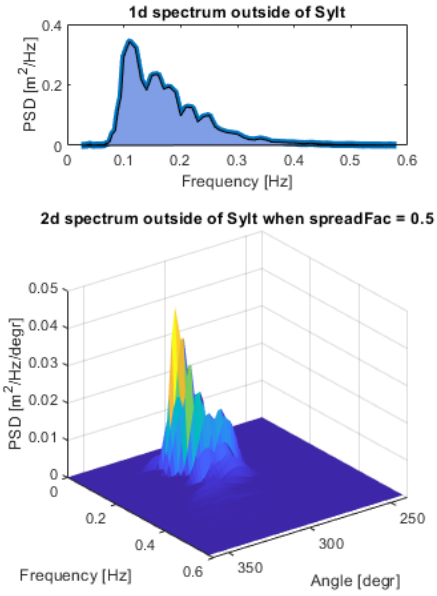

Figure 21: Example of one of the spectrum used in the Sylt experiment. On top the original 1D spectrum is plotted. Below you can see the recreated 2D spectrum using a cosine squared function as $D(\theta)$ for each frequency and spread, where this particular function uses $fac = 0.5$.

$$\theta_n = \{\Delta\theta, 2\Delta\theta, ..., n\Delta\theta\} \quad \text{where,} \quad \Delta\theta = \frac{360}{n_\theta} \tag{126}$$

Then for each f_i find the θ_m and θ_n such that $max(\theta_m) \leq D_P - \sigma_\theta$ and $min(\theta_n) \leq D_P + \sigma_\theta$. For every θ_j where $j \in [m, n]$ the PSD at this index is then evaluated as:

$$E(f_i, \theta_j) = \frac{E_{max}}{\Delta\theta} E(f_i) \cdot D_i(\theta_j) \tag{127}$$

Where D_i is the directional function for this frequency.

Now the only data accounted for is the first four columns, and the relative PSD. It could be possible to include the skewness and kurtosis if one used the normal distribution as a base instead.

5.3 Bathymetry

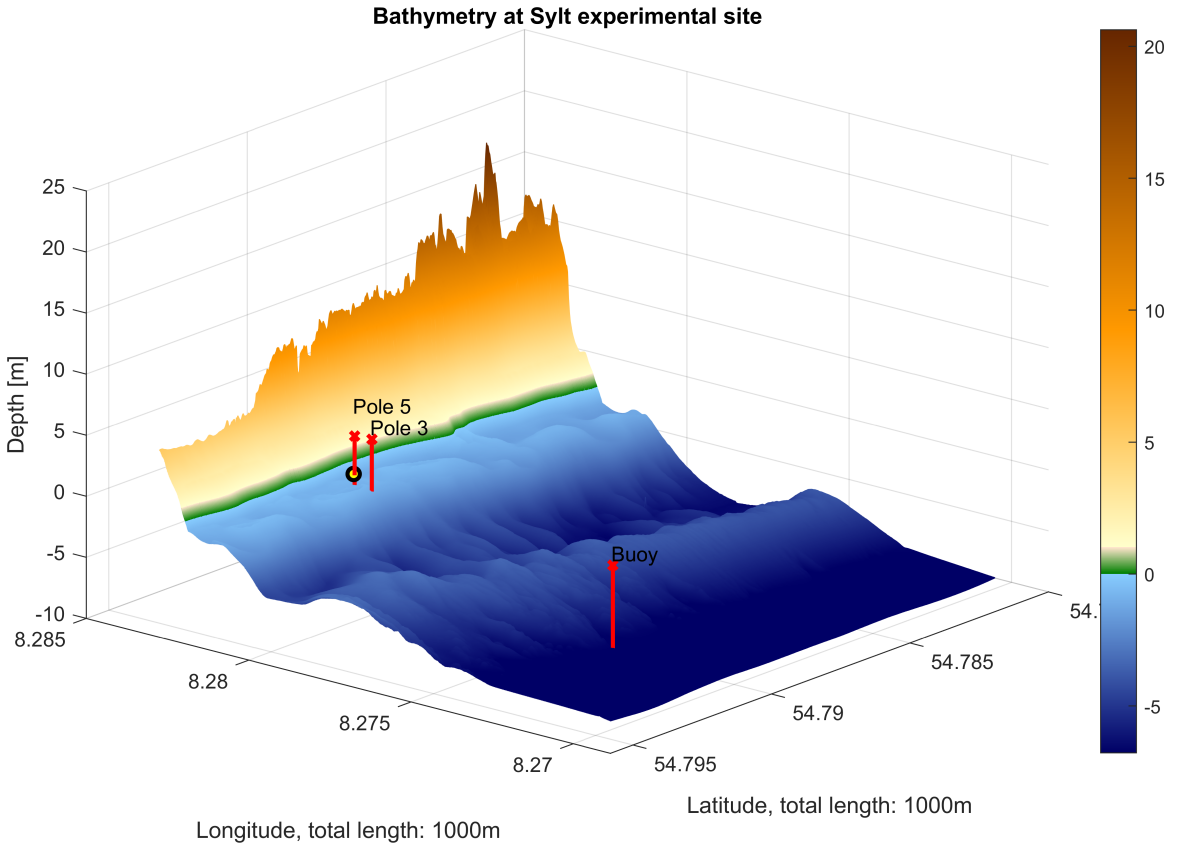

Figure 22: The supplied bathymetry around the experimental site on Sylt. The height of the Island and surrounding ocean floor. Two poles and the buoy location is plotted in red, and the yellow ball is the starting location of the numerical tracer corresponding to the orange.

Since our hypothesis is that the circulation in the surf zone is strongly influenced by the bathymetry it is crucial that we have an as exact replication of the real-world situation as possible. To do so we combine multiple data sources through the work of Volker Roeber. We get our data from two different sources, the relatively coarse EMODnet bathymetry of the North Sea [emo, 2022] and a finer LiDAR scan of Sylt island done by Leica on behalf of the LKN [Lei, 2022].

The main grid used in the picture above of the bathymetry is the LiDAR scan supplied by the LKN. This dataset was originally scanned by drone with a resolution of 10 by 10 cm over the entire island of Sylt at in June 2020. The data from supplied to us after contacting the responsible person in the LKN. It is unfortunate that the dataset is from 9 months after the experiment, as the sandbars are probably moved significantly when the data was collected compared to the experi-

ments. Nonetheless it is the best we can do. To compensate for this we are simulating the tracers for various water heights such that the errors hopefully cancel.

The LiDAR data was only collected to about 600 meters off coast. This was not enough for our use since the Buoy was located further off-shore and at deeper depth. Hence it was necessary to find some other data to fill the outmost gap of the domain. The EMODnet online supplied data was used for this task, which is a rough grid with a resolution of about 115 by 115 m. This dataset is used wherever the LiDAR data is not measured, which is farthest offshore at depths lower than 6m. For all practical purposes this dataset encompasses only small parts of the domain, as all depths deeper than the buoy location is set to the buoys depth.

To fit these two datasets together they were interpolated to a grid size of 2 by 2m, which also define a mesh which is practically possible to simulate. After doing this for the entire site of Sylt, it is only a matter of choosing a subset of the entire domain to simulate. In the above picture a 500 by 500-point grid is extracted, but in the results section a 1000 points alongshore by 500 point normal to the shore grid is used. Lastly, to avoid excess shoaling of the incoming waves the bathymetry is cut off at the water depth of the buoy.

5.4 Inclusion in BOSZ

The bathymetry data is most likely not correct as the sandbank would have moved in the time since the experiments. Therefor we simulate the tracers for different water heights around the true tide level of the time to compensate for this movement bathymetry, of which we chose $tide = \{-0.20, -0.25, -0.30\}m$.

The buoy data is reconstructed to a 2D plot as described in Ch. (5.2.2) with the spread factor as $\{0, 0.5, 1\}$ before being simulated in BOSZ via the wavemaker as seen in Ch. (2.1.6). Here an additional parameter we are changing is the spread, which is multiplied by a changing factor. The reconstructed orange path is used to create the initial position and velocity of the numerical tracers. Here we place 100 tracers randomly in a circle of radius 20cm to compensate for errors in the location of the oranges, we also add a random component to the measured velocities of the oranges from the pictures which measures $\pm 50\%$. After 500 seconds have passed and the wave setup is complete, the tracers are added to the simulation and each of them are simulated independently before being averaged in an ensemble.

For each of the pair of variables above we run the simulations for 6 different random seeds for the phase angles described in Ch. (2.1.6). After the simulation is complete the results of the idealization of the wave fields are averaged to yield our final numerical drifter path.

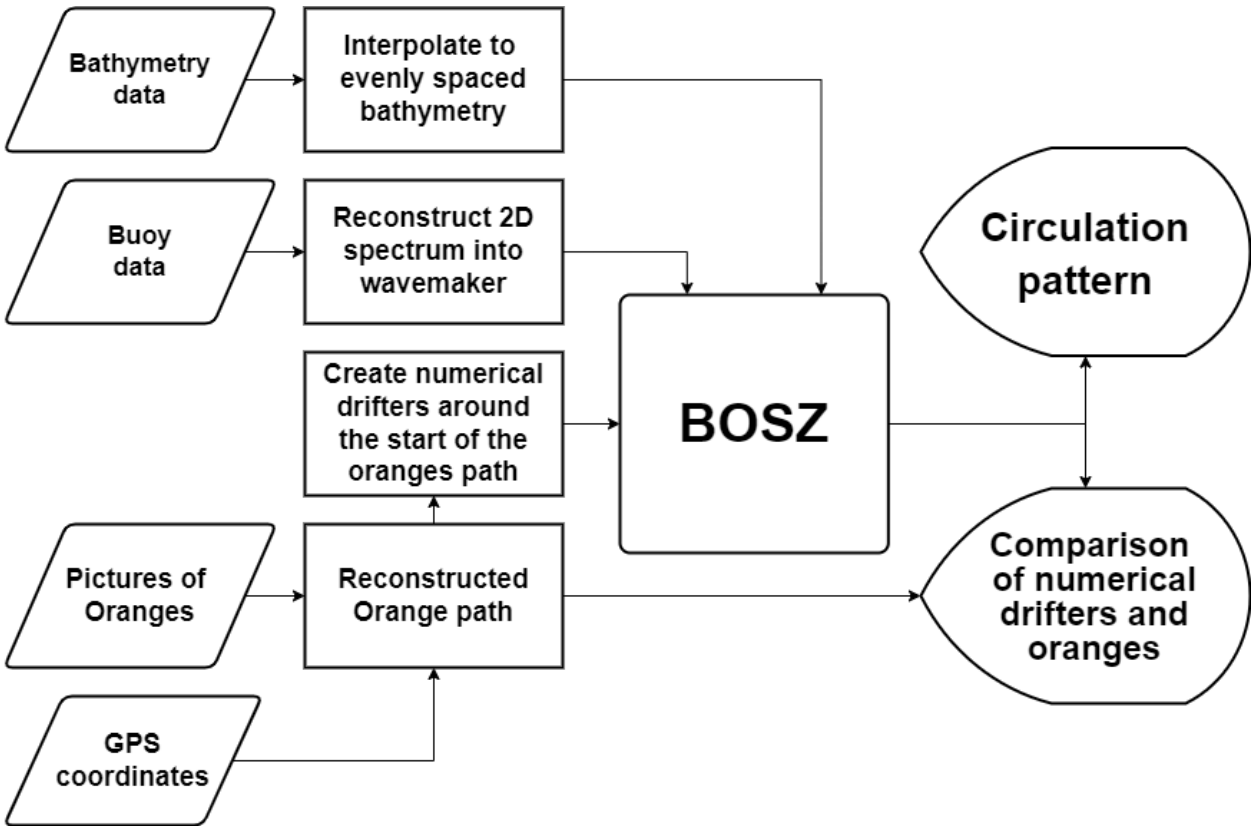

Figure 23: Flowchart of how the experimental data is connected to the BOSZ model.

5.5 Results

After simulating the numerical drifters the paths were post processed to look at the paths which they follow. The paths were stored in a 7-dimensional tensor with the dimensions: tide, σ_θ, seed, orange path, drifter, time, and X- or Y-coordinate. To plot the data it was necessary to reduce the dimensions to maximum three. This was done by creating a new X and Y grid where for every drifter we create a binary map where 1 means that the particle were in this location for any timestep. This creates the new 7-tensor with dimension: tide, σ_θ, seed, orange path, drifter, X-, and Y-index. To reduce the system and find the percentage of tracers going through any particular location is then a matter of summing the dimensions and dividing by the total number of instances summed together. In Fig. (24) this is shown for tide, σ_θ, seed, and drifters summed together such that the independent variables left are the orange paths, X-, and Y-index. Lastly the average position of the drifters of the drifters for the drifters for each orange path was calculated.

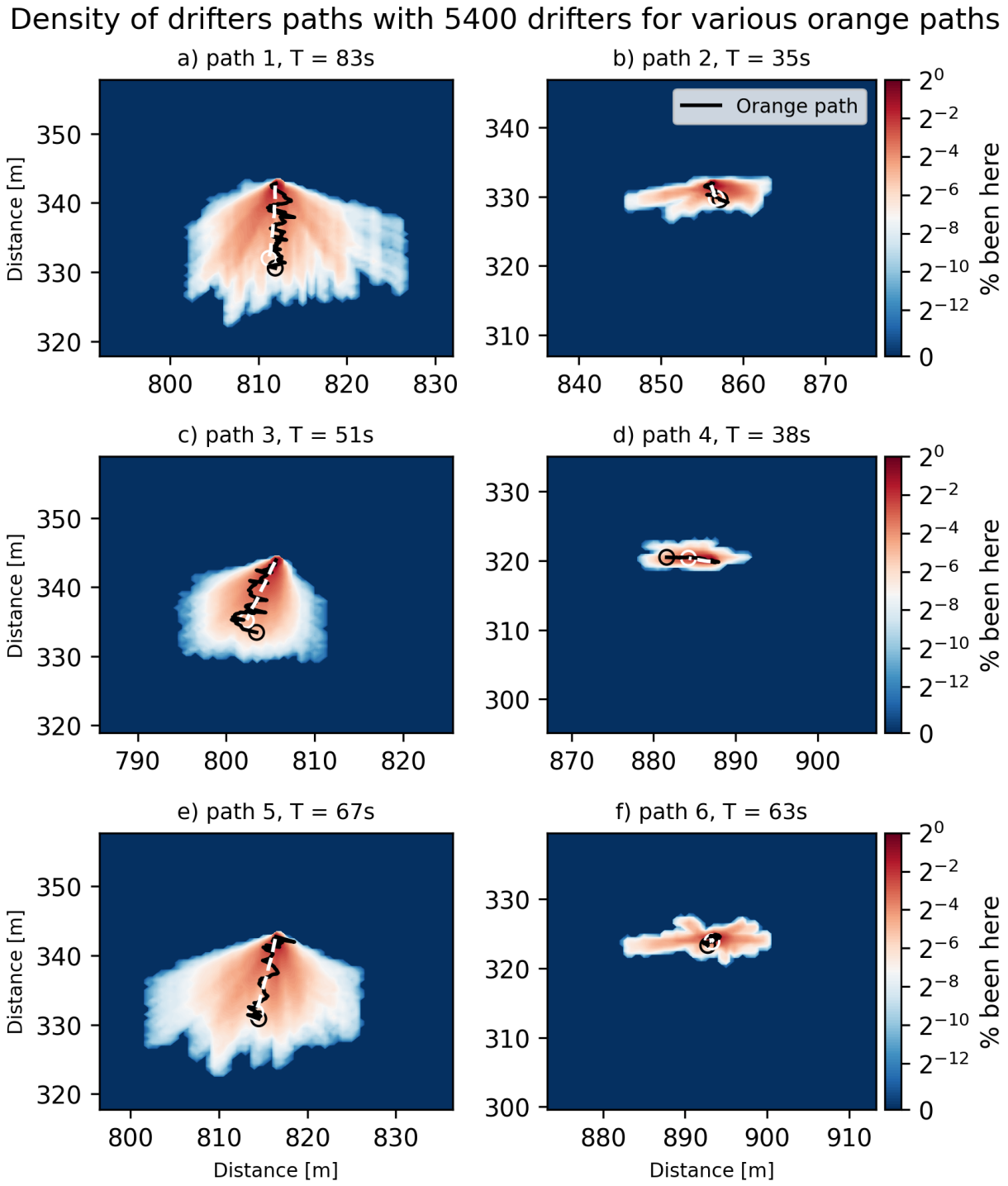

Figure 24: The results from the orange simulations. For each orange path a $40m$ by $40m$ area is plotted where every $0.5m$ by $0.5m$ grid cell counts how many numerical drifters have passed through that particular cell have passed after the T seconds the orange was tracked. This number divided by the total number of drifters yields the plotted values. The black path denotes the real orange while the white is the average path of all the numerical drifters. The particles in a), d) and e) was tracked outside the sandbar and shows large movements, while b), c), and f) was inside with less movement.

5.6 Discussion

The particles tracked in Fig. (24) come from two different conditions. There is a sandbar located at around $X = 830 - 850m$ so there is primarly here the waves break according to visual inspections of the pictures of the oranges. Path 1, 3, and 5 is located outside of the bar, and are hence moving through larger waves, but also have higher initial velocities. Path 2, 4, and 6 on the otherhand is located inside the sandbar, and have almost no velocity.

The average values of the numerical drifters show good resemblance to the oranges actual end position. It is noticeable that the oranges move backwards and forwards because of the waves, but the most important contribution to their movement seem to be caused by a much more slowly varying component. This is in compliance to the results of Ch. (4). The spreading of drifter location also makes sense. For oranges with larger movement, there is a larger spreading from the numerical drifters. Nevertheless the spreading in the model centres around the actual movement of the oranges.

Perhaps surprising is the dense streams of directions seen in the movement of the drifters inside the sandbar. Here there is multiple tight arms which multiple drifters seem to follow, which go in their own direction. The reason for this is best seen by choosing another independent variable than the orange paths. By choosing the seed to the RNG input to the wave phases Fig. (25) as the independent variable it is possible to see that the seed strongly influence these arms. This seem to indicate that the waves which they encounter first determine which direction they will follow.

This seems to be an effect from our conclusion from Ch. (4). Inside the surf zone specifically the IG components of movement is critical. As these components vary for timescales around the ones we measure the oranges, it is natural that our choice of seed determine which part of the IG wave is encountered and therefore is critical for which direction the drifters will move. This effect is also reflected for the drifters outside the sandbar to a lesser degree. Consequentially, it will be necessary for every computation of particles in the surf zone to include different seeds of incoming waves as the impact of IG-waves is both large and uncontrollable in such an environment. As it seems to the authors that that the average of these seeds are reflecting the actual movement and reflect the conditions of the day.

Even though our model have simplifications for reproducing the events we get reasonable results. The governing depths averaged Boussinesq equations (56), the uncertainty in the oranges exact locations and velocity together with impossibility of representing the exact wavefield, and half year late bathymetry with resolution 2×2m are all limitations for how exact we can expect the results to get. But still our results is representative and allow for further interpretation of the processes. We therefore continue our research into the fluid velocity in the surf zone.

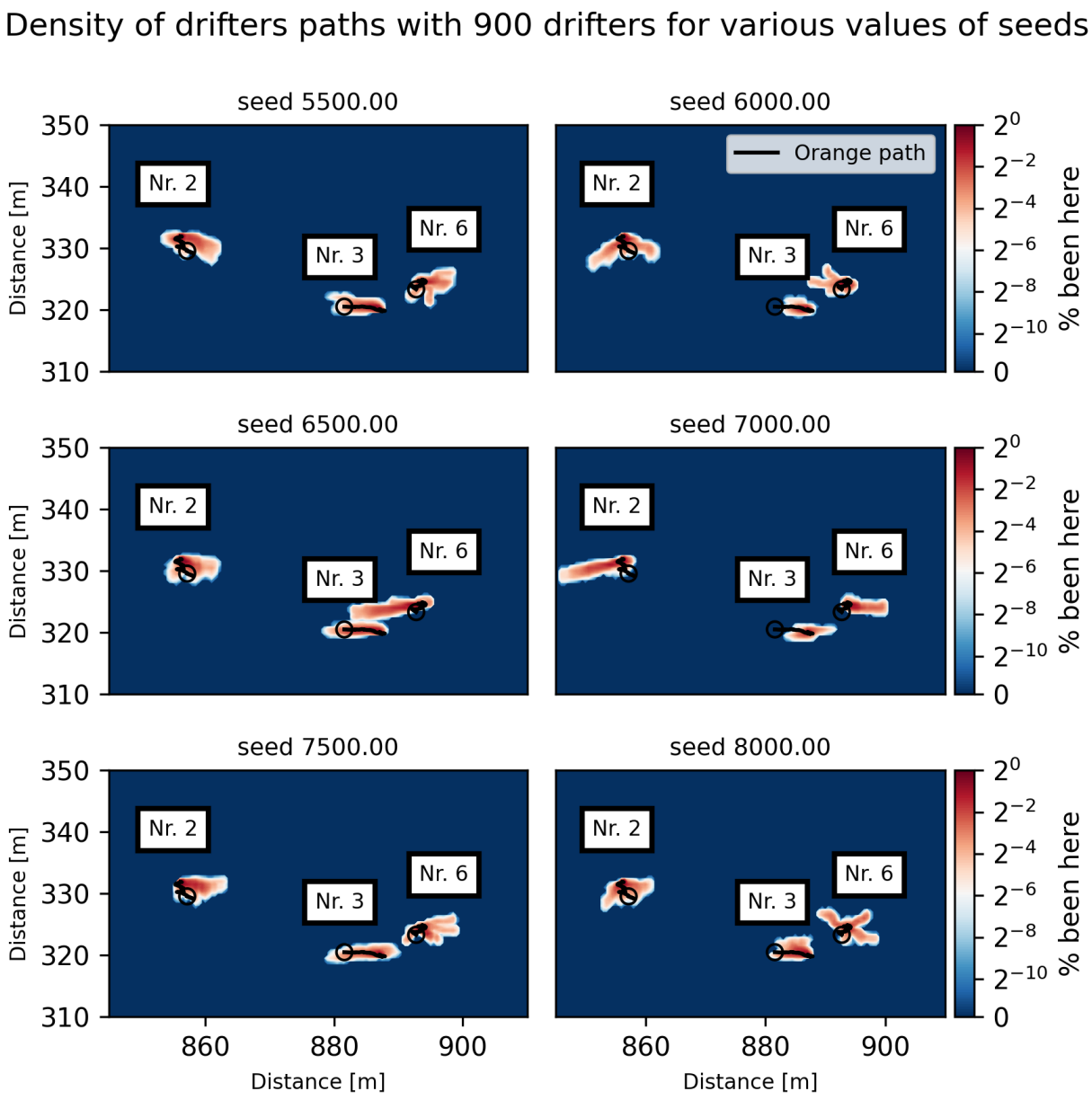

Figure 25: The movements of the three particles found inside the sandbar for the different RNG seeds used for the wave phases. These particles correspond to b), d) and f) in Fig. (24).

6 Vortexes at Sylt

In this section we will look at the dependence of the near-shore circulations on conditions with regard to the tide and wave field. Through simulation of various inputs in our bathymetry from Sylt we will identify and calculate the vortexes which arises in our domain before doing statistical analysis. We will compare the dependencies against the work of [Baker et al., 2021], [Choi et al., 2015], and [O'Dea et al., 2021] who all looked into the dependence of surf zone dynamics on the directional spread of the incoming wavefield.

We will also look at a larger scale comparison from [Scott et al., 2014] which in 2014 did a field experiment where they deployed drifters on beaches in South-western England. They identified three different behavioural groups, which we will compare our results against.

6.1 Methodology

6.1.1 Model input

The independent variables we are looking at are the tide levels, the spreading σ_θ of the incoming wavefield, and what the main direction D_P of the incoming wave field is. Through the buoy data from Ch. (5.2.1) we were able to see that realistic values of the latter two variables are $\sigma_\theta \in [0, 40]^\circ$ and the $D_P \in [270, 310]^\circ$. Further from using the OSU Tidal Prediction Software we found that the tide naturally varies between $-0.5m$ and $0.5m$.

We discretized these variables as follows: $tide = \{-0.5, -0.25, 0, 0.25, 0.50\}m$, $\sigma_\theta = \{0, 20, 40\}^\circ$, and $D_P = \{270, 290, 310\}^\circ$. Where the tide is modelled as a stationary change to the water depth. The spread is the width as in Ch. (5.2.1) with $Hs = 1.3153m$ and $Tp = 9.09s$ which corresponds to the spectrum from Ch. (5.2.1), and the main direction is modelled by inputting the wavefield from the wavemaker at an angle. All together this yields 35 different simulations.

While the bathymetry is considered to be static, a changing tide level impacts the depth of bottom features and therefore impacts the overall flow. The changing tide level can be interpreted as a change in bathymetry. Further wavefields approaching the beach at an angle have the potential to create large alongshore velocities, while having a higher spread allows the waves to come at multiple different directions and waveheights creating a varied incoming field. The goal is that with this discretization is to see results from the entire spectrum of realistic inputs from this location.

In addition the bathymetry is the same as described in Ch. (5.3) except that we now use the entire $1000 \times 2000m$ domain from the measurements. We also now use a standard JONSWAP spectrum, as this should represent the condition on Sylt, as it is located in the North Sea.

6.1.2 Finding vortexes

Each run is simulated for 3600 seconds, where the first 600 seconds are purely for initializing the wave field. After this initial period the ocean surface velocity is continuously averaged. This yields mean values for the velocity which we visually inspect (see Fig. (26)). These values represent where we can detect circular flow in the ocean over longer time frames like the pathlines observed by [Scott et al., 2014], in opposition to just spontaneous circular streamlines.

To find the locations of the circulations a rough review of the data is performed by a twofold method. The resulting flow is plotted as in Fig. (26) with the color representing velocity and a similar plot with the colouring instead representing the swirling strength as defined in [Buckley and Veron, 2017]. This first pass-through every location with a swirl or circular velocity is marked as a potential vortex.

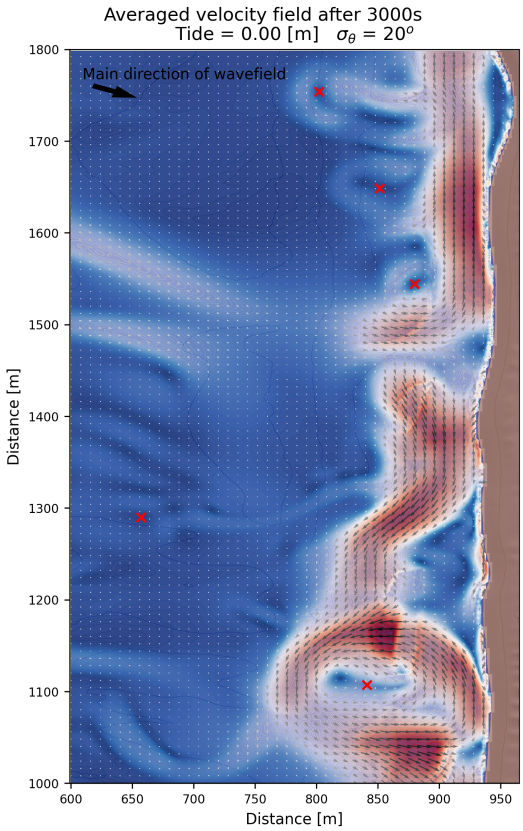

Figure 26: A subsection of the average velocity field for one simulation with multiple vortexes of different sizes and strengths. The red markers denote where we identified centres of vortexes.

After visually inspecting all the images like Fig. (27), the circulation is calculated for every one of them. This is done by integrating the velocity fields in circular paths for varying radii around the centres of the vortex. Then the maximum circulation is identified by a simple forward difference, which is manually inspected and corrected if necessary. During this a finer vortex identification criterion is used to determine whether the rough locations indeed were a vortex. To count as a vortex the flow need to fulfil the following criterion:

- The center of the vortex is identified as a region of zero flow, since near the center of revolution real vortex flow is nearly solid-body rotation [Kundu et al., 2015].
- There must be a closed circuit of pathlines to count as a vortex.
- The circulation value must be a local maximum, to mark the beginning of the end of the vortex.

This maximum circulation and the corresponding radius is stored together with the independent variables for later statistics. See Fig. (27) for an example.

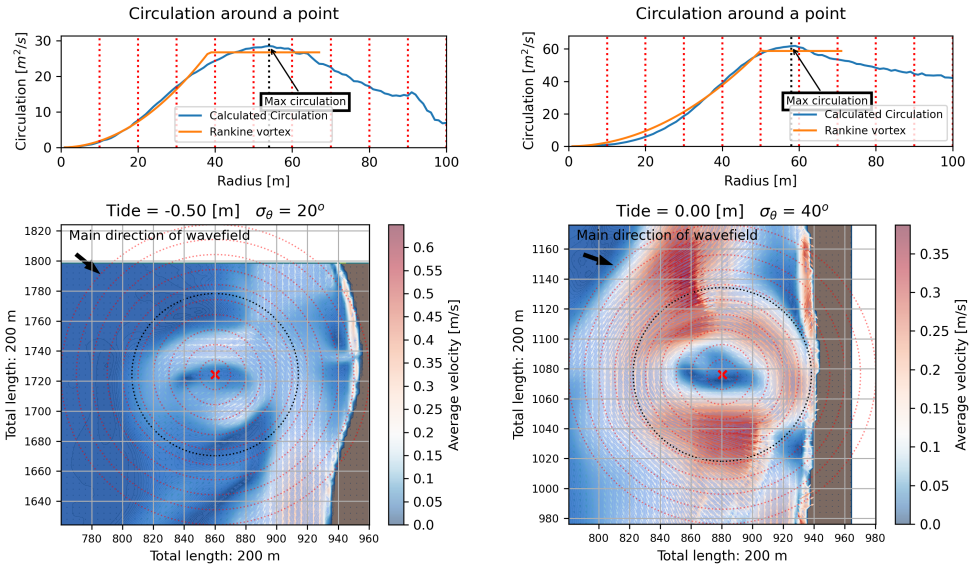

Figure 27: The visual inspection of the circulation around a point for a set of independent variables. Bottom: The surrounding velocity field. The red cross denotes the centre, and the dotted circles shows the radius of factor 10. Top: Shows the circulation around the point for various radii. The dotted red lines denote the radius of factor 10, and the black cross shows the maximum circulation around this circulations. The orange line define the best fit Rankine vortex for these circulation where the maximum circulation $Gamma = \{28.52, 61.71\}m^2/s$ and radius of transition $\sigma = \{40.07, 57.45\}m$ for the left and right vortex respectively.

6.1.3 Statistics

We want to quantify whether or not any differences of the means of radius and strength are statistically significant or not. Thus it is necessary to conduct a statistical test, of which we are using a three-way ANOVA. This test looks at the means $\mu_{ijk} \approx \bar{x_{ijk}}$, where the indexes indicate the value of tide, σ_θ, and D_P. We are interesting if any one of the variables, or an interaction between them, impacts the means to a significant degree. We thus create the 3-way ANOVA models:

$$\text{radius} \sim \text{tide} + \sigma_\theta + D_\theta + \text{tide} : \sigma_\theta + \text{tide} : D_\theta + \sigma_\theta + D_\theta + \text{tide} : \sigma_\theta : D_\theta$$
$$\text{strength} \sim \text{tide} + \sigma_\theta + D_\theta + \text{tide} : \sigma_\theta + \text{tide} : D_\theta + \sigma_\theta + D_\theta + \text{tide} : \sigma_\theta : D_\theta$$

After identifying the vortices and calculating the dependent variables as described in the previous section, we use the *python* package *statsmodels* to conduct the ANOVA test and provide the results.

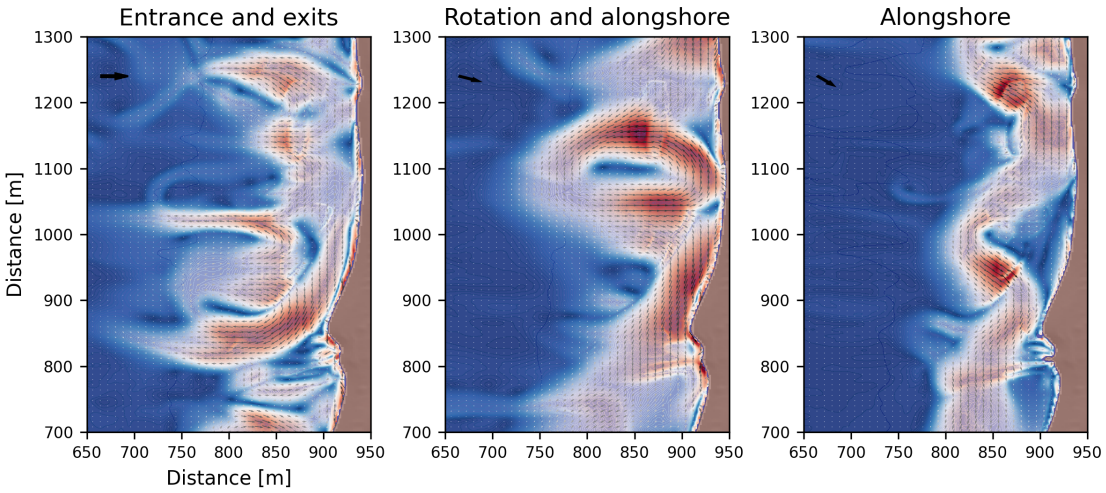

Figure 28: Examples of the three types of large scale velocity behaviour from the same location for different model inputs. Left: Here the velocity enters and leaves the shoreline. Middle: A large vortex is seen in the upper part of the image. It is fed "mass" from the above and feeds into the alongshore current below. Right: A alongshore flow is seen.

6.2 results

6.2.1 Visual comparisons

Plotting the velocity results and visually inspecting them yields a striking resemble to the work of [Scott et al., 2014]. They found that there exist three primary behavioural groups by the large scale velocity pattern, that they consist of fields pointing outwards to sea, circles nearshore, and alongshore inside the surf zone. In our simulation we found the identical groups of data, in addition to one similar to, but in opposite direction of, exit flow which we call entrance flow. See Fig. (28) where you can see these four groups of velocity. In this plot we replicate the plot from Scott et. al. where we have plotted a subdomain of dimensions $300 \times 600m$ for different initial conditions.

Further they found that while these are the dominant groups, the particles they followed in their experiment showed that while they might for example initially follow a circular path but after a circulation they would be sent out to sea or down along the shore. A result which suggest one group is connected to another. Via such deduction and further simulation form their location that found the following: 1) At the sides of exits there exist rotations. 2) On the side of alongshore flow which faces the sea, there appears smaller exits 3) Inside alongshore flow there exists rotations which the alongshore flow swirls around. All of these phenomenons appears in our dataset as well. This indicate that the resulting flow from our inputs to BOSZ and the resulting output reflects real possibilities of flow.

Looking at the first row of Fig (29) also exemplifies the influence of the ratio of incoming significant waveheight and local morphology. [Scott et al., 2014] noted in their field experiments that when the tide is at such a level that the incoming wavefield breaks over the inner bar the maximum currents would develop. This would happen when the tide, and thus morphology, was a little lower than the necessary wave height to water depth breaking condition. This simultaneous breaking thus create more organized breaking in the surf zone causing higher values of velocity [Martins et al., 2022], which in cause flow to circulate in larger scale patterns with higher values. As seen in Fig (29), the lower tide level means that waves break before the sandbar at different spatial locations yielding a cancelling of large scale flow. At tide levels around 0 the sandbar depth is optimal for organized flow, before at higher tides the resulting flow decreases again.

Plotting some of the averaged velocity fields for different values of σ_θ yields the middle row of Fig (29). Here it is possible to see as [O'Dea et al., 2021] found that less directional spreading is associated with larger velocities in the surf zone since more spreading yields more and higher variability in the transient flow. [Choi et al., 2015] notes that the decrease in alongshore flow is a consequence of multidirectional phase interaction in the nearshore region yields less wave-induced momentum flux based on the moments of the wave energy spectrum. As noted in both [Baker et al., 2021] and [O'Dea et al., 2021] this does not decrease the energy associated with the wave field nearshore, but the resulting wavefields increases the short-scale fluctuations of the velocities and therefore cancels on average.

Lastly, the main direction of the incoming wave field D_P greatly influences the alongshore flow. With the mean direction being normal to the beach there would be zero net momentum in the alongshore direction, it is therefore expected that this results in the least amount of alongshore movement.

It is also evident most of the vortexes appear inside the surf zone as seen on the right side of Fig. (29). All of the vortexes found outside the surf zone is due to exit flows which can extend to 1-2 surf zone widths beyond the surf zone edge, and as noted by Scott et al, vortexes appear around these rip currents. The morphology is also critical for the formation of vortexes as the wide and strong vortexes appear at the sandbar. This happens as it is here the velocity of the flow is highest [Martins et al., 2022] and generated vortexes are trapped inside the through [Bühler and Jacobson, 2001].

6.2.2 Nature of circulation inside vortexes

In theoretical fluid dynamics it is common to divide vortex into solid body rotation where the circulation $\Gamma = 2\pi r^2 \omega_0$ is increasing as a parabola with increasing radii, and irrotational vortexes

where the circulation is constant for all radii $\Gamma = 2\pi B$ [Kundu et al., 2015]. In real life no vortex are purely a solid body rotation or an irrotational vortex, and what we see is often an Rankine vortex:

$$\Gamma(r) = \begin{cases} (\Gamma_{max}/\sigma^2)\, r^2 & \text{if } r \leq \sigma, \\ \Gamma_{max} & \text{if } r > \sigma \end{cases}$$

Where there is two parameters: σ which determines for which radial distance the vortex characteristics switches from SBR to irrotational, which is an abrupt transition, and the maximum circulation Γ_{max}, the maximum circulation of the vortex which happens when $r \geq \sigma$ [Kundu et al., 2015].The Rankine vortex thus consists of a core where the rotation is nearly solid body rotation, where there exist increasing vorticity and circulation, and an outer region where the vorticity is 0 and circulation constant.

We went through all identified vortexes and found the best fit values for Γ and σ in the L_1 norm, where two of the resulting vortexes are plotting in Fig. (27). Here we can easily see that the cores indeed are nearly solid body rotations for these circulations, which is also true for all the identified vortexes. Typical of these plots is that for circulation close to the centre the Rankine vortex is close, but close to $r = \sigma$ the true circulation is almost linearly increasing. A reasonable result as there is no reason to expect a real function to be non-differentiable, and a smooth transition from one form of characteristics to the next should be expected. The irrotational part of the vortexes also does not last indefinitely as indicated by a true Rankine vortex. As we increase the radius other parts of the domain have a more significant role and the circulation is no longer reminiscent of a Rankine vortex.

This is obvious as described in [Scott et al., 2014] all vortexes along the surf zone exists alongside entrance, exit, or alongshore flow. Thus it can not be expected that these patterns exists for all time, but for some radius higher than the maximum circulation of each vortex we find that the nature of circulation is approximately a Rankine vortex. In Fig. (27) the left vortex is part of an alongshore current and the right vortex has an alongshore current above it which feeds into it before continuing into an entrance below it. In this right figure the circulation spikes again, but this is purely due to the large velocity in the entrance flow, and does not fit our definition of a vortex.

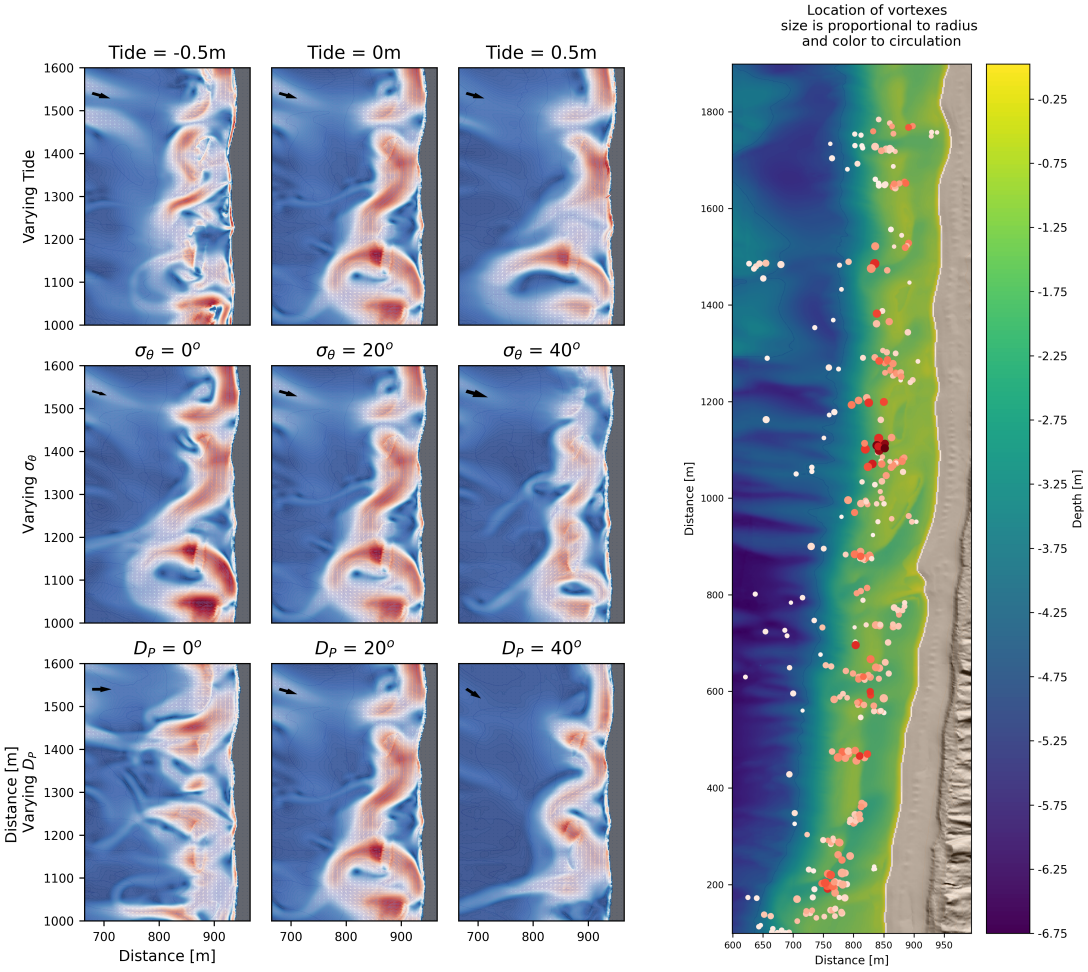

Figure 29: Left: The qualitatively dependencies of the flow on the variables studied in this thesis for a subdomain of the beach. The middle column shows the average flow field for tide $= 0m$, spread = 20^o and D_P = 20^o. For each row one of these variables are changed. Right: The location of all the vortexes for all the simulations.

6.2.3 Statistical results

Going through the velocity fields and marking all the vortexes and calculating their radii and circulation as in Fig. (27) yields 343 individual vortexes. Plotting these values on histograms yields Fig. (30) a). Here it is evident that the radius is closely gamma distributed, which means that the log transformed data is almost normal distributed as seen in the plots. The circulation strength on the other hand does not look like a recognizable distribution. Either way both diagrams seem to indicate that most circulation are weaker than $\approx 60m^2/s$ and have a radius in the range of $r \in [20, 60]m$. The radius and circulation of the vortexes are dependent on each other on a linear relationship, where increasing radius entails increasing circulation strength but with larger standard deviation.

Looking at Fig. (30) b) indicate the dependence of larger and smaller vortexes on our parameters. The number of vortexes reaches a maximum while the tide is neutral, with almost twice as many vortexes as with high or low tides. The distribution of large and small vortexes also change with changing tides, with increasing share of large vortexes for higher tides. Sorting the number of vortexes by directional spread does not seem to have a strong influence on the number of vortexes, but the distribution of them is highly dependent on the value of σ_θ. Larger spread is correlated with more small vortexes. Lastly D_P is a critical factor for the amount of vortexes, where an incoming wavefield which is normal to the beach yields twice as many vortexes as when $D_P = 40^o$. Meanwhile the sizes of the vortexes is not clearly correlated with this

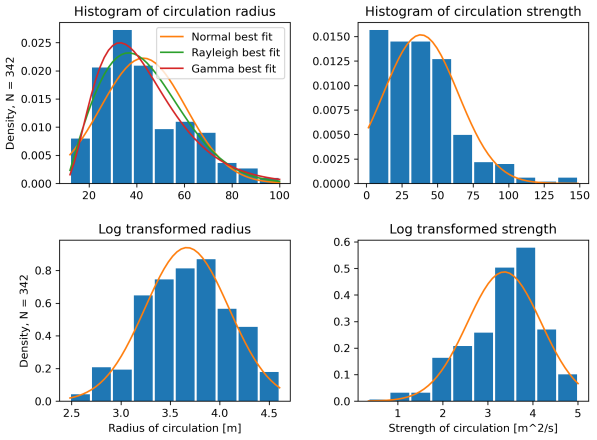

(a) Strength and radii with all parameters combined

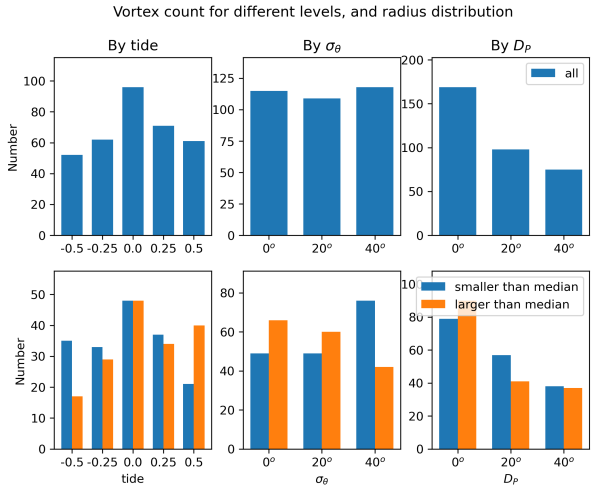

(b) Number of vortexes by parameter value.

Figure 30: a) The histogram of the raw and log transformed data of all the vortexes radii (left) and circulation strength (right), together with the best fit normal distribution. b) Top: The combined number of vortexes for different values of tide, spread, and D_P. Bot: The number of vortexes divided by if they are smaller or larger than the median radius of the vortexes.

Table 3: p-values from the 3-way ANOVA for the radius and circulation of vortices. The statistical significant variables are shown in bold at the level $\alpha = 0.05$.

Dependence	p-values	
	Radius	Strength
tide	**1.4e-2**	5.6e-2
σ_θ	**1.8e-4**	**3.6e-15**
D_P	5.7e-2	**4.9e-2**
tide:σ_θ	4.7e-1	3.7e-1
tide:D_P	3.3e-1	5.2e-1
σ_θ:D_P	2.9e-1	**1.4e-3**
tide:σ_θ:D_P	9.2e-1	9.9e-1

parameter.

Looking at boxplots of the values of radius and circulation for all the parameters yields Fig. (31). Looking on this there seems to be a decreasing relationship of vortex radii and strength with the directional spread as well as an increasing relationship with tide and radius, something which corresponds well with Fig. (30). There also seem to be no dependence on radii on the remaining variables. Hence the main direction of the incoming wavefield does not appear to have an impact on the parameters of vortexes, while the tide only affect the size of them.

Using the data from Fig. (31) to conduct the 3-way ANOVA as described in Ch. (6.1.3) yields the results seen in table (3). Here it shows that the radius of the vortexes are influenced by the tide and directional spreading σ_θ, and that the circulation strength is influenced by the spread σ_θ, main direction D_P and an interaction between them. To know whether or not these results are valid it is necessary to

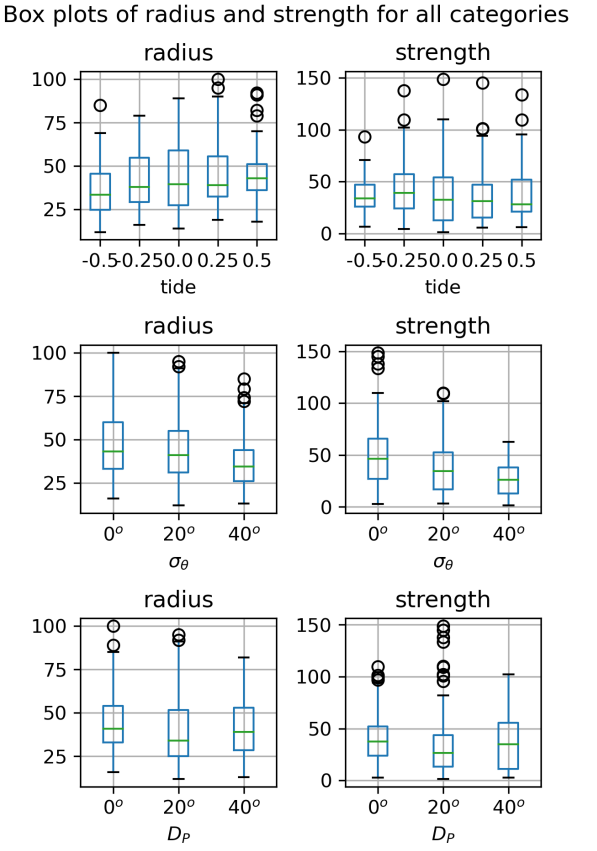

Figure 31: The box plots of vortex radius and circulation strength for all the variables. The leftmost boxplots are for the radius and rightmost for the strengths.

check whether or not the residuals of our statistical model is normal, and if we have outliers in our data. This is done in Fig. (32) a), where we can see that the radius' residuals are satisfactory normal and the conclusions from the ANOVA test for these are valid. For the circulations on the other hand there are ≈ 7 values which are larger than expected. Unaccounted for these values would skew the means higher and influence the test, but removing them did not influence the results of the test. We therefore conclude that the results for the circulation is also valid. Lastly the effects of the interaction is plotted to visualize the effect in Fig. (32) b). Here there seems to be a large influence on the circulation strength of the vortexes for some specific values of the wave fields main direction and spreading. While on average the influence of the main direction D_P on the circulation strength is to reduce it as seen in Fig. (30) b), for $\sigma_\theta = 40^o$ it first increases it before decreasing again implicating that there is a complex interaction between these two parameters.

6.3 Discussion

Depending on the incoming waves, surf zone dynamics feature a variety of flows, including longshore currents, entrance and exit flows, rip currents and in many cases vortices of varying size and strength. Close to the center, vortices in the surf zone are very close to pure solid-body rotation, while with increasing distance from the center, the flow becomes nearly irrotational. As such, the flow can be well represented by a Rankine vortex [Kundu et al., 2015].

The nature of the main features of the flow as well as details such as size (radius) and strength (circulation) of these vortices are determined by multiple factors. In the present work we have looked at how the tide level, direcionl spread of the wave spectrum, and the mean direction of the wave field affect the nature of the nearshore flow field.

The bathymetry is critical for the formation of vortexes, especially the depth of the sandbar. We found that when the tide is at some ratio compared to the depth of the sandbar, there is a large number of organized circulations present in our domain as seen in Fig. (30). When much of the incoming wave energy breaks at the same location they seem to feed into energetic and organized movement, in the form of vortexes in our study but also rip currents as [Scott et al., 2014] found. The local bathymetry must also be a factor with regards to the size of the vortexes, as Fig. (30) shows that the predominant share of vortex size changes from small to large for changing tide.

Analysing the impact of D_P of the wavefield it is also evident that the largest factor for the vortex formation. The intensity of the longshore flow decreases towards its offshore and onshore boundaries (see Figure (28), right panel) and may also vary in time. Consequently, the net longshore flow prevents the formation of distinct circulatory patterns of smaller scale. Similar dynamics

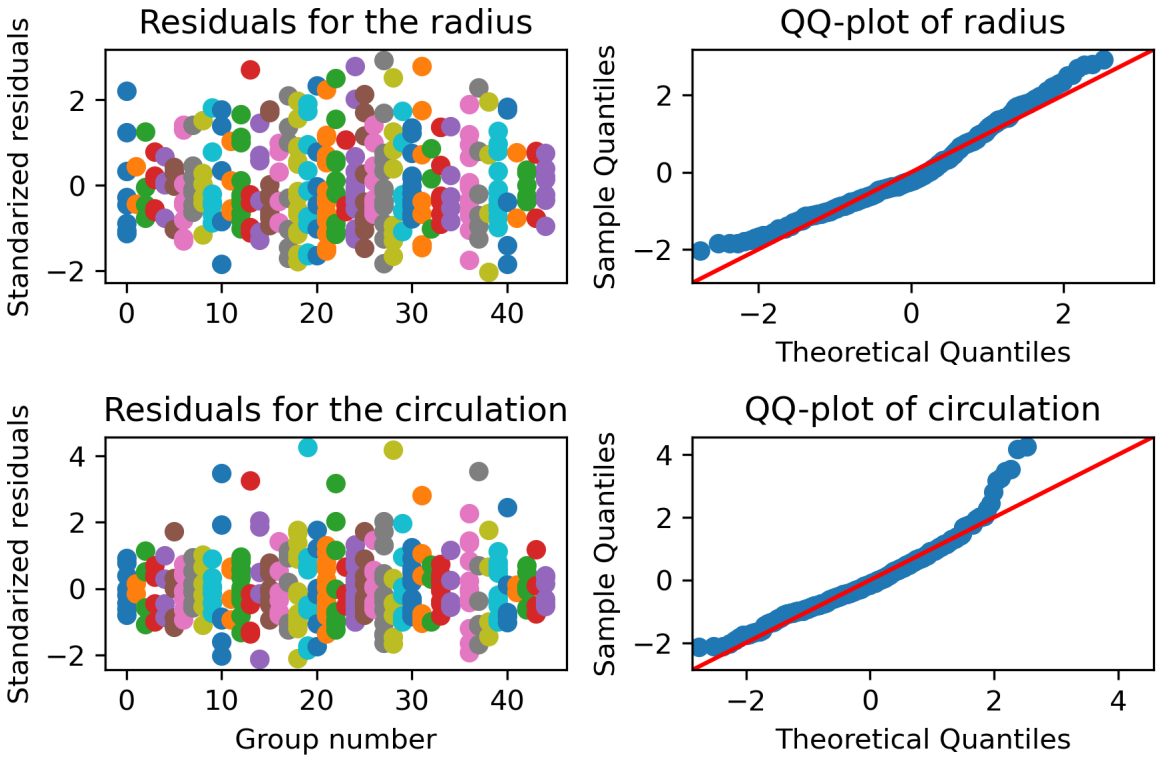

(a) Residuals and QQ-plots

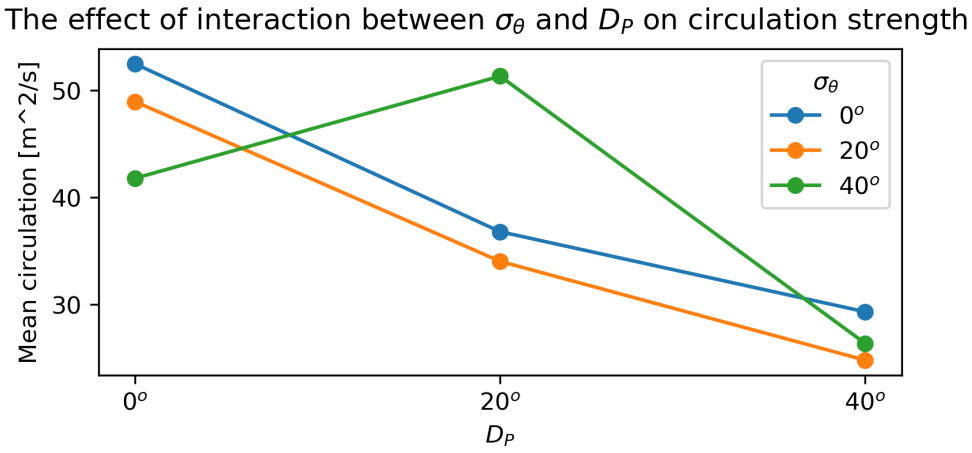

(b) Interaction terms

Figure 32: a) The residuals of the two ANOVA models used to test the dependence of vortex radius and circulation strength. The left plots shows every residual for every grouping of variables, and the right plots shows the standarized residuals plotted against the expected values from the normal distribution. The residuals from the radius are close to normally distributed, while the circulation has a few values which are larger than expected. b) The mean value of circulation plotted for different values of σ_θ and D_P. There is a interaction for $\sigma_\theta = 40^o$ and $D_P = 20^o$

.

were also observed by [Choi et al., 2015]. Therefore there is less organized net vortex movement over time in these cases, and we see less vortex formation. But when these vortexes first organize, for example in the wake of an exit or the shadow of a swing in the alongshore current, then the size and strength of these seem unaffected by the direction.

Lastly σ_θ impacts the distribution of large and small vortices, their strength, and their average size. When incoming waves comes at multiple angles into the surf zone, their momentum cancels and the resulting flow becomes weaker inside the zone. When averaging over longer times the vorticity decreases for larger spreads as also found in [O'Dea et al., 2021]. With less vorticity on average it follows that the limits of circulatory strength also falls for higher spreading, as our data shows us. With no spreading from the incoming wavefield, all the vorticity in the surf zone is bathymetry driven. Since this is constant in all our simulation it is natural that the average vorticity and thus circulatory strength is larger for these cases. It also tells us that bathymetry driven vorticity is a main force of vortexes in the surf zone. The directional spreading inhibits vortexes by nonlinear interactions since inside the surf zone higher spreading induce wave breaking in directions opposite to the flow decreasing the speed at which it flows [Choi et al., 2015]. [Baker et al., 2021] with their experiments on the American east coast, where they found that higher spreading is connected to smaller radii.

Combined this means that all three parameters influences the characteristics of the vortices, both in terms of size and strength. Not only do the parameters influence the flow in the beach, but they also interact with each other in a complex way. In this paper we have seen that tides and directional spreading influences the distribution of large versus small vortexes, while tide and the main direction of the wave field influences the numbers of vortexes. In addition we found more complex interaction between directional spread and main directional, which we have no explanation for at this moment.

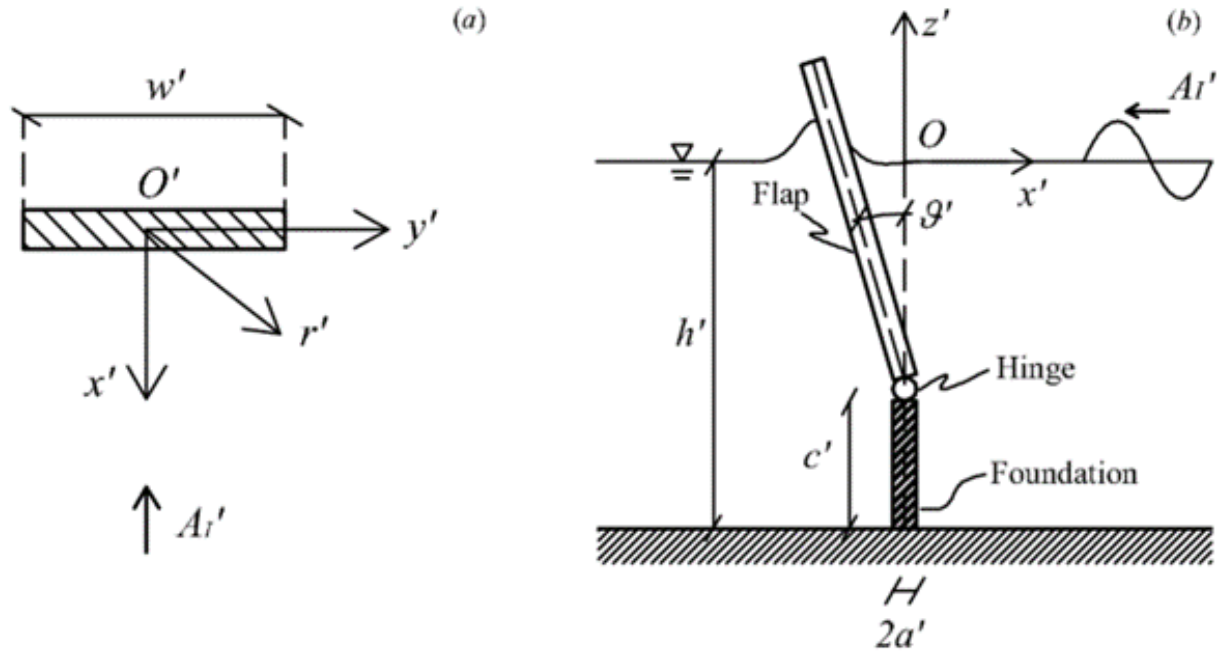

Figure 33: Geometry of the system in physical variables (a) plan view (b) section view [Renzi and Dias, 2013]

7 Oscillating wave surge converter

7.1 Background

The goal of this chapter is to somehow implement an OWSC into BOSZ to track how it influences the nearshore circulation at Sylt.

7.2 Analytical solution to capture factor of an OWSC

Consider a rectangular OWSC consisting of a flap attached to a foundation sitting on a flat ocean floor. [Renzi and Dias, 2013] then showed that when this device is under the influence of a monochromatic wave of amplitude A' and period T' (where $'$ denote physical variables), a potential flow model can be solved analytically. They showed that through calculating constants depending on parameters regarding the converter's geometry and the incoming wave field, one can express the capture factor of each wave. Constants regarding the flap's geometry is the first and second moment of inertia $S = \frac{S'}{\rho b'^4}$ and $I = \frac{I'}{\rho b'^5}$ and the elastic moment of inertia due to net buoyancy $C = wa(h-c)^2 - S$.

Further they expressed the boundary conditions on the converter as:

$$f_n = \frac{\sqrt{2[\kappa_n(h-c)sinh(\kappa_n h)+cosh(\kappa_n c)-cosh(\kappa_n h)]}}{\kappa_n^2(h+\omega^{-2}sinh^2\kappa_n h)^{\frac{1}{2}}} \tag{128}$$

$$d_0 = \frac{k(h+\omega^{-2}sinh^2 kh)^{\frac{1}{2}}}{\sqrt{2\omega cosh(kh}}, \qquad d_n = 0 \quad \forall \quad n > 0 \tag{129}$$

Where $\kappa_0 = k_0$ and $\kappa_n = k_0$ are the solutions of the dispersion relations:

$$\omega^2 = k_0 tanh(k_h) \quad \omega^2 = -k_n tan(k_n h) \tag{130}$$

With this they solved for the jump in potentials across the plate as given by the two following infinite system:

$$\sum_{p=0}^{P} \begin{Bmatrix} \alpha_{pn} \\ \beta_{pn} \end{Bmatrix} C_{pn}(v_0) = - \begin{Bmatrix} f_n \\ d_n \end{Bmatrix} \quad v_0 \in (-1, 1) \tag{131}$$

Where the C_{pn} constants are given by:

$$C_{pn}(v_{0j}) = -(p+1)U_p(v_{0j}) + \frac{i\kappa_n}{4}\int_{-1}^{1}(1-u^2)^{\frac{1}{2}} \cdot U_p(u) \cdot \left[\frac{R_n(\frac{1}{2}\kappa_n|v_{0j}-u|)}{|v_{0j}-u|}\right] du \tag{132}$$

Here, U_p is the p'th Chebyshev poylnomial of the first kind and R_n is:

$$R_n(\alpha) = J_1(\alpha)[1 + \frac{2i}{\pi}(ln\frac{\alpha}{2} + \gamma)] - \frac{i}{\pi}\left[\frac{\alpha}{2} + \sum_{j=2}^{\infty}\frac{(-1)^{j+1}(\frac{\alpha}{2})^{2j-1}}{j!(j-1)!}(\frac{1}{j}\sum_{q=1}^{j-1}\frac{2}{q})\right] \tag{133}$$

And $J_1(\alpha)$ is the Bessel function of the first kind and order, and γ is the Euler constant.

Solving for α_{pn} and β_{pn} allowed Renzi and Dias to solve for $\nu = \frac{\omega\pi}{4} f_0 \text{im}(\alpha_{00})$, the torque due to inertia of the system, and $F = -\frac{\omega\pi}{4} i\omega A_I \beta_{00} f_0$ the complex excitation. Which in turn allowed them to express the average capture factor over a wave as:

$$C_f = \frac{|F|^2}{2A_I^2 C_g(\eta + \eta_{pto})} \tag{134}$$

Where A_I is the incoming wave amplitude, C_g the group velocity, and ν_{pto} is the optimized extraction rate given by:

$$\nu_{pto} = \sqrt{\frac{C - (I+\mu)\omega^2)^2}{\omega^2} + \nu^2} \tag{135}$$

7.3 Numerical solutions

7.3.1 Pseudo-code

Algorithm 1 Determine the capture factor for every WEC

$P = 5$ to truncate α and β
$N = 2$ to truncate f_n, d_n, κ_n, k_n
for every ΔM timesteps **do**
  for all WEC **do**
    Low-pass gauge data to find T and A', and calculate ω and A_0
    Estimate k_n and κ_n with Newtons method and ITP
    Calculate f_n and d_0
    for every $C_{pn}(v_{0j})$ **do**
      Use adaptive Gauss-Legrende Quadrature until error $< 2\%$
      Trunctate Rn at 5 factorial
    end for
    Solve linear system for α_{pn} and β_{pn}
    Calculate F, ν and ν_{pto}
    Calculate the capture factor
  end for
end for

7.3.2 Numerical solutions

The input to Renzi' and Dias' solution is the incoming waves period and amplitude. This is unknown, where the only available information regarding the wave field are the ocean elevation and particle speed at fixed locations. However, one can estimate the incoming wave period and amplitude on a wave-by-wave basis by looking at the time record of a gauge placed further ahead of the OWSC. Every time I look to update the capture ratio of the OWSC, I find the three first zero-mean-crossings which provides the wave period. In addition, the zero-mean-crossings of an array of backwards finite differences of the wave elevation is used to find the location of the maximum and minimum wave elevation, from which the wave height and amplitude is calculated.

The next numerical challenge is to solve equations (130) for the wave numbers, both of which are impossible to solve exact. But the leftmost equation is a strictly increasing and approaching a linear function for large input k, Newton's method is effective to solve it.

The rightmost equation is less trivial to solve. Here I need to find the first n positive solutions of the equation. The equation has the useful property that it is decreasing and has vertical asymptotes for $k_j = \frac{\pi}{2H} + \pi j$, $j \geq 0$. This means that for every subdomain $k \in (k_j, k_{j+1})$ there is exactly

one solution. Hence solving for the n first solutions is done by using the secant- and bisection-like method ITP. These solutions are worked on in parallel until the change of values are less than 10^{-7} for all the values in one iteration.

To solve the linear system eq. (132) it is necessary to define discrete values for v_0 and truncate n and p. [Renzi and Dias, 2013] references that choosing v_{0j} to be equal to the j'th zero of the Chebyshev polynomial of the first kind provides the fastest convergence:

$$v_{0j} = \cos\left(\frac{(2j+1)\pi}{2P+2}\right), \quad j = 0, 1, ..., P \tag{136}$$

Further they claim that truncating $N = 2$ and $P = 5$ is sufficient to obtain a maximum relative error of $O(10^{-15})$. Hence my scheme is also truncated at this value.

Calculating the integral of $C_{pn}(v_{0j})$ is done via an adaptive Gauss-Legendre scheme. For each iteration the error is estimated as the difference between two successive iterations and is continued until a 2% error is obtained. This part of the scheme is computational intensive and is thus ended at a much larger error than the previous calculations. Hence it is likely that any error in the resulting estimate is contained in this calculation.

Contained in the calculation for C_{pn} is also a truncation for the calculation of R_n. Here the factorials are precomputed for efficiency, and the infinite sum is truncated to 5 by experience.

All other values are calculated straightforward through a direct relation, without any need to use numerical methods.

7.3.3 Comparison to results of Renzi and Dias

My results line up perfectly with Renzi' And Dias' results, except for values of the capture factor for wave periods greater than $\approx 8s$. The reason of this is unbeknownst to me, as it seems odd that every part matches up until the last calculation. Especially odd is the part where the initial peak matches well, but for higher values of T it no longer matches.

7.4 Connecting porosity and capture factor

The porosity used in the BOSZ model (Ch. 1.4.3) is not the same as the capture factor calculated in Ch. (7.3.2). To model our OWSC in BOSZ as a breakwater I propose that the friction factors mentioned in Ch. (1.4.3) is used, since it removes energy as a wave moves through the location, and that our measure of comparison should be how much energy is removed when choosing for a given porosity.

Figure 34: Left: Results from Renzi and Dias original paper. Right: The recreation from my scheme. The diagrams a), b), and c) matches perfectly to the eye, but diagram d) from my scheme does not have an uptick for higher periods.

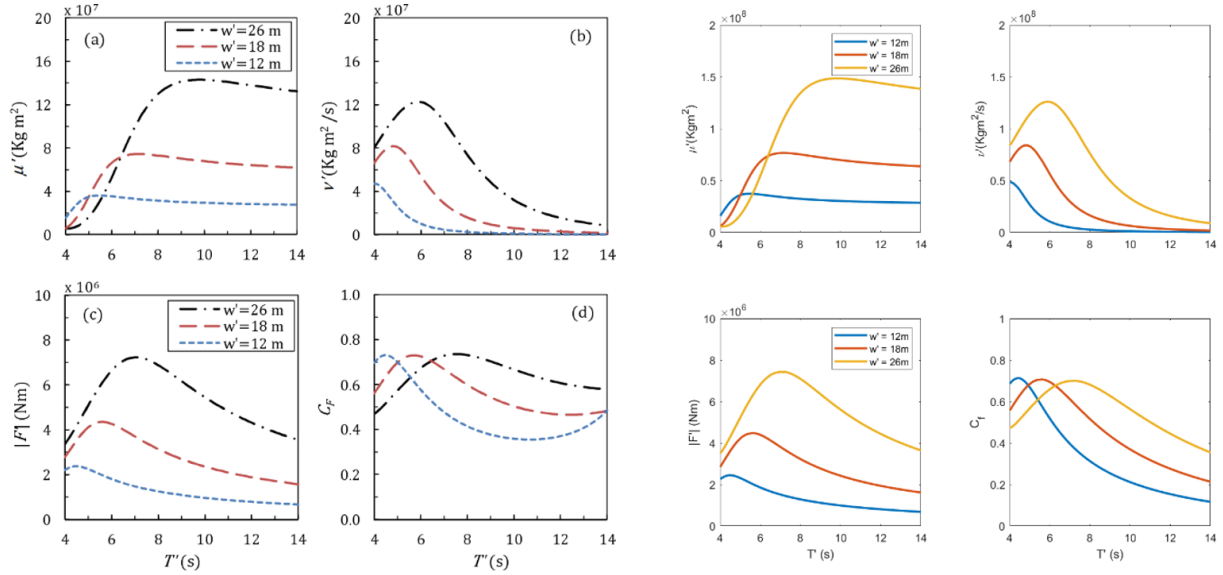

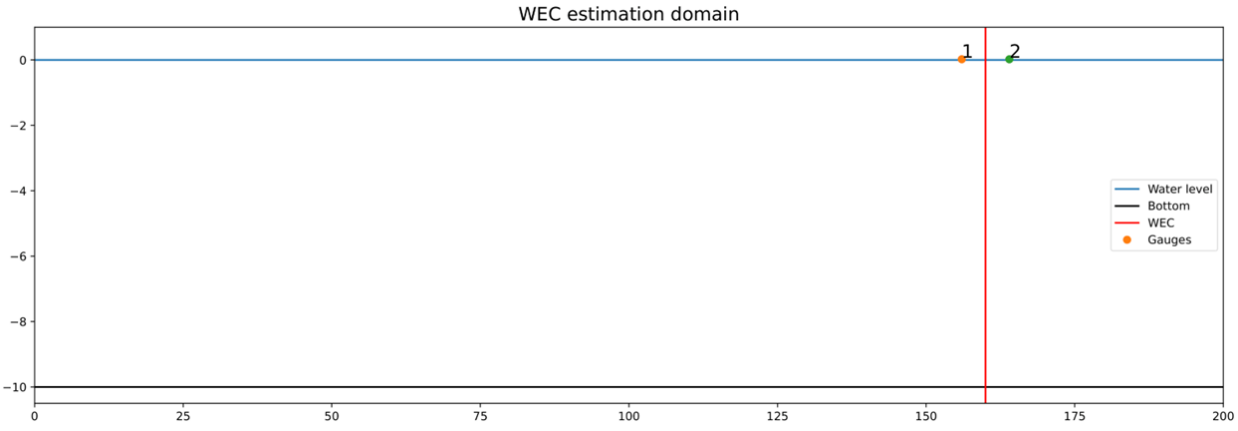

Figure 35: Domain for estimating the energy removed for a given porosity.

Figure 36: Wave ampltitude (top) and spectral density (bottom) before and after a JONSWAP wave field passes through a numerical OWSC with porosity equal 0.2 (left) and 0.1 (right).

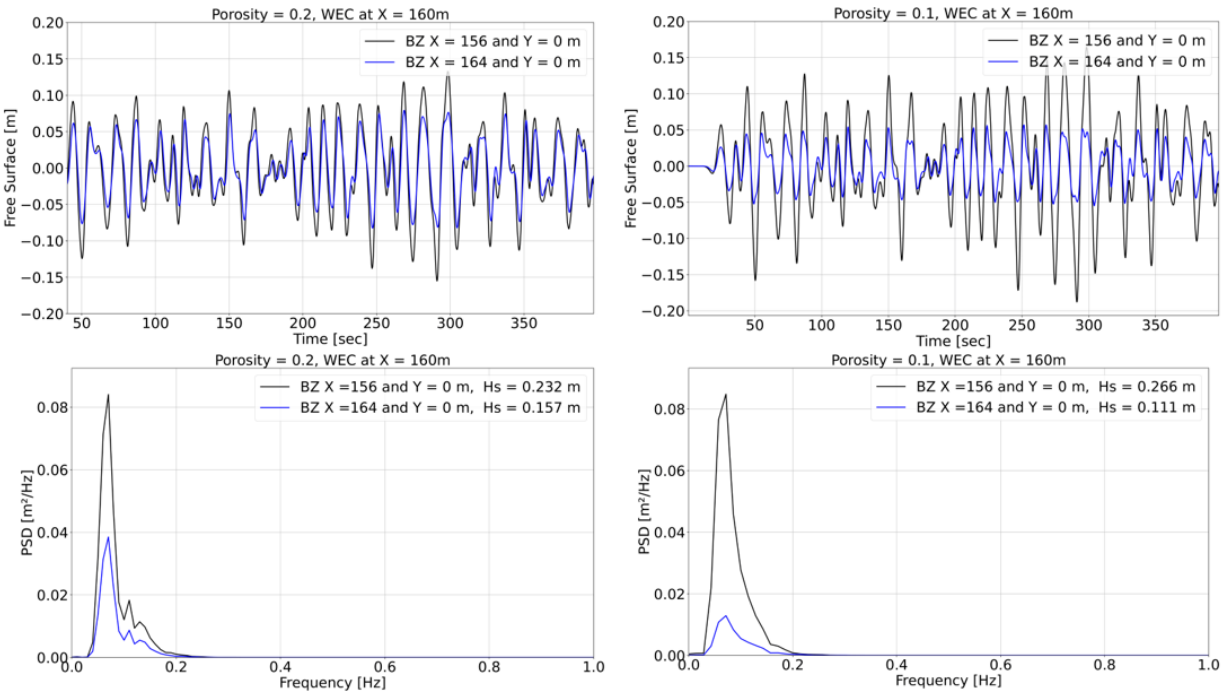

To calculate this energy, I simulate a representative incoming JONSWAP wavefield. This wavefield is measured right before and right after it hits the converter (see Fig. 35). The signal is then converted to a power spectral density, which is integrated to measure the percentage loss of energy. In Fig. (36) I plot porosities of 0.2 and 0.1 maps to a capture factor of 0.5414 and 0.8334 respectively. Repeating this process for various values of porosities yields a discrete mapping of porosities and capture factors (Fig. 37). This method accounts for the loss in energy on the beach side of the OWSCs, but as we do not control the amount of energy reflected outwards the computed data on the sea side of the devices is not to be trusted. But the beach side which is where we are interested in at the moment should have the right amount of energy coming through.

The above plot suggests that when the porosity approaches zero, no energy is transported through the breakwater. This is as expected and reflects that 100% of the energy is captured. But when the porosity approaches one from the left, it does not let through all the energy. A convergence towards 0 would be expected, since a medium with porosity 1 has no material blocking it, but my above tests imply that the captured energy converge towards 0.2. Hence for capture factors below 0.2 I am left with the choice of choosing a porosity which captures 20% of the energy or

Figure 37: Figure 8: Capture factor as a function of porosity, note abrupt change from porosity = 0.99 to porosity = 1

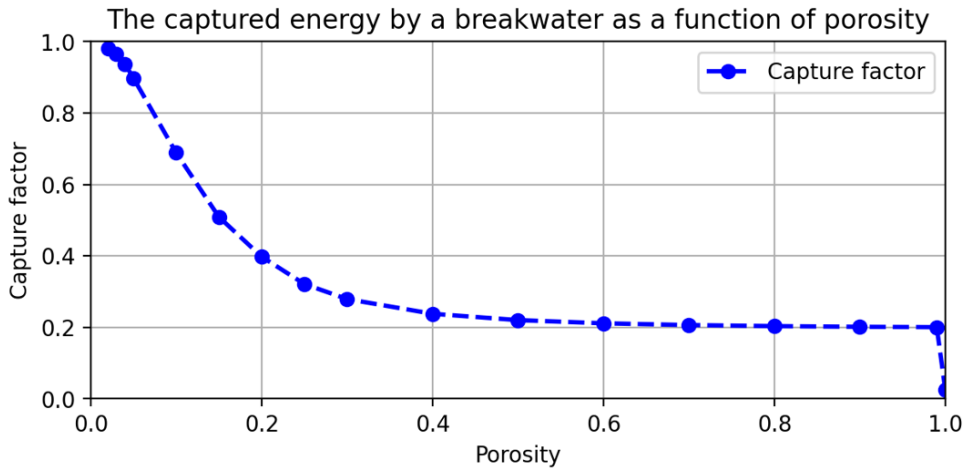

deactivating the breakwater. Of these approaches I have chosen the latter.

In the live simulation with varying capture factor our process will thus be threefold.

- First the incoming wave elevations are calculated on a regular basis. At a location in front of the OWSC the elevations are recorded.
- These are sent to my calculations for the OWSC to find the current capture factor. If the capture factor is lower than 0.2 the porosity is set to 1, to ignore the OWSC.
- Before lastly the corresponding porosity is found via the above table, and linear interpolation, and inputted to the BOSZ model for further simulation.

The variables of where and how often this calculation should be carried out is chosen at the beginning of the simulation. The porosity is then dynamically changed to estimate the needed energy removal. This approach has the potential issue that the abrupt changing of porosity might induces a backwards travelling wave if the water level is higher behind the OWSC than in front. A potential solution would be to slowly change the porosity from one to another to mitigate the effect, but this is not accounting for at writing time.

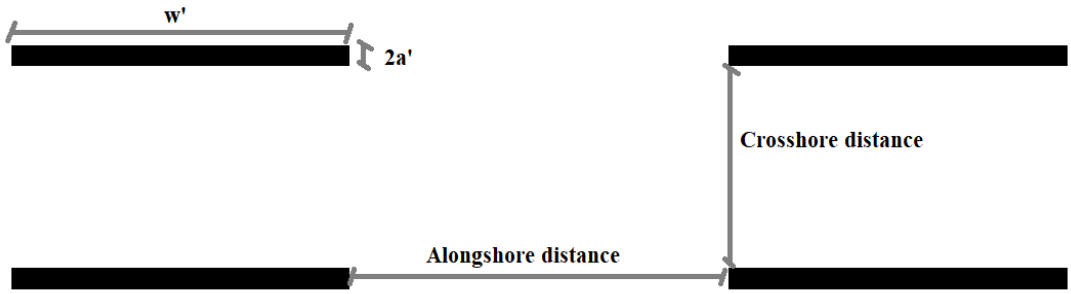

Figure 38: Farm configuration. This pattern is repeated across the entire domain at a fixed latitude.

Table 4: Dimensions of the OWSC devices and farm configuration

Width w'	Thickness 2a'	Hinge height c'	Alongshore distance	Crosshore distance
25m	1.8m	1.5m	25m	15m

7.5 Effect on circulation at Sylt

7.5.1 Dimensions

Now I test how building OWSCs in the surf zone would impact the local circulation outside Sylt. There has been multiple studies regarding optimal size of the devices, OWSC farm configurations, and comparisons with other WEC devices [Babarit, 2015, Benites Muñoz, 2022, Babarit et al., 2012, Noad and Porter, 2015, Sarkar et al., 2014].

It has been found that these devices works best at depths between 8 and 15 meters, and that the devices themselves should be 24.6 meters wide and 1.9 meter thick [Noad and Porter, 2015]. In our model I have therefore deemed to use these values for the devices. The depth is not controllable by me, but luckily the depth of our bathymetry of Sylt about 8m, so the devices are placed in depths around that value.

Further much effort have been put into evaluating different patterns of the OWSC farms, and it has been found that while the different interaction between the devices has an effect on the efficiency it is unknown how a varying bathymetry changes the conclusions [Sarkar et al., 2014]. They further found that multiple layers of closeby devices has a detrimental effect on the efficiency, both for the forward and backwards devices [Benites Muñoz, 2022]. The devices should therefore be placed as far away from each other as possible, but this is in practice impossible given the space constraint. As the devices cannot be placed unlimited in the alongshore direction either, I have come to an compromise with placing two rows of devices along the length of our domain to simplify the placements for an initial study. They stand in a straight north-south line around $400 - 500$ meters offshore.

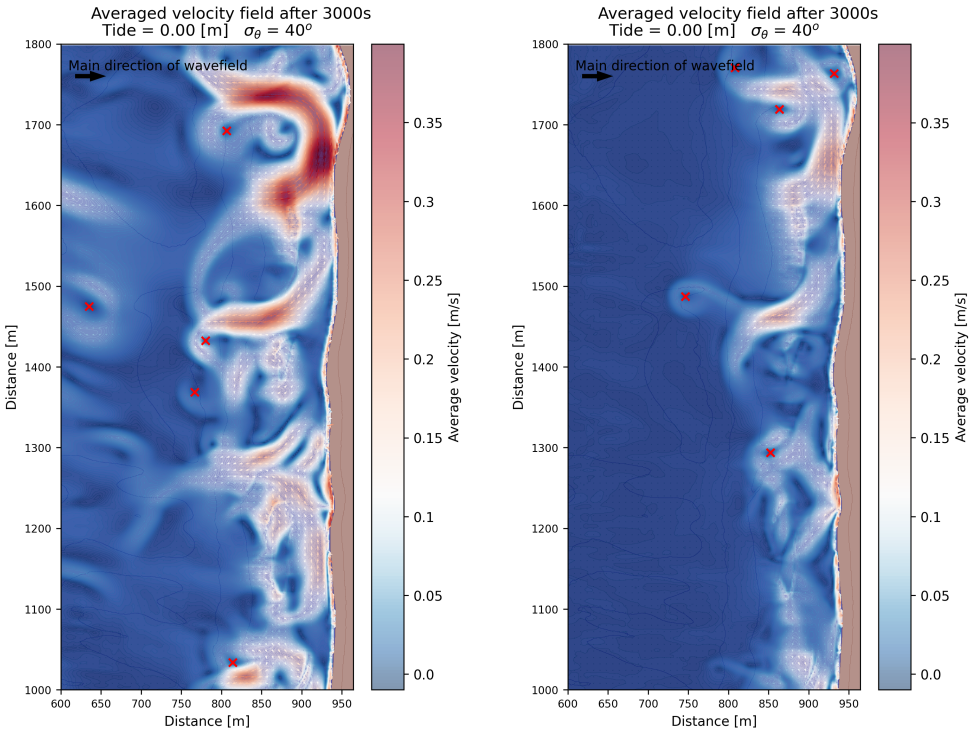

(a) Without an OWSC farm

(b) With an OWSC farm

Figure 39: A subsection of the average velocity field for one simulation with multiple vortexes of different sizes and strengths. The red markers denote where we identified centres of vortexes. The subsection and input parameters are the same for both figures. The only difference is the inclusion of the OWSC farm in figure b). Some of the flow patterns can be recognized, but with a lower value.

7.5.2 Numerical setup

The bathymetry and wave field are identical to the one used in Ch. (6). I also simulate the same 35 runs, varying the tide, directional spreading and the main direction of the incoming wave field. The only thing which is changed is the inclusion of OWSCs in the model.

The OWSCs are modelled as having the capture factor described in Ch. (7.3.2) and by using the in-built porosity calculations of BOSZ as described in Ch. (1.4.3) and (7.4). I define beforehand the placements of the OWSC. BOSZ uses this location to find the smallest depths for each device, to model the fact that the seafloor would need to be flattened to place the device, which is then used to calculate the capture factor. The width of the device is calculated to be 1.9m but in the model it is modelled as being 2m as that is mesh resolution.

While in Ch. (7.4) I propose a wave-by-wave tracking scheme, it is in practice hard to implement a wave-tracker to know the length and period of an individual wave in a 2D random wave-field. I have therefore in this chapter assumed that the efficiency of the OWSC are about

that for the significant wave height and mean period. Hence the capture factor and the porosity is constant throughout the run.

7.5.3 Statistical results

In this section we do a repeat of the analysis in Ch. (6.2.3), but for the new data acquired from simulating with a OWSC farm in the domain. The method of identifying the vortices are the same as in Ch. (6.1.2), and the same programs are used to post-process them. See Fig. (39) for an example comparison.

Firstly, by looking at the distribution of radii and circulatory strength, Fig. (40) (a), it is obvious that the distributions have shifted left. This is especially true for the strength of the circulations. A results of this is that the circulatory strength have approached an exponential distribution, while the radii is an even better fit to a Gamma distribution. This is reflected by the fact that the logarithmic transform is close to a normal distribution.

In Fig. (40) (b) the total number of vortices associated by the different parameters and their relative size compared to the median is plotted. The influence of the parameters σ_θ and D_P is similar to the case without an OWSC farm, while the tide have a new pattern. As the tide increases, the number of vortices decrease in the surf zone.

To compare the two cases, with and without OWSCs, boxplots of the sizes of the radii and circulatory strength for the different values of the parameters are plotted in Fig. (41). Here we it is seen that indeed for all parameters the

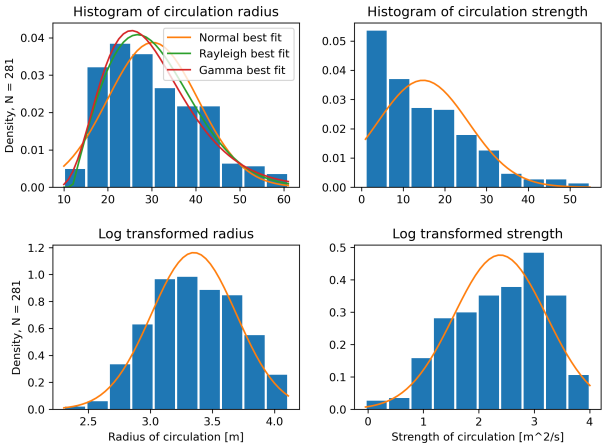

(a) Strength and radii with all parameters combined

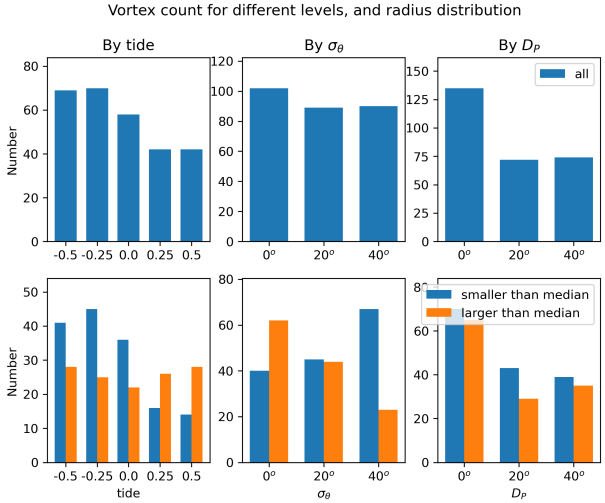

(b) Number of vortexes by parameter value..

Figure 40: a) The histogram of the raw and log transformed data of all the vortexes radii (left) and circulation strength (right), together with the best fit normal distribution. b) Top: The combined number of vortexes for different values of tide, spread, and D_P. Bot: The number of vortexes divided by if they are smaller or larger than the median radius of the vortexes.

Table 5: p-values from the Mann-Whitney U test for the difference between the radius and circulation of the vortices with or without WECs present in the domain. The statistical significant variables are shown in bold at the level $\alpha = 0.05$.

	Radius	Strength
p-values	**2.23e-20**	**3.17e-39**

radius and strength of the circulations have decreased. This is true for both the mean and the spreading of the quantiles for both values, but is especially true for the circulatory strength. Testing the null hypothesis that the circulations and radiuses are drawn from the same distribution with the non-parametric Mann-Whitney U test it is seen from table (5) that they are indeed statistically different.

7.6 Discussion

By placing an OWSC farm in front of the surf zone of a beach, we see that the circulation decrease in both size and strength. This is natural, as the idea of such a farm is to extract energy which means that the waves have less energy to circulate when approaching the shore. As a consequence there is less energy available to mix the near shore ocean.

This effect is larger for higher tides. This might be due to the fact that the Oyster device which the solution of [Renzi and Dias, 2013] is based upon have an optimal depth of $8 - 15$m, where our bathymetry has a depth of at most 8m. For lower tides we are therefore operating in non-efficient depths, and for high tides the devices are efficient. This would explain why for high depths the waves which approuch shore have less energy and circulate less. During the manual circulation identification it was noticed that the velocities were very small for these cases except for a few places.

The fact that we managed to identify more smaller circulations indicate that not just circulations but also exits and alongshore current is smaller. This is due to the fact that if these were significant, their influence of the mean surface velocities would overshadow the circulations and it would not be possible to see them with our methodology.

This decrease in radius, and drastic decrease in circulatory strength might have a large influence on the mixing of the ocean nearshore. Sediment transport will be lessened, and biological life which are depending upon it will be affected. How much these large OWSCs would influence these nearshore processes and life must be further researched.

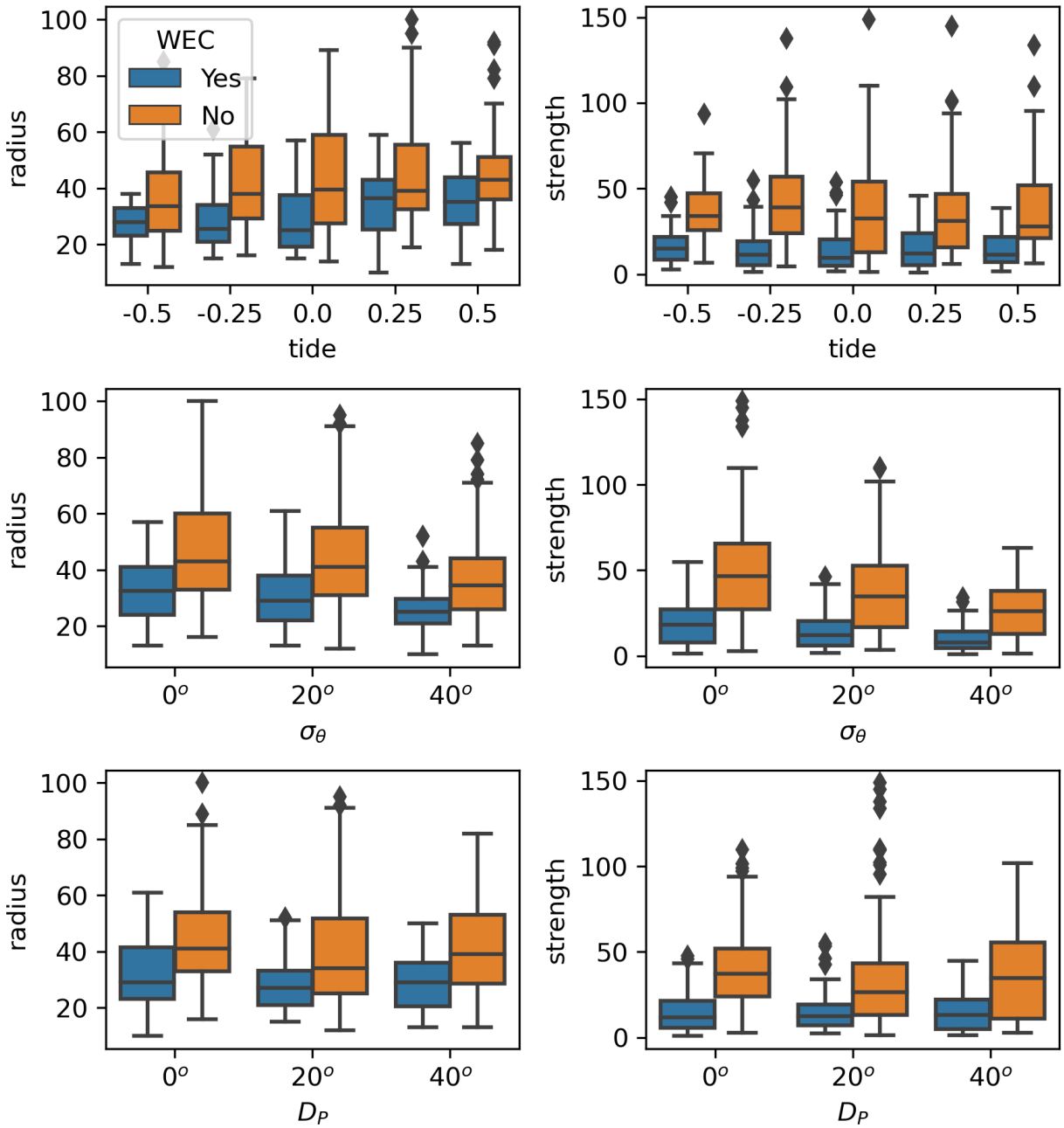

Figure 41: The box plots of vortex radius and circulation strength for all the variables, both with (blue) and without (orange) the OWSC farm. The leftmost boxplots are for the radius and rightmost for the strengths.

8 Summary

In Chapter (4) it was found that particle transport is much more sensitive to waves originating in the infra-gravity (IG) band. These are waves which typically have much smaller amplitudes than the typical waves seen on the ocean, and their long period and wavelength makes them hard to spot while looking at out at sea. Nevertheless it was found that the movement of particles have a significant component in IG frequency offshore. As the waves break in the surf zone the IG band grows in importance before the movement associated with them are dominant in the surf zone. This explains multiple effects that has been found to be dominated by IG frequencies such as the location of the river plume [Flores et al., 2022], net movement of inertial particles [Bjørnestad et al., 2021], and sand flux [Mendes et al., 2020].

As it was found that the phase-resolving nearshore wave model Boussinesq Ocean and surf zone model (BOSZ) can generate these kind of waves, it also makes sense that the model can be used to somewhat accurately predict the movement of actual particle paths. In Chapter (5) this was put to the test by comparing the simulated paths in BOSZ with actual orange paths outside Sylt. Oranges was tracked through pictures taken with a stereo camera and combined with GPS data to recreate their position in a coordinate system. Combining this data about their position with data regarding the bathymetry, tide levels, and wave compositions it was possible to numerically recreate the wave conditions of the day. In the resulting simulated movements we find that the numerical paths matches the actual paths to a satisfactory degree. Further it was found that the drifters moved slowly in one direction while having much faster oscillating movements while travelling there. This of course follows from the discussion that the slowly varying IG waves dominate the movements. It was also found that these IG waves is critical to accurately simulate particles in the surf zone, as the phases of the waves determined the direction of movement of the particles. Only by averaging paths by different phases could we get the right paths, a results which is necessary to include in all further work in tracking near shore particles.

Along the coast multiple large scale fluid patterns can be found. There exists regions of flow which primarly move towards the beach or out of the beach, the latter of which is known as rip currents, as well as alongshore flow and lastly large scale circular patterns called vortexes. In Chapter (6) and (7) it was found that vortexes in the surf zone are dependent upon the tide level, the mean direction the waves were coming from, and if they all came in at the same angle or not. The radii, strength and the number of these circular movements for different values of these parameters were compared, and it was found through statistical testing that some of the parameters only influenced the radii of the vortexes, while others influenced the strength or number of vortexes.

Oscillating wave surge converter (OWSC) devices are a relatively new type of wave energy converter of recent interest as these can capture a large percentage of the energy of the waves (capture factor). In Chapter (7) a method of analytically calculating the capture factor for a wave was retold. A way of numerically calculate this factor was developed, and how to include this in the BOSZ model was explained. The inclusion of a farm of OWSCs in the bathymetry had the effect of reducing all the radii and circulatory strength in the surf zone, while keeping most of the relationships from the case with an open beach.

A better understanding of the vortex structures can shed light into the intensity of mixing. This goes beyond this project but we might be able to recalculate the vertical exchange of water by knowing the size and intensity of eddies. The fact that we found in Chapter (6) that vortexes at the beach match the fundamental Rankine vortex yields a better feeling of what to expect from computations. It might be possible to use the computed results in combination with analytical solutions to create better estimates for mixing ratios in the future. This can among other help to understand the influence OWSC farms have on the local ecology and morphology.

References

[emo, 2022] (2022). Bathymetry.

[Lei, 2022] (2022). High-density airborne lidar sensor ideal for challenging coastal survey of sylt.

[Babarit, 2015] Babarit, A. (2015). A database of capture width ratio of wave energy converters. *Renewable Energy*, 80:610–628.

[Babarit et al., 2012] Babarit, A., Hals, J., Muliawan, M. J., Kurniawan, A., Moan, T., and Krokstad, J. (2012). Numerical benchmarking study of a selection of wave energy converters. *Renewable energy*, 41:44–63.

[Baker et al., 2021] Baker, C. M., Moulton, M., Raubenheimer, B., Elgar, S., and Kumar, N. (2021). Modeled three-dimensional currents and eddies on an alongshore-variable barred beach. *Journal of Geophysical Research: Oceans*, 126(7):e2020JC016899.

[Barthelemy et al., 2018] Barthelemy, X., Banner, M., Peirson, W., Fedele, F., Allis, M., and Dias, F. (2018). On a unified breaking onset threshold for gravity waves in deep and intermediate depth water. *Journal of Fluid Mechanics*, 841:463–488.

[Battjes, 1994] Battjes, J. (1994). Shallow water wave modelling. In *Proc. Int. Symp.: Waves-physical and numerical modelling, Vancouver*, pages 1–23.

[Beji and Battjes, 1993] Beji, S. and Battjes, J. (1993). Experimental investigation of wave propagation over a bar. *Coastal engineering*, 19(1-2):151–162.

[Benites Muñoz, 2022] Benites Muñoz, D. A. (2022). *Numerical modelling of oscillating wave surge converters operating in array configurations*. PhD thesis, UCL (University College London).

[Bertin et al., 2018] Bertin, X., de Bakker, A., van Dongeren, A., Coco, G., André, G., Ardhuin, F., Bonneton, P., Bouchette, F., Castelle, B., Crawford, W. C., Davidson, M., Deen, M., Dodet, G., Guérin, T., Inch, K., Leckler, F., McCall, R., Muller, H., Olabarrieta, M., Roelvink, D., Ruessink, G., Sous, D., Éléonore Stutzmann, and Tissier, M. (2018). Infragravity waves: From driving mechanisms to impacts. *Earth-Science Reviews*, 177:774–799.

[Bertin et al., 2019] Bertin, X., Mendes, D., Martins, K., Fortunato, A. B., and Lavaud, L. (2019). The closure of a shallow tidal inlet promoted by infragravity waves. *Geophysical Research Letters*, 46(12):6804–6810.

[Bjørnestad, 2021] Bjørnestad, M. (2021). A study of the influence of vorticity, capillarity and slope angle on the properties of shoaling and breaking waves.

[Bjørnestad et al., 2021] Bjørnestad, M., Buckley, M., Kalisch, H., Streßer, M., Horstmann, J., Frøysa, H. G., Ige, O. E., Cysewski, M., and Carrasco-Alvarez, R. (2021). Lagrangian measurements of orbital velocities in the surf zone. *Geophysical Research Letters*, 48(21):e2021GL095722.

[Bondehagen et al., 2023] Bondehagen, A., Roeber, V., Kalisch, H., Buckley, M., Streß er, M., Cysewski, M., Horstmann, J., Bjø rnestad, M., Ige, I., Frø ysa, H., and Carrasco-Alvarez, R. (2023). Wave-driven current and vortex patterns at an open beach: Insights from phase-resolving numerical computations and lagrangian measurements. *Submitted*.

[Buckley and Veron, 2017] Buckley, M. P. and Veron, F. (2017). Airflow measurements at a wavy air–water interface using piv and lif. *Experiments in Fluids*, 58(11):161.

[Bühler and Jacobson, 2001] Bühler, O. and Jacobson, T. E. (2001). Wave-driven currents and vortex dynamics on barred beaches. *Journal of Fluid Mechanics*, 449:313–339.

[Choi et al., 2015] Choi, J., Kirby, J. T., and Yoon, S. B. (2015). Boussinesq modeling of longshore currents in the sandyduck experiment under directional random wave conditions. *Coastal Engineering*, 101:17–34.

[Dean and Dalrymple, 1991] Dean, R. G. and Dalrymple, R. A. (1991). *Water wave mechanics for engineers and scientists*, volume 2. world scientific publishing company.

[Drew et al., 2009] Drew, B., Plummer, A. R., and Sahinkaya, M. N. (2009). A review of wave energy converter technology.

[Engelund, 1953] Engelund, F. (1953). *On the laminar and turbulent flows of ground water through homogeneous sand*. Akad. for de Tekniske Videnskaber.

[Flores et al., 2022] Flores, R. P., Williams, M. E., and Horner-Devine, A. R. (2022). River plume modulation by infragravity wave forcing. *Geophysical Research Letters*, 49(15):e2021GL097467.

[Gustafsson, 2007] Gustafsson, B. (2007). *High order difference methods for time dependent PDE*, volume 38. Springer Science & Business Media.

[Gustafsson et al., 1995] Gustafsson, B., Kreiss, H.-O., and Oliger, J. (1995). *Time dependent problems and difference methods*, volume 24. John Wiley & Sons.

[Hasselmann, 1974] Hasselmann, K. (1974). On the spectral dissipation of ocean waves due to white capping. *Boundary-Layer Meteorology*, 6(1):107–127.

[Holthuijsen and Herbers, 1986] Holthuijsen, L. and Herbers, T. (1986). Statistics of breaking waves observed as whitecaps in the open sea. *Journal of Physical Oceanography*, 16(2):290–297.

[Holthuijsen, 2010] Holthuijsen, L. H. (2010). *Waves in oceanic and coastal waters*. Cambridge university press.

[Kennedy et al., 2000] Kennedy, A. B., Chen, Q., Kirby, J. T., and Dalrymple, R. A. (2000). Boussinesq modeling of wave transformation, breaking, and runup. i: 1d. *Journal of waterway, port, coastal, and ocean engineering*, 126(1):39–47.

[Kundu et al., 2015] Kundu, P. K., Cohen, I. M., and Dowling, D. R. (2015). *Fluid mechanics*. Academic press.

[Lay et al., 2016] Lay, D. C., Lay, S. R., and McDonald, J. J. (2016). *Linear algebra and its applications*. Pearson.

[LeVeque and Leveque, 1992] LeVeque, R. J. and Leveque, R. J. (1992). *Numerical methods for conservation laws*, volume 214. Springer.

[Longuet-Higgins and Stewart, 1960] Longuet-Higgins, M. and Stewart, R. (1960). Changes in the form of short gravity waves on long waves and tidal currents. *Journal of Fluid Mechanics*, 8:565–583.

[Longuet-Higgins and Stewart, 1961] Longuet-Higgins, M. S. and Stewart, R. (1961). The changes in amplitude of short gravity waves on steady non-uniform currents. *Journal of fluid mechanics*, 10:529–549.

[Longuet-Higgins and Stewart, 1962] Longuet-Higgins, M. S. and Stewart, R. (1962). Radiation stress and mass transport in gravity waves, with application to 'surf beats'. *Journal of Fluid Mechanics*, 13:481–504.

[Longuet-Higgins and Stewart, 1964] Longuet-Higgins, M. S. and Stewart, R. (1964). Radiation stresses in water waves; a physical discussion, with applications. In *Deep sea research and oceanographic abstracts*, volume 11, pages 529–562. Elsevier.

[Martins et al., 2022] Martins, K., Bertin, X., Mengual, B., Pezerat, M., Lavaud, L., Guérin, T., and Zhang, Y. J. (2022). Wave-induced mean currents and setup over barred and steep sandy beaches. *Ocean Modelling*, 179:102110.

[Mendes et al., 2020] Mendes, D., Fortunato, A. B., Bertin, X., Martins, K., Lavaud, L., Nobre Silva, A., Pires-Silva, A. A., Coulombier, T., and Pinto, J. P. (2020). Importance of infragravity waves in a wave-dominated inlet under storm conditions. *Continental Shelf Research*, 192:104026.

[Miche, 1944] Miche, M. (1944). Mouvements ondulatoires de la mer en profondeur constante ou décroissante. *Annales de Ponts et Chaussées, 1944, pp (1) 26-78,(2) 270-292,(3) 369-406*.

[Munk, 1951] Munk, W. H. (1951). Origin and generation of waves. Technical report, Scripps Institution of Oceanography La Jolla Calif.

[Noad and Porter, 2015] Noad, I. and Porter, R. (2015). Optimisation of arrays of flap-type oscillating wave surge converters. *Applied Ocean Research*, 50:237–253.

[Nwogu, 1993] Nwogu, O. (1993). Alternative form of boussinesq equations for nearshore wave propagation. *Journal of waterway, port, coastal, and ocean engineering*, 119(6):618–638.

[Nwogu, 1996] Nwogu, O. G. (1996). Numerical prediction of breaking waves and currents with a boussinesq model. *Coastal Engineering Proceedings*, (25).

[Nwogu and Demirbilek, 2001] Nwogu, O. G. and Demirbilek, Z. (2001). Bouss-2d: A boussinesq wave model for coastal regions and harbors. Technical report, ENGINEER RESEARCH AND DEVELOPMENT CENTER VICKSBURG MS COASTAL AND HYDRAULICSLAB.

[O'Dea et al., 2021] O'Dea, A., Kumar, N., and Haller, M. C. (2021). Simulations of the surf zone eddy field and cross-shore exchange on a nonidealized bathymetry. *Journal of Geophysical Research: Oceans*, 126(5):e2020JC016619.

[Peregrine, 1967] Peregrine, D. H. (1967). Long waves on a beach. *Journal of fluid mechanics*, 27(4):815–827.

[Pierson Jr et al., 1971] Pierson Jr, W. J., Neumann, G., and James, R. W. (1971). Practical methods for observing and forecasting ocean waves by means of wave spectra and statistics. Technical report, NAVAL OCEANOGRAPHIC OFFICE NSTL STATION MS.

[Pope and Pope, 2000] Pope, S. B. and Pope, S. B. (2000). *Turbulent flows*. Cambridge university press.

[Renzi and Dias, 2013] Renzi, E. and Dias, F. (2013). Hydrodynamics of the oscillating wave surge converter in the open ocean. *European Journal of Mechanics-B/Fluids*, 41:1–10.

[Roeber, 2021] Roeber, V. (2021). Boussinesq ocean and surf zone model bosz user manual.

[Roeber and Cheung, 2012] Roeber, V. and Cheung, K. F. (2012). Boussinesq-type model for energetic breaking waves in fringing reef environments. *Coastal Engineering*, 70:1–20.

[Roeber et al., 2010] Roeber, V., Cheung, K. F., and Kobayashi, M. H. (2010). Shock-capturing boussinesq-type model for nearshore wave processes. *Coastal Engineering*, 57(4):407–423.

[Russell, 1993] Russell, P. E. (1993). Mechanisms for beach erosion during storms. *Continental Shelf Research*, 13(11):1243–1265.

[Santamaria et al., 2013] Santamaria, F., Boffetta, G., Afonso, M. M., Mazzino, A., Onorato, M., and Pugliese, D. (2013). Stokes drift for inertial particles transported by water waves. *EPL (Europhysics Letters)*, 102(1):14003.

[Sarkar et al., 2014] Sarkar, D., Renzi, E., and Dias, F. (2014). Wave farm modelling of oscillating wave surge converters. *Proceedings of the Royal Society A: Mathematical, Physical and Engineering Sciences*, 470(2167):20140118.

[Scott et al., 2014] Scott, T., Masselink, G., Austin, M. J., and Russell, P. (2014). Controls on macrotidal rip current circulation and hazard. *Geomorphology*, 214:198–215.

[Simarro et al., 2013] Simarro, G., Orfila, A., and Galan, A. (2013). Linear shoaling in boussinesq-type wave propagation models. *Coastal Engineering*, 80:100–106.

[Stelling and Zijlema, 2003] Stelling, G. and Zijlema, M. (2003). An accurate and efficient finite-difference algorithm for non-hydrostatic free-surface flow with application to wave propagation. *International journal for numerical methods in fluids*, 43(1):1–23.

[Suzuki et al., 2017] Suzuki, T., Altomare, C., Veale, W., Verwaest, T., Trouw, K., Troch, P., and Zijlema, M. (2017). Efficient and robust wave overtopping estimation for impermeable coastal structures in shallow foreshores using swash. *Coastal Engineering*, 122:108–123.

[Swigler, 2010] Swigler, D. T. (2010). *Laboratory study investigating the three-dimensional turbulence and kinematic properties associated with a breaking solitary wave*. PhD thesis, Texas A & M University.

[Symonds et al., 1982] Symonds, G., Huntley, D. A., and Bowen, A. J. (1982). Two-dimensional surf beat: Long wave generation by a time-varying breakpoint. *Journal of Geophysical Research: Oceans*, 87(C1):492–498.

[Tolman, 1995] Tolman, H. L. (1995). Subgrid modeling of moveable-bed bottom friction in wind wave models. *Coastal engineering*, 26(1-2):57–75.

[Toro, 1997] Toro, E. F. (1997). Multidimensional test problems. In *Riemann Solvers and Numerical Methods for Fluid Dynamics*, pages 551–562. Springer.

[Ursell, 1953] Ursell, F. (1953). The long-wave paradox in the theory of gravity waves. In *Mathematical Proceedings of the Cambridge Philosophical Society*, volume 49, pages 685–694. Cambridge University Press.

[van Thiel de Vries et al., 2008] van Thiel de Vries, J., van Gent, M., Walstra, D., and Reniers, A. (2008). Analysis of dune erosion processes in large-scale flume experiments. *Coastal Engineering*, 55(12):1028–1040.

[Varing et al., 2021] Varing, A., Filipot, J.-F., Grilli, S., Duarte, R., Roeber, V., and Yates, M. (2021). A new definition of the kinematic breaking onset criterion validated with solitary and quasi-regular waves in shallow water. *Coastal Engineering*, 164:103755.

[Wei et al., 1999] Wei, G., Kirby, J. T., and Sinha, A. (1999). Generation of waves in boussinesq models using a source function method. *Coastal Engineering*, 36(4):271–299.

[Zelt, 1991] Zelt, J. (1991). The run-up of nonbreaking and breaking solitary waves. *Coastal Engineering*, 15(3):205–246.